Universidad de Cantabria

Departamento de Física Moderna

CSIC - Universidad de Cantabria

Instituto de Física de Cantabria

Cotas sobre la no-Gaussianidad primordial de tipo local con datos del fondo cósmico de microondas

Memoria presentada por el Licenciado

Andrés Curto Martín

para optar al título de Doctor en Ciencias Físicas

2009

Enrique Martínez González, Doctor en Ciencias Físicas y
Profesor de Investigación del Consejo Superior de Investigaciones Científicas,

CERTIFICA que la presente memoria

Cotas sobre la no-Gaussianidad primordial de tipo local con datos del fondo cósmico de microondas

ha sido realizada por **Andrés Curto Martín** bajo mi dirección.
Considero que esta memoria contiene aportaciones suficientes para construir la tesis Doctoral del interesado

En Santander, a 24 de Julio de 2009

Enrique Martínez González

Dedicado a la memoria de mi
abuela H. Díaz Hernández

Agradecimientos

El trabajo plasmado en esta tesis es producto del esfuerzo y la ayuda de muchas personas. En primer lugar, quiero agradecer a Enrique Martínez González, mi director de tesis, el tiempo y el esfuerzo dedicado para que todo este trabajo saliera adelante. En especial quiero agradecerle la oportunidad que me dio de unirme a su grupo a finales de 2004 así como todos los contactos científicos y amigos que he podido hacer por todo el mundo en estos fantásticos años.

Hay una larga lista de personas a las que agradecer su apoyo para hacer posible este trabajo. Quiero empezar con mis padres, ya que a ellos les debo la existencia y buena parte de lo que soy. Desde que tengo consciencia les recuerdo enseñando a mi hermana, a mi hermano y a mí lo importante que es el conocimiento, el esfuerzo y el trabajo bien hecho para poder salir adelante en nuestra sociedad. Mi hermana Gema y mi hermano Jaime también han seguido con interés mis publicaciones y andanzas por el mundo, esperando eso sí, que haga estancias en lugares interesantes para visitarme durante sus vacaciones.

Por lo que respecta al trabajo específico de la tesis, tengo agradecer la ayuda de extraordinarios colaboradores dentro del IFCA y de otros centros repartidos por el mundo. Muchas gracias a Belén Barreiro, cuyos comentarios han sido de gran ayuda en todos los capítulos de esta tesis; a Juan Francisco Macías-Pérez, Pia Mukherjee, José Alberto Rubiño y Eiichiro Komatsu. No puedo olvidarme de las personas que trabajan en la Unidad de Servicios Informáticos del IFCA así como el super-ordenador Altamira: buena parte de esta tesis no habría podido desarrollarse sin su inestimable ayuda. En particular estoy agradecido a Rafa Marco, Jesús Marco y más recientemente a Luis Cabellos.

También quiero agradecer la gran ayuda prestada a mis compañeros de despacho: Antonio y Marco en los primeros tiempos; Diego y Patri, a los que gané una apuesta sobre quién sería el sucesor de Juan Pablo II; Marcos López-Caniego, el *root* y compañero de habitación en muchas escuelas; Marcos Cruz, el gran experto en Diplomacia con mayúsculas; Carlos “Chals“ Monteserín, un gran conocedor de la lengua castellana; Jacobo Ebrero, un visionario con profundos conocimientos de la actualidad española; Luis, un gran entendido en equipos de fútbol extranjeros; Raquel, la experta en idiomas siempre dispuesta a ayudarme a mejorar mi pronunciación y mi escritura inglesas; Biuse, la primera víctima a la que pongo “deberes” que además siempre los hace, y Raúl, con quien comparto gran admiración por ciertos personajes del universo *Star Wars*. Llegados a este momento, creo que dejaréis que añada mi pequeña contribución al *Altar*.

Finalmente quiero dar las gracias a los demás miembros del grupo como José Luis, Chema, Pier Paolo, Ángel, y los más recientemente incorporados Patxi y Francesco ... a todos, gracias.

Universidad de Cantabria

Departamento de Física Moderna

CSIC - Universidad de Cantabria

Instituto de Física de Cantabria

Constraints on local primordial non-Gaussianity with cosmic microwave background data

A dissertation submited for the conferment of

the degree of Doctor of Philosophy in Physics by

Andrés Curto Martín

2009

Prologue

The Gaussianity of the cosmic microwave background (CMB) anisotropies is analysed in this thesis. In particular we focus on the possible non-Gaussian deviations generated during the inflationary period, usually known as the primordial non-Gaussianity. The measurements of the anisotropies in the CMB temperature and polarization fluctuations provide information about the universe as for example its age, geometry and components. The search of primordial non-Gaussian deviations, usually characterised through the non-linear coupling parameter f_{nl}, has become a question of considerable interest since it can be used to discriminate different inflationary scenarios. We have analysed the data from the Archeops balloon-borne experiment and the Wilkinson Microwave Anisotropy Probe (WMAP) experiment in search of non-Gaussian deviations. We have used different statistical tools as for example the Minkowski functionals, the spherical Mexican hat wavelet and the smooth tests of goodness-of-fit. For both experiments we have imposed constraints on the f_{nl} parameter providing values which are compatible with results obtained with independent methods. The results favour the standard inflation which is the most successful inflationary theory since many of its predictions have been confirmed with different and independent observations.

The thesis is organised as follows. We start with an introduction where we describe general questions about the CMB, the anisotropies, and the most relevant inflationary models for the problem of non-Gaussianity. The Chapter 2 is devoted to a Gaussianity analysis of the Archeops data at low angular resolution with the smooth tests of goodness-of-fit and the Minkowski functionals. In Chapter 3 we analyse the Archeops data at higher resolutions and impose constraints on the non-linear coupling parameter f_{nl}. The Chapter 4 presents constraints on f_{nl} with WMAP data using third order statistics based on the spherical Mexican hat wavelet. The Chapter 5 is a continuation of the previous chapter. Here we use all the possible third order statistics based on the spherical Mexican hat wavelet obtaining improved constraints on f_{nl}. In the Chapter 6 we study the relationship between wavelets and the bispectrum of the primordial non-Gaussianity. The conclusions of this thesis are presented in Chapter 7. At the end of the thesis, a summary in Spanish language is included.

Contents

List of Figures

List of Tables

CHAPTER 1

Introduction

1.1 The Cosmic Microwave Background Radiation

1.1.1 An overview of the CMB

When we observe the extraterrestrial electromagnetic background radiation at wavelengths in the range of millimeters to centimeters, we observe an isotropic component. This is the cosmic microwave background (CMB) radiation. This radiation uniformly fills the space and its spectrum is very close to a thermal Planck form at 3 K which suggests a thermodynamic equilibrium. This could not have happened in our present universe as it is transparent to electromagnetic radiation. The standard interpretation is that the CMB offers a snapshot of the universe when it was only 400,000 years old. This radiation last scattered off the free electrons at that epoch and then travelled freely through space. Before the last scattering the electrons and the photons were in thermal equilibrium and this explains that the photons have a black body spectrum. Figure 1.1 shows the CMB radiation spectrum from the Far Infrared Absolute Spectrophotometer (FIRAS) instrument installed on board the Cosmic Background Explorer (COBE) satellite [124]. This spectrum, for a frequency ν, fits very well with the Planck function

$$I(\nu, T_0) = \frac{2h\nu^3/c^2}{e^{h\nu/(K_B T_0)} - 1} \tag{1.1.1}$$

that only depends on the temperature of the system T_0, and the fundamental constants c, h and K_B. The results from COBE measurements are that $T_0 = 2.725 \pm 0.010$ K [64].

The discovery of the CMB favored the theory of the Big Bang proposed by

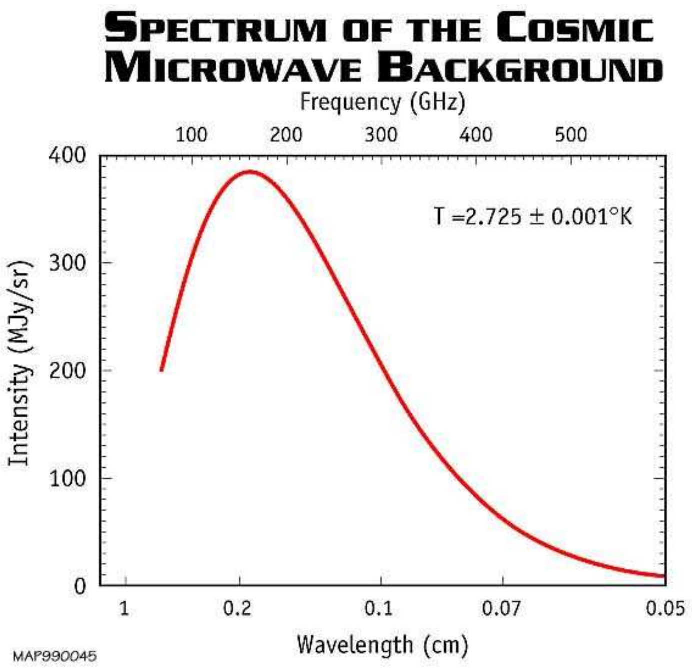

Figure 1.1 CMB black-body spectrum as measured by the FIRAS instrument on board the COBE satellite. From the Legacy Archive for Microwave Background data Analysis (LAMBDA) web site (http://lambda.gsfc.nasa.gov/).

Gamov and collaborators [5] against other alternatives as for example the theory of the Steady State Universe proposed by Hoyle, Bondi and Gold [22, 82]. According to the Big Bang theory, the Universe was formed thousands of millions of years ago starting from a tremendously dense and hot state. The theory explains the abundance of light elements (primordial nucleosynthesis), and the expansion of the Universe which was observed by E. Hubble in 1929 [83]. In addition an isotropic background radiation of the order of 5 Kelvin was predicted. It would represent a relic radiation of the hot early Universe which cooled from around 3,000 K down to about 5K due to the expansion of the Universe. More than a decade later, in 1965, Penzias and Wilson [138] detected the CMB radiation accidentally and R. Dicke, P.J.E. Peebles, P.G. Roll, & D.T. Wilkinson [49] interpreted this radiation as a signature of the Big Bang.

After the discovery of the CMB, a large number of experiments were conducted to characterise this radiation. It was in the late 1980's and early 1990's when an important step forward was made. In 1989 the COBE satellite was launched producing a great advance for the CMB field. The FIRAS instrument installed on board the satellite measured the CMB intensity in a wide frequency range

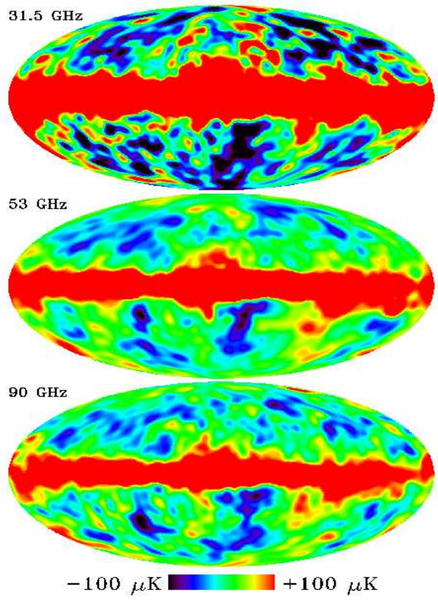

Figure 1.2 CMB anisotropies as measured by COBE, obtained at three frequencies (31.5, 53, and 90 GHz) after the dipole subtraction. From the LAMBDA web site.

(see Fig. 1.1). The Differential Microwave Radiometer (DMR) instrument provided the first full sky image of the CMB temperature anisotropies (see Fig. 1.2)

The success of the COBE experiment gave as a result the second Nobel Prize to CMB researchers after Penzias and Wilson. In 2006 the COBE scientists John Mather and George F. Smoot won the Nobel Prize of Physics "for their discovery of the black body form and anisotropy of the cosmic microwave background radiation".

Following COBE, the next generation of CMB experiments were intended to study in more detail the anisotropies of the CMB because of the cosmological information that they contain. The primary objective of these experiments was to find the first acoustic peak, i.e., the first angular scale with a maximum in the power spectrum of the anisotropies. After COBE, many ground based experiments, several balloon borne experiments, and one satellite experiment were carried out. As ground based experiments we can mention the Tenerife experiment [170] and the Mobile Anisotropy Telescope at Cerro Toco in the Chilean Altiplano (MAT/TOCO) [126], based on radiometers; the Degree Angular Scale

Interferometer (DASI) [72] and the Cosmic Background Imager (CBI) [151], based on interferometers; the Sunyaev-Zel'dovich Infrared Experiment (SuZIE) [32], based on bolometers; or the Python experiment [53], based on radiometers and bolometers. More recent ground based experiments are the Very Small Array (VSA) [69] and the Arcminute Cosmology Bolometer Array Receiver (ACBAR) [98]. To solve important problems as the Earth's atmospheric emission, several unmanned balloon experiments were developed, as for example the Millimeter-wave Anisotropy Experiment Imaging Array (MAXIMA), the Balloon Observations of Millimetric Extragalactic Radiation and Geophysics (BOOMERanG) experiment and the Archeops experiment (all based on bolometers). MAXIMA and BOOMERanG detected the first acoustic peak in the anisotropy [19, 73]. Archeops was able to link the large angular scales measured by COBE with the small angular scales measured by MAXIMA and BOOMERanG [16].

The National Aeronautics and Space Administration (NASA) launched in 2001 the Wilkinson Microwave Anisotropy Probe (WMAP) satellite. It is located in the L2 Sun-Earth Lagrangian point at a distance of 1.5 million km from the Earth. This satellite is intended to measure the anisotropies of the CMB at high resolution. In particular it is able to produce full sky maps of the anisotropies at resolutions of 13 arc minutes. It operates at frequencies between 23 GHz and 94 GHz and its detectors are based on the radiometer technology. The Planck satellite of the European Space Agency (ESA) was launched on May 14^{th} 2009. Planck has two instruments, the Low Frequency Instrument (LFI) based on radiometers and the High Frequency Instrument (HFI) based on bolometers. They will operate at frequencies between 30 and 857 GHz. Planck will produce all-sky maps with unprecedented resolution and sensitivity.

These experiments have provided fundamental information to have a complete picture of the Universe. In particular we have detailed information about its age, geometry and composition. The CMB anisotropies can be used to constrain the cosmological parameters that describe these properties. The results can be compared with independent measurements of these parameters (for example the large scale structure and the supernovae observations). The Λ-Cold Dark Matter (ΛCMD) model of the Big Bang is supported by all of these measurements, and therefore sometimes it is called the *concordance model*. It is the simplest known model that is in general agreement with observed phenomena. Λ is the cosmological constant that allows for the current accelerating expansion of the Universe. The nature of Λ is unknown, and it is often named dark energy. Cold dark matter is the model where the dark matter is explained as being cold (non-relativistic at the epoch of radiation-matter equality), non-baryonic, dissipation-less (can not cool by radiating photons) and collision-less (the dark matter particles interact with each other and other particles only through gravity). The model assumes a Universe without spatial curvature. It also assumes that it has no observable topology, so that the Universe is much larger than the observable particle horizon. These are predictions of cosmic inflation. The model uses the Friedmann-Lemaître-Robertson-Walker (FLRW) metric, the Friedmann equations and the cosmological equations of state to describe the Universe from the end of the inflationary epoch to present time and the future. This model also tells us how was the Universe in the past. In particular we know that about 14 billions (10^9) years ago the Universe was on a state of *infinite* temperature and density. In this moment the current laws of physics, the concept of time and space, break down. From that singularity, widely known as the Big Bang, to approximately 10^{-43} seconds, the physics are poorly understood (in special because we are not able yet to reproduce these conditions in a laboratory). After this time, also known as Planck time we have a clear picture of what happened. The Universe was filled homogeneously and isotropically with interacting radiation and matter. The temperature, density and pressure were very high and the Universe expanded very rapidly. The *inflationary* models were proposed originally to explain certain open questions of the Big Bang theory. Among many important predictions, they suggest that the Universe suffered a exponential expansion up to 10^{-35} seconds after the Big Bang. In particular, the anisotropies in the CMB have a particular pattern which has been predicted by the inflation (see Dodelson [51], Liddle & Lyth [108]). After the inflationary period, the universe was very hot and the matter was in a plasma state formed by the quarks and other fundamental particles. About 10^{-5} seconds after the Big Bang the first baryons were formed. Then the electrically neutral atoms were not formed until the temperature of the Universe was of the order of 3000K, 400,000 years after the Big Bang. In that moment, radiation and matter were decoupled and the photons were scattered in all the directions. These photons are the CMB photons and have been travelling freely through the Universe from that moment.

1.1.2 The anisotropies of the CMB

We know that the Universe is not perfectly isotropic and homogeneous, though it is very close to it on large scales. The COBE spacecraft detected in 1992 small fluctuations or anisotropies in the CMB [154]. These anisotropies have an amplitude of $\Delta I/I \sim 10^{-5}$ on an angular scale of 10 degrees [111]. The simplest interpretation is that they correspond to irregularities at the last scattering surface in the time of recombination. As these irregularities have a characteristic scale larger than the size of the horizon at that time, they are not causally formed and therefore they must be introduced *ad hoc*, they must be part of the initial conditions. The inflationary cosmology [2, 70, 105, 106] is able to explain these inhomogeneities, and its predictions fit very well with the most precise observations of the anisotropies performed by WMAP [97].

Although the CMB anisotropies are dependent on the position and the time, we can observe them only here and now. Note that the small excursions from this space-time point (considering for example the position of WMAP and the position of the Earth and the observations performed over the past 40 years) are insignificant with respect to the scales over which the CMB temperature varies. Therefore we are only interested in the direction of the incoming radiation, $\vec{n}$, which can be characterised by two coordinates θ and ϕ as for example our latitude and longitude on the Earth's surface. Thus the temperature anisotropies of the CMB observed in any direction can be expanded in terms of the spherical harmonics $Y_{\ell m}(\theta, \phi)$

$$\frac{T(\theta,\phi) - T_0}{T_0} = \sum_{\ell=1}^{\infty} \sum_{m=-\ell}^{\ell} a_{\ell m} Y_{\ell m}(\theta, \phi) \tag{1.1.2}$$

where $T(\theta, \phi)$ is the temperature of the CMB radiation in the direction defined by θ and ϕ, $T_0 = 2.725$ K is the average temperature of the CMB today (also known as monopole) and $a_{\ell m}$ are the spherical harmonics coefficients ($\ell = 0$ corresponds to the monopole, $\ell = 1$ dipole, $\ell = 2$ quadrupole, etc). One of the predictions of the standard, single field, slow roll inflation is that the anisotropies are compatible with a nearly Gaussian random field. In this case, all the cosmological information of the anisotropies is contained in the power spectrum C_ℓ, defined as the variance of the $a_{\ell m}$. It is also satisfied that

$$\langle a_{\ell m} a^{*}_{\ell' m'} \rangle = C_\ell \delta_{\ell \ell'} \delta_{m m'} \tag{1.1.3}$$

where $\langle \rangle$ means average over many Gaussian samples. Note that for large ℓ

we have many $a_{\ell m}$ and therefore we can sample very well their distribution. This does not occur for low multipoles. This fundamental uncertainty in the knowledge of the C_ℓ, most pronounced at low multipoles, is known as the *cosmic variance*. This error scales as the inverse of the square root of the number of possible samples

$$\frac{\Delta C_\ell}{C_\ell} \equiv \frac{\sigma(C_\ell)}{C_\ell} = \sqrt{\frac{2}{2\ell+1}} \tag{1.1.4}$$

The two point correlation function also can be used to characterise the anisotropies in the Gaussian case.

$$C(\alpha) = \left\langle \frac{\Delta T}{T}(\theta_1, \phi_1) \frac{\Delta T}{T}(\theta_2, \phi_2) \right\rangle = \sum_{\ell m} \sum_{\ell' m'} \langle a_{\ell m} a^*_{\ell' m'} \rangle Y_{\ell m}(\theta_1, \phi_1) Y_{\ell' m'}(\theta_2, \phi_2) \tag{1.1.5}$$

where α is the angular distance between the directions (θ_1, ϕ_1) and (θ_2, ϕ_2). The angular correlation is related to the power spectrum via the Legendre transform

$$C(\alpha) = \sum_{\ell} \frac{2\ell+1}{4\pi} C_\ell P_\ell(cos(\alpha)) \tag{1.1.6}$$

where P_ℓ are the Legendre polynomials. The ΛCDM model provides the values of the power spectrum given the values of the cosmological parameters. There are several codes available on the web that compute the power spectrum given a set of cosmological parameters, as for example CMBFAST [150]. In figure 1.3 we can see the ΛCDM power spectrum that best fits the data obtained by WMAP (red line) and the measurements of the power spectrum as measured by different experiments. Notice the agreement between the model and the observations. The anisotropies that we observe today have been formed by different processes at different times. They are usually classified in primary anisotropies (produced at the last scattering surface and before) and secondary anisotropies (produced after the last scattering surface).

The primary anisotropies are formed in a context where the radiation and the matter are interacting. The radiation pressure in the photon-baryon plasma tends to erase anisotropies, whereas the gravitational attraction of the baryons tries to make dense haloes. These two effects compete to create acoustic oscillations which gave the power spectrum its characteristic peak structure. The peaks correspond, roughly, to resonances in which the photons decouple when a particular mode is at its maximum amplitude. The peaks as well contain interesting physical information. At large scales, the dominant effect is the Sachs-Wolfe effect [145], due to variations in the gravitational potential. Another im-

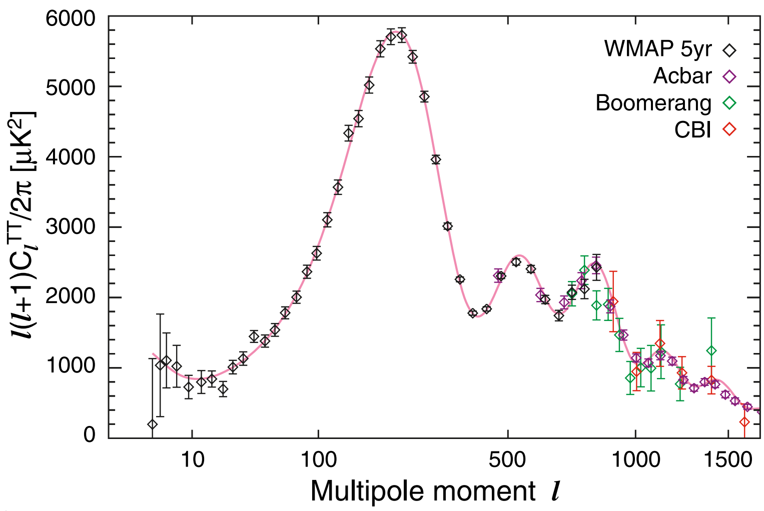

Figure 1.3 The angular power spectrum from the WMAP 5-yr data and recent results from the ACBAR, CBI and BOOMERanG experiments. The red curve corresponds to the best-fit ΛCDM model of the WMAP data. From the LAMBDA web site.

portant contribution to the primordial anisotropies is the diffusion damping. It occurs when the primordial photon-matter plasma begins to disappear, at the beginning of the decoupling phase [152]. The diffusion damping contributes to the suppression of anisotropies on small scales, and give rise to the characteristic exponential damping tail seen in the power spectrum.

The secondary anisotropies are generated after the last scattering surface. They are due to the interactions of the CMB with neutral and ionised matter in its journey through the universe. The ionised matter was produced during a epoch called *reionisation*. The first stars of the young universe generated radiation that ionised the still dense intergalactic medium. The interaction of the CMB radiation with these charges tends to reduce the anisotropies and also introduces polarization on large angular anisotropies. These two effects have been detected by the recent experiments. In addition, the hot gas trapped in the clusters of galaxies contains free electrons that also interacts with the CMB distorting the black-body spectrum. The interaction with these clouds is called the Sunyaev-Zeldovich effect. There are two kinds of modification on the anisotropies: the kinematic and the thermal Sunyaev-Zeldovich effects. The first is due to the high kinetic energy of the free electrons and the second is due to the high temperature of the electrons. Finally we have the interaction with the neutral matter, basically through gravitational interaction (the integrated Sachs-Wolfe

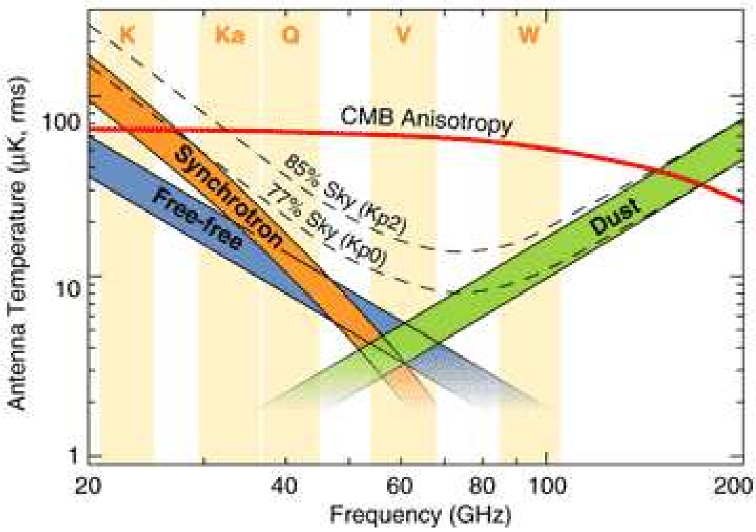

Figure 1.4 Spectra of the CMB and three known sources of foreground emission: synchrotron, free-free, and thermal dust emission. From the LAMBDA web site.

effect, the Rees-Sciama effect, the lensing effect, etc.).

1.2 Foreground contamination

The CMB radiation that we observe is contaminated with other non-cosmic microwave sources known as the *foregrounds*. The sources of this contamination are our Galaxy and the extragalactic sources. For ground based or balloon borne experiments there is an important foreground contamination coming from the Earth's atmosphere. A good understanding of the foregrounds and a proper *component separation* of the different contributions to the total microwave radiation is necessary if we want to carry out proper analyses of the CMB. In addition, the foregrounds contain very valuable astrophysical information on its own.

The galactic foregrounds are typically extensive and very strong towards the galactic plane, and therefore they affect to low multipoles ℓ. The extragalactic foregrounds consist of radio galaxies and IR galaxies. There exists a range of frequencies from around 30 GHz to 100 GHz where all the foregrounds are sub-dominant to the cosmological signal. In addition, the foregrounds have a different spectral shape to the CMB (see Fig. 1.4). In order to exploit this information, the WMAP and Planck experiments observe at different frequency channels. This allows one to fit out several foreground components against the uniform cosmological signal. The lowest and highest frequencies of these experiments are specially useful to provide accurate estimates of the foregrounds which then can be extrapolated and removed from the central frequency region. In regions where the Galaxy dominates, the foregrounds are particularly strong and difficult to remove and in many cases it is necessary to mask out these areas. Finally the instruments usually introduce more contamination to the signal that we observe in the form of noise and systematic effects. The instrumental contamination must be taken into account and understood.

There are several methods to separate the different components. These methods can be classified into methods for diffuse objects (synchrotron, free-free, etc.) and methods for compact objects, such as the point sources or the Sunyaev-Zeldovich effect. Some of the methods that have been proposed are the Wiener Filtering [23, 159], the Maximum Entropy Method (MEM) [12, 80, 81, 158, 164], Fast Independent Component Analysis (FastICA) [117, 118], Spectral Matching Independent Component Analysis (SMICA) [48, 137], Spectral Estimation Via Expectation Maximisation (SEVEM) [121], wavelets [26, 164], etc. Many regions of the sky are so contaminated by foregrounds that a reliable cleaning cannot be assured. For these cases masks are required. The WMAP team has proposed several masks for the different WMAP data releases, as for example the Kp0 mask for the 1-yr and 3-yr data [15, 78], and the KQ75 mask for the 5-yr data [79].

In the rest of this section we review the properties of the most important foregrounds. For a detailed analysis of them see for example [24, 159].

1.2.1 Synchroton

The synchrotron radiation is generated by the acceleration of ultra-relativistic charged particles when they move through a magnetic field. The radiation produced may range over the entire electromagnetic spectrum and it is distinguished by its characteristic polarization and spectrum. This radiation is more important at low frequencies and its spectrum has a power law shape ($\nu^{-\beta}$) with $2.6 < \beta < 3.1$ for WMAP frequencies. The free electrons travelling through the magnetic field of the interstellar medium generate a weak synchrotron radiation. Supernovas and active Galactic nuclei are strong synchrotron sources. Before WMAP, there was one full sky survey: the Haslam synchrotron template at 408 MHz [75]. Using different statistical techniques, the WMAP team generated an improved synchrotron template at 23 GHz for the 3-yr data [78].

1.2.2 Free-free

The free-free emission is a radiation produced by the scattering of electrons and other charged particles, such as an atomic nucleus. The free-free radiation relevant at microwave frequencies is produced by high energetic electrons at $T \sim 10^4$ K interacting with ions of the interstellar medium. This radiation is poorly known, difficult to measure and dominates in a small window of frequencies around 50 GHz. This radiation is located in hot regions with ionised hydrogen. Therefore, H_α regions are considered good tracers of free-free emission. In fact, the correlation of free-free emission with H_α can be used to create free-free templates. The WMAP team uses the H_α map assembled by Finkbeiner [63] using different surveys. Using this map and the Galactic reddening map given by Schlegel et al. [148], the WMAP team computes a best guess map of free-free emission.

1.2.3 Thermal Dust

This radiation is dominant at frequencies above 100 GHz (see figure 1.4). It is produced by grains of dust of few μm in size. The dust absorbs UV radiation from interstellar medium and re-emits that radiation in far-infrared frequencies. The thermal dust can be described with the grey body model:

$$I_\nu = I(\nu, T_D)\nu^{\alpha_D} \tag{1.2.1}$$

where $I(\nu, T_D)$ is the Planck function for a black body with a temperature T_D. This temperature is usually around 18 K and the spectral index α_D has different values $1.5 \leq \alpha_D \leq 2.5$ depending on the properties of the grains. The thermal dust emission has been studied by IRAS (Infrared Astronomical satellite) and COBE. Schlegel et al. [148] use the data of these experiments to provide a full sky dust template. The WMAP team uses a extrapolation of this map [62].

1.2.4 Extragalactic foregrounds

High precision experiments such as WMAP or Planck are affected by the contamination of extragalactic foregrounds such as the point sources. Objects that can emit microwave radiation are for example quasars, galaxies, active galactic nuclei, infrared galaxies, starbursts or spheroids. The WMAP team have identified and masked out several point sources. There are alternative catalogues of point sources [see for example 112]. However there are point sources that cannot be resolved because they are very weak although their overall influence cannot be neglected. These unresolved sources can be modelled and simulated [see for example 176].

1.3 Primordial non-Gaussianity and the CMB

The statistical properties of the CMB anisotropies are predicted by the inflationary models. In this section the physics of inflation, its imprints on the CMB and the principal sources of non-Gaussianity will be reviewed.

1.3.1 Inflation

Inflation describes an epoch of the very Early Universe between $\sim 10^{-42}$ and $\sim 10^{-36}$ seconds after the Big Bang. During the inflationary period, the universe expanded exponentially. This expansion was driven by a negative pressure. However the physics of the fields which can generate negative pressure is poorly known. Inflation answers some open questions of the Big Bang theory: the flatness of the universe, the horizon problem, the homogeneity and isotropy of the universe and the unwanted relics [108]. Quantum fluctuations in the microscopic inflationary region, magnified to cosmic sizes, become the seeds for the growth of structure in the universe.

Historically the first inflationary models were formulated by Albrecht & Steinhardt [2], Guth [70], Linde [105, 106] in the early 1980's.

Motivation

Inflation solves several problems that were noticed in the Big Bang Cosmology. These problems arise from the observation that the universe would have started from very finely tuned initial conditions at the Big Bang to reach its present status. Inflation attempts to resolve these problems by providing a dynamical mechanism that drives the universe to this special state.

The first is the *horizon problem*. We know from observation that the matter is distributed very homogeneously and isotropically on scales larger than 100 Mpc. The CMB anisotropies are as well very homogeneous and isotropic (with differences of $\sim 10^{-5}$). However there are regions of the universe so distant between them that even the light emitted from one has not yet reached the other, because the 13.7 billion years of the present universe is simply not enough time to allow it to occur. In other words, if particles are separated by distances greater than the co-moving horizon

$$\eta = \int_0^t dt/a(t) \tag{1.3.1}$$

(where t is present time and $a(t)$ is the scale factor), they could never have communicated between them. It is possible that very distant particles cannot communicate today but could in the past. This might happen if $(aH)^{-1}$, the co-moving Hubble radius (where $H = \dot{a}/a$ is the Hubble parameter), was much larger than it is today. This cannot happen in the matter and radiation epochs, when this quantity is growing. On the other hand, a decrease in $(aH)^{-1}$ implies an increase in (aH), i.e. $d(aH)/dt > 0$. Thus we have $d^2a/dt^2 > 0$. This means that in this epoch the expansion is accelerating. This is in fact the origin of the *inflation* name.

The second question is the *flatness problem*. The observations suggest that the current density of the universe is very close to its critical value at which space is perfectly flat. From the Friedmann equations we have

$$\Omega - 1 = \frac{K}{a^2 H^2} \tag{1.3.2}$$

where K is the curvature parameter, and Ω is the total density of the Universe normalised to the critical density $\rho_c = 3H/8\pi G$. As we have noticed from the horizon problem, the Hubble radius $(aH)^{-1}$ increases with the time. Therefore, as K is constant, $|\frac{K}{a^2H^2}|$ increases with time, and the same for $|\Omega - 1|$. From observations we know that today $|\Omega_0 - 1| \sim 0$. Going back in time we find that at the early times, $|\Omega - 1|$ should be very close to zero. These finely tuned initial conditions seem very unlikely.

The third question is the *magnetic monopole problem*. The observations indicate that the Early Universe was hotter and denser than the present universe. If it was very hot, a large number of heavy, stable magnetic monopoles would be produced, in according to well known particle physics theories. None of these particles has been observed in nature. Inflation solves this problem since an exponential expansion below the temperature where magnetic monopoles can be produced can dilute their density in many orders of magnitude, leaving it out of the observational levels.

Physics of standard inflation

From the microscopic point of view, inflation can be driven by one or more spin-0 particles (not observed experimentally yet). These particles are described in the usual way through a scalar field. The most interesting property of these particles is that they have an equation of state with an effective negative pressure.

Standard inflation assumes a single scalar field usually called inflaton. From fundamental physics one can obtain the energy density and the pressure of the scalar field $\phi(t)$

$$\begin{aligned} \rho &= \frac{1}{2}\dot{\phi}^2 + V(\phi) \\ P &= \frac{1}{2}\dot{\phi}^2 - V(\phi), \end{aligned} \tag{1.3.3}$$

where $V(\phi)$ is the potential of the scalar field. Substituting them in the Friedmann equation

$$H^2 = \frac{1}{3(8\pi G)}\left[V(\phi) + \frac{1}{2}\dot{\phi}^2\right] \tag{1.3.4}$$

and continuity equation

$$\ddot{\phi} + 3H\dot{\phi} = -\frac{dV}{d\phi}. \tag{1.3.5}$$

$\dot{\phi}^2/2$ is the kinetic energy of the field, and $V(\phi)$ is its potential energy. A field configuration with negative pressure is one with more potential energy than kinetic. This can be reproduced in a potential with a false vacuum, that is, a local minimum of the potential. This kind of potential was first used by Guth [70] in the early times of the inflation models. It was soon realised that this potential is not viable. The only way to migrate from the false vacuum to the true vacuum is by means of quantum mechanics. Detailed calculations [71, 76] showed that the transition from false vacuum to true vacuum does not happen at the same time, but in small localised regions. Some of these false vacuum regions expand with the inflation and never reach the true vacuum.

Subsequent models of inflation [2, 105] consider a scalar field slowing rolling towards the true vacuum. The slow-roll inflation is characterised by two parameters, ϵ and δ, defined as

$$\begin{aligned} \epsilon &= \frac{d}{dt}\left(\frac{1}{H}\right) \\ \delta &= \frac{1}{H}\frac{\ddot{\phi}}{\dot{\phi}}. \end{aligned} \tag{1.3.6}$$

These parameters are small during inflation, and the equations 1.3.4 and 1.3.5 can be written now:

$$\begin{aligned} H^2 &\simeq \frac{V(\phi)}{3(8\pi G)} \\ 3H\dot{\phi} &\simeq -\frac{dV}{d\phi}. \end{aligned} \tag{1.3.7}$$

The slow-roll approximation is valid for almost all inflationary models. For a given potential $V(\phi)$ the equations can be solved. In many cases, the process is the opposite. For a given solution, the corresponding potential is computed.

There is an important estimator of the amount of inflation. It is the ratio of the scale factor at the final time of inflation and the scale factor at some initial time. The logarithm of this quantity is the number of e-foldings:

$$N(t) = log\frac{a(t_{end})}{a(t)}. \tag{1.3.8}$$

The end of inflation is called reheating or thermalization because the large potential energy of the inflaton field decays into particles and fills the universe with electromagnetic radiation. There are three main stages in the reheating period: scalar field oscillations around the minimum of the potential, the decays of the inflaton into other particles, and finally the thermalization of the new particles.

As we have seen, inflation is able to solve the open problems of the Big Bang theory for a homogeneous universe. It as well provides a theory of inhomogeneities in the Universe which may explain the observed structures [13, 108]. The inhomogeneities arise from the quantum fluctuations of the inflaton field $\delta\phi(\vec{x}, t)$. These fluctuations can be written in terms of a Fourier expansion

$$\delta\phi(\vec{x}, t) = \sum_{\vec{k}} \delta\phi_{\vec{k}}(t) e^{i\vec{k}\vec{x}} \tag{1.3.9}$$

for a co-moving coordinate $\vec{x}$. The structures that we see today can be formed by gravitational instability only if there are small preexisting fluctuations on relevant scales which entered the Hubble radius in the radiation and matter dominated eras. This has to be put in by hand in the Big Bang model since it is impossible to produce fluctuations on scales larger than the horizon size. The key ingredient is the decreasing during inflation of the co-moving Hubble distance $(aH)^{-1}$. The physical wavelength a/k of a quantum fluctuation in the scalar field whose potential drives inflation soon exceeds the Hubble radius (i.e. $aH/k > 1$) and then freezes because the quantum fluctuations cannot operate in distances greater than the horizon.

The fluctuations of the scalar field produce primordial perturbations in the energy density, and these fluctuations are inherited by the radiation and matter which appear after inflation. Once inflation has ended $(aH)^{-1}$ increases so the fluctuations can reenter the Hubble radius.

The simplest model for inflation, i. e. the slow roll single field inflation, has well known dynamics [2, 70, 105, 106]:

- There is only one inflation field, and the fluctuations of other fields have insignificant effect in the inhomogeneities.
- The slow roll inflation takes place while scales are leaving the horizon. The inflaton field is in the vacuum state (ground state), leading to Gaussian density perturbations.
- The gravitational waves generated in the process have negligible effect on the CMB temperature anisotropies.

As we have said, the fluctuations are inherited by the matter and radiation after inflation. Considering a generic perturbation $g(\vec{x}, t)$ at a time t and a position $\vec{x}$ (as for example the CMB temperature anisotropies ΔT), we can compute its Fourier expansion:

$$g(\vec{x}, t) = \sum_{\vec{k}} g_{\vec{k}}(t) e^{i\vec{k}\vec{x}}. \tag{1.3.10}$$

As the perturbations are small after inflation, we can evolve them using perturbation theory up to first order and obtain $g_{\vec{k}}(t)$ in terms of the Fourier components of the inflaton field

$$g_{\vec{k}}(t) = T(t, \vec{k}) \times \delta\phi_{\vec{k}}(t_{end}) \tag{1.3.11}$$

where $T(t,\vec{k})$ is the transfer function, and t_{end} is a time few e-folds after inflation. This function will have an important role in the forthcoming chapters of this thesis. Here we will just say that it depends on the cosmological model, and that it can be computed numerically using for example software as CMBFAST [150] and CAMB [104].

Assuming the hypothesis of this kind of inflation, the inflaton is in its ground state and according to quantum field theory this means that each $\delta\phi_{\vec{k}}(t_{end})$ has a Gaussian probability distribution, and no correlations among different modes $\vec{k}$. This is inherited by the Fourier components of any perturbation, as for example the CMB anisotropies which have not evolved very much since their formation at the decoupling era. Thus, when analysing the statistical properties of the CMB anisotropies we are testing inflation, as it can be used to discriminate among different possible scenarios of the early universe.

1.3.2 Different scenarios with non-Gaussianities

The level of non-Gaussianity in inflationary models is usually quantified phenomenologically by the non-linear parameter f_{nl} in the primordial gravitational potential [13]

$$\phi = \phi_L + f_{nl} \star \phi_L^2 \tag{1.3.12}$$

where ϕ_L is the gravitational potential at linear order. In this section we will review the most important inflationary models and the levels of non-Gaussianity that they generate.

Standard inflation

In the standard scenario that we have described previously we have found that the primordial fluctuations are Gaussian. However small departures from Gaussianity can arise due to non-linear second order effects. In the standard inflationary model these deviations from Gaussianity are negligible and they are of the order of the slow-roll parameters [13]. The evolution of the perturbations from the end of inflation through reheating, and the radiation/matter dominated epochs leads to an observable non-Gaussianity in the CMB anisotropies of the order of $f_{nl} \sim 1$.

Curvaton scenario

The primordial perturbations in the curvaton scenario [115] are generated from the fluctuations of another completely different scalar field σ called curvaton, in a period of inflation when the contributions of the inflaton are negligible. The curvaton generates the perturbation in two stages. First, its fluctuation during inflation is converted at horizon exit to a classical perturbation with a flat spectrum. Second, after inflation, the perturbation in the curvaton field is converted into a curvature perturbation. The curvature perturbation will become relevant when the energy density of the curvaton is a significant fraction of the total density at the end of inflation. The curvaton decays into radiation at the end of the nucleosynthesis, generating a final adiabatic perturbation.

The non-Gaussianities generated in this scenario can be very relevant. Considering the fractional energy density of the curvaton at the time of its decay, $r = (\rho_\sigma/\rho_{tot})$, it can be seen that $f_{nl} \sim -5/(4r)$ for $r << 1$ and $f_{nl} \sim 3/4$ for $r \sim 1$ [13]. Note that the level of non-Gaussianities is higher for lower fractional densities of the curvaton. Assuming the existence of the curvaton and its entire responsability of the CMB anisotropies, the WMAP constraints on f_{nl} imply $\rho_\sigma/\rho_{tot} > 9 \times 10^{-3}$ at the time of curvaton decay [95].

Inhomogeneous reheating scenario

This scenario is characterised by spatial fluctuations in the decay rate Γ of the inflaton field to ordinary particles [see 13, 55]. These fluctuations produce fluctuations in the radiation and the reheating temperature in different locations of the Universe.

The level of non-Gaussianity produced here varies depending on the decay modes of the inflaton into other particles. Thus for example, if the decay rate is similar to H during inflation, the efficiency to generate density perturbations can be very small and the non-Gaussianities are expected to be high.

Multiple field inflation

It is difficult to accept that only one scalar field plays a significant role during inflation, specially from the point of view of particle physics, where it is common to have many different particles interacting. There are models that propose several fields producing density perturbations [see for example 107]. However, if more than one scalar field is accepted, one must also consider the interactions among the different scalar fields. These interactions give rise to new quantum fluctuations in the scalar fields, the *oscillation mechanism* [see 13, and references therein]. The non-Gaussianities arise in these models because nothing prevents the coupling of the inflaton with other scalar fields out of slow-roll conditions. If these interactions are sizable, they can represent a potential source of non-Gaussianities. Depending on the properties of the interacting scalar fields f_{nl} ranges from values $\sim 10^{-2}$ to higher values ~ 10 that can be measured by CMB experiments as Planck. Other ways to check the level of non-Gaussianities in multi-field inflation models is through correlations of third and higher orders [20].

Warm inflation

In the *warm inflation* the thermal equilibrium is maintained during the inflation period. It is characterised by the presence of dissipative effects during inflation so radiation is generated simultaneously with the inflationary expansion [13, 18]. The presence of radiation during inflation influences the production of inhomogeneities. The levels of non-Gaussianity for this model are of the order of $f_{nl} \sim 10^{-2}$.

Ghost inflation

The *ghost inflation* has a scalar field with the property of having a velocity that does not redshift to zero as the universe expands. This kind of field leads to interesting modifications of the gravity at large scales [8, 13]. The size of the perturbations is parametrically different from standard slow-roll inflation, and the inflation happens at lower energies. The f_{nl} parameter has values $f_{nl} \sim 100$, not much greater than the present WMAP constraints.

DBI inflation

The *DBI inflation* is based on the motion of a D-brane travelling down a higher-dimensional space-time. Here the inflaton is naturally slowed with steep potentials, in contrast with usual slow-roll inflation [13, 102, 153]. f_{nl} has a non-trivial momentum dependence although in certain conditions it can be rather large.

Other set-ups that generate non-Gaussianity or anisotropy

There are other scenarios that can generate large amounts of non-Gaussianity. Here we list some models that may present non-Gaussianities.

Topological defects are also able to imprint non-Gaussian features in the CMB [169]. It is known from high energy physics that symmetries that are spontaneously broken in our present Universe may be present in the early Universe because of field interactions. When a symmetry is restored in the early Universe and then spontaneously broken, topological defects may form. Different types of defects were predicted depending on the broken symmetry. Topological defects are high-energy phenomena that can leave imprints in the CMB as for example hot or cold spots. Cruz et al. [41] claim that a non-Gaussian cold spot detected in WMAP data is compatible with having been caused by a particular kind of topological defect called texture.

The geometry and the topology of the universe affect the CMB anisotropies. Small deviations from the Friedmann-Robertson-Walker metric can lead to noticeable signatures in the CMB anisotropies. The effect of the topology on the Gaussianity of the CMB is reviewed in Martinez-Gonzalez [122]. We can mention the homogeneous and anisotropic models for the metric of the universe at large scale (the Bianchi models) that can produce spirals or hot/cold spots [see for example 87]. Non-trivial topologies leave characteristic imprints in the CMB [99]. Luminet et al. [113] use a dodecahedral topology for the universe to explain some anomalies found at low multipoles of the WMAP data.

Primordial magnetic fields are potential sources of non-Gaussianity. These magnetic fields are able to induce perturbations on the CMB anisotropies if their amplitude is 10^{-8} G or higher [54]. The Alfvén turbulence at the epoch of recombination, caused by a statistically isotropic and homogeneous primordial magnetic field, induces correlations in the CMB anisotropies, in particular for those multipoles with $\Delta l = 2$ [54]. In addition this turbulence has non-Gaussian properties due to the quadratic dependence of the vorticity on the magnetic field [133]. An analysis on WMAP data by Naselsky et al. [133] showed no significant contribution of these magnetic fields to the CMB anisotropies.

1.4 Methods to test the Gaussianity

1.4.1 Goodness-of-fit tests

We describe the "goodness-of-fit technique" applied to test the Gaussianity of a set of signal-to-noise eigenmodes derived from measurements of the CMB temperature anisotropies.

Smooth tests of goodness-of-fit

Given a set of n random numbers, $\{y_i\}_{i=1}^{i=n}$, it is sometimes interesting to check whether they behave statistically according to one specific pdf, $f(y, \theta)$, that is, if the probability of finding a random number y in an interval between y_0 and $y_0 + \Delta y$, with $\Delta y \geq 0$, is given by $f(y_0, \theta)\Delta y$. A scalar or vector variable θ is introduced, which allows us to move smoothly between different pdfs in their corresponding space of normalised functions.

This statistical analysis tests the null hypothesis, $H_0 : \{\theta = 0\}$ against the alternative hypothesis, $K : \{\theta \neq 0\}$.

From the family of smooth goodness-of-fit tests, we can consider an *order k alternative* pdf $g_k(y, \theta)$, characterised by a pdf of the form [141, 142]

$$g_k(y, \theta) = C(\theta) \exp\left[\sum_{i=1}^{k} \theta_i h_i(y)\right] f(y) \tag{1.4.1}$$

θ is a set of k parameters to smoothly cover our space of pdfs, $f(y)$ is the null hypothesis pdf (e. g. the Gaussian distribution), $h_i(y)$ forms a complete set of orthonormal functions[1] on $f(y)$, and $C(\theta)$ is a normalisation constant.

The "score statistic" is used to evaluate the simple null hypothesis H_0. With this statistic one can estimate the statistical significance of θ through the "Maximum Likelihood Method". Following the notation by Aliaga et al. [3], the score statistic for this goodness-of-fit test is

$$S_k = \sum_{i=1}^{k} U_i^2 \ , \tag{1.4.2}$$

and the U_i^2 quantities are given by

$$U_i = \sum_{j=1}^{n} \frac{h_i(y_j)}{\sqrt{n}} \tag{1.4.3}$$

[1] $\int_{-\infty}^{\infty} h_i(y) f(y) h_j(y) dy = \delta_{ij}$

In the case of a Gaussian pdf, $h_i(x)$ are the "normalised Hermite-Chebyshev polynomials". If the null hypothesis is satisfied then the U_i quantities have statistically normal behaviour and therefore U_i^2 behave like a χ_1^2 distribution

$$f(U_i^2) = \frac{1}{\sqrt{2\pi U_i^2}} e^{-\frac{-U_i^2}{2}} \tag{1.4.4}$$

It is possible to write the U_i^2 statistical quantities in terms of the moments of order k derived from the set of n random numbers to be analysed, $\mu_k = 1/n \sum_{j=1}^{n} y_j^k$, [e.g. 3, 4].

We used the five first statistics U_i^2 which can be related to the k-order moments as follows,

$$\begin{aligned} U_1^2 &= n(\mu_1)^2 \\ U_2^2 &= \frac{n}{2}(\mu_2 - 1)^2 \\ U_3^2 &= \frac{n}{6}(\mu_3 - 3\mu_1)^2 \\ U_4^2 &= \frac{n}{24}(\mu_4 - 6\mu_2 + 3)^2 \\ U_5^2 &= \frac{n}{120}(\mu_5 - 10\mu_3 + 15\mu_1)^2 \end{aligned} \tag{1.4.5}$$

The first few statistics are generally the most sensitive for most applications. In our case higher order U_i^2 statistics are dominated by errors (because of the usual propagation of errors) and therefore are not very useful in practice. This is described in detail in section 2.3.

Signal-to-noise eigenmode analysis

We have described the method that is used to analyse a set of n random numbers to test whether their pdf is the normal distribution.

The next step is to compute the set of numbers to be analysed. In our case they come from the so-called "signal-to-noise eigenmodes", first introduced in the CMB field by Bond [21]. Our observational data, (the fluctuation in the temperature of the incoming blackbody radiation measured for each direction $\vec{n}$ in the sky, $\Delta T(\vec{n})/T$), can be interpreted as originating from several sources: all emissions coming from the sky (CMB signal, Galactic and extragalactic foregrounds and atmosphere) and the measured instrumental Gaussian noise [116].

The total area observed by the experiment is usually divided into equal area pixels identified by their centre direction $\vec{n}$ and to which the measurements,

$\Delta T(\vec{n})/T$, are assigned. To obtain the signal-to-noise eigenmodes, we expand the pixel values of the map, $\Delta T(\vec{n})/T$, into a linear combination in which the transformed instrumental noise (hereafter the noise) and the transformed theoretical CMB signal (hereafter the signal) are not correlated.

For the signal-to-noise decomposition it is necessary to calculate signal and noise covariance matrices. The temperature covariance between two pixels i and j is given by

$$C_{ij} = \langle \Delta T_i \Delta T_j \rangle - \langle \Delta T_i \rangle \langle \Delta T_j \rangle \tag{1.4.6}$$

where the brackets $\langle\rangle$ represent the average over several realisations of temperature anisotropy maps. Thus we can construct the signal (noise) covariance matrices, S (N), averaging over signal $\Delta T_s(\vec{n})$ (noise $\Delta T_n(\vec{n})$) realisations. Since the data represent temperature fluctuations around the mean then it is trivially satisfied that $\langle \Delta T_s(\vec{n}) \rangle = \langle \Delta T_n(\vec{n}) \rangle = 0$. Therefore, $C_{ij} = \langle \Delta T_i \Delta T_j \rangle$, the correlation matrix.

Once we select a set of n directions in the sky (pixels) and construct S and N matrices, which have the same dimension n and are symmetrical, we can compute the "signal-to-noise matrix" A

$$A = L_N^{-1} S L_N^{-t} \tag{1.4.7}$$

where L_N is the Cholesky matrix of N, defined as $N \equiv L_N L_N^t$. L_N can be obtained from the diagonalisation of the N matrix. Suppose D_N is the diagonal matrix of eigenvalues of N, and R_N is a matrix of the eigenvectors of N, related by $R_N^t N R_N = D_N$, then $L_N = R_N D_N^{1/2}$ is satisfied where $D_N^{1/2}$ is the square root matrix of D_N.

If $\vec{d}$ is the vector of dimension n representing the data assigned to the pixels in the sky, the signal-to-noise eigenmodes can be written as

$$\vec{\xi} = R_A^t L_N^{-1} \vec{d} \tag{1.4.8}$$

where R_A is the matrix of eigenvectors of A and D_A the diagonal matrix of eigenvalues of A, $R_A^t A R_A = D_A$.

The y_i quantities to be analysed with the goodness-of-fit test defined in the previous section are

$$y_i = \frac{\xi_i}{\sqrt{1 + (D_A)_i}} \tag{1.4.9}$$

It can be easily demonstrated that if the vector of data $\vec{d}$ satisfies $\langle \vec{d} \rangle = 0$ then $\langle y_i \rangle = 0$. In the case $\Delta T = \Delta T_s + \Delta T_n$, from the definition of signal-to-noise eigenmodes in equation 1.4.8, the definition of y_i in equation 1.4.9, and properties of correlation matrices, it follows that $\langle y_i^2 \rangle = 1$.

Supposing that the original map $\vec{d}$ is multi-normal, then our $\{y_i\}$ numbers keep the Gaussian character because both sets of numbers are connected by linear operations. More precisely, they follow a normal pdf with zero mean and unit variance, $N(0,1)$. Moreover, for different indexes i and j, y_i and y_j are independent.

Finally, for Gaussian data $\vec{d}$ each U_i^2 statistics, defined in equation 8.1.3, is distributed as a χ_1^2. The decision to accept or reject the null hypothesis will therefore be based on this pdf, as is seen in sections 2.4 and 2.5 when the test is applied to the Archeops and WMAP data.

1.4.2 The Minkowski functionals

The Minkowski functionals are useful tools to test Gaussianity and constrain the f_{nl} parameter [95]. Detailed theoretical information about these quantities is presented for example in Gott et al. [67], Minkoski [127], Schmalzing & Gorski [149]. Some examples of applications of the Minkowski functionals to the CMB are in Curto et al. [44, 45] for Archeops data, De Troia et al. [161] for BOOMERanG 2003 data, Gott et al. [68], Spergel et al. [156] for WMAP 3-yr data and Komatsu et al. [97] for WMAP 5-yr data.

For a random field $\Delta T(\vec{n})$ in the sphere we have three Minkowski functionals given a threshold ν. Considering the excursion set of points Q_ν where $\Delta T(\vec{n})/\sigma > \nu$ the three Minkowski functionals are: the area $A(\nu)$ of Q_ν, the contour length $C(\nu)$ of Q_ν, and the genus $G(\nu)$ (proportional to the difference between hot spots above ν and cold spots below ν). The expected values of the functionals for a Gaussian random field are [149]

$$\begin{aligned} \langle A(\nu)\rangle &= \frac{1}{2}\left(1-\frac{2}{\sqrt{\pi}}\int_0^{\nu/\sqrt{2}} exp(-t^2)dt\right) \\ \langle C(\nu)\rangle &= \frac{\sqrt{\tau}}{8} exp\left(-\frac{\nu^2}{2}\right) \\ \langle G(\nu)\rangle &= \frac{\tau}{(2\pi)^{3/2}}\,\nu\, exp\left(-\frac{\nu^2}{2}\right) \end{aligned} \tag{1.4.10}$$

where $\sigma = \sum_{\ell=1}^{\ell_{max}}(2\ell+1)C_\ell$ and $\tau = \sum_{\ell=1}^{\ell_{max}}(2\ell+1)C_\ell\ell(\ell+1)/2$. These expressions are only valid in an ideal case. In practice, we will obtain these quantities from Gaussian CMB simulations in order to take into account the noise, mask and pixel effects.

For a Gaussian random field the Minkowski functionals are approximately Gaussian distributed, therefore we can use a χ^2 statistic to test the Gaussianity of a CMB map. This statistic is computed with the three Minkowski functionals evaluated at n_{th} different thresholds.

$$\chi^2 = \sum_{i,j=1}^{3n_{th}} (v_i - \langle v_i \rangle) C_{ij} (v_j - \langle v_j \rangle) \tag{1.4.11}$$

where $\langle\rangle$ is the expected value for the Gaussian case, $\vec{v}$ is a $3n_{th}$ vector

$$(A(\nu_1), .., A(\nu_{n_{th}}), C(\nu_1), .., C(\nu_{n_{th}}), G(\nu_1), .., G(\nu_{n_{th}})), \tag{1.4.12}$$

and C is a $3n_{th}$ covariance matrix

$$C_{ij} = \langle v_i v_j \rangle - \langle v_i \rangle \langle v_j \rangle. \tag{1.4.13}$$

The Gaussianity analysis consists of computing the χ^2 statistic of the data and compare it with the value of the χ^2 statistic of a set of Gaussian simulations of the data (CMB signal plus instrumental noise).

Another important analysis is the estimation of the f_{nl} parameter. In this case, we can use a χ^2 test with the Minkowski functionals

$$\chi^2(f_{nl}) = \sum_{i,j=1}^{3n_{th}} (v_i - \langle v_i \rangle_{f_{nl}}) C_{ij}(f_{nl}) (v_j - \langle v_j \rangle_{f_{nl}}) \tag{1.4.14}$$

where $\langle\rangle_{f_{nl}}$ is the expected value for a model with f_{nl}, and $C_{ij}(f_{nl}) = \langle v_i v_j \rangle_{f_{nl}} - \langle v_i \rangle_{f_{nl}} \langle v_j \rangle_{f_{nl}}$. For low values of f_{nl} ($f_{nl} \lesssim 1500$) we have that $C_{ij}(f_{nl}) \simeq C_{ij}(f_{nl} = 0) = C_{ij}$, and therefore we can use the approximation

$$\chi^2(f_{nl}) = \sum_{i,j=1}^{3n_{th}} (v_i - \langle v_i \rangle_{f_{nl}}) C_{ij} (v_j - \langle v_j \rangle_{f_{nl}}). \tag{1.4.15}$$

The best-fit f_{nl} for the data is obtained by minimization of $\chi^2(f_{nl})$. Error bars for it at different confidence levels are computed using the Gaussian simulations.

Other than the analysis of the data at each resolution separately we can also analyse the data by combining the information at different resolutions. Assuming maps at n_{res} different resolutions we can define a vector

$$\vec{V} = (\vec{v}_1, \vec{v}_2, ..., \vec{v}_{n_{res}}), \tag{1.4.16}$$

where each v_i corresponds to the vector given by equation 1.4.12 for the resolution i. With this combined vector we can compute χ^2 statistics in the same way as in equations 1.4.11 and 1.4.15

$$\chi^2 = \sum_{i,j=1}^{3N_{th}} (V_i - \langle V_i \rangle) C_{ij} (V_j - \langle V_j \rangle) \tag{1.4.17}$$

$$\chi^2(f_{nl}) = \sum_{i,j=1}^{3N_{th}} (V_i - \langle V_i \rangle_{f_{nl}}) C_{ij} (V_j - \langle V_j \rangle_{f_{nl}}) \tag{1.4.18}$$

where $\langle\rangle$ is the expected value for the Gaussian case, $\langle\rangle_{f_{nl}}$ is the expected value for a model with f_{nl}, $N_{th} = \sum_{k=1}^{n_{res}} n_{th}^{(k)}$, $n_{th}^{(k)}$ is the number of thresholds used at resolution k, and $C_{ij} = \langle V_i V_j \rangle - \langle V_i \rangle \langle V_j \rangle$.

1.4.3 The spherical Mexican hat wavelet

Wavelets are useful tools to test Gaussianity. The most important property of the wavelets is that contrary to the harmonic analysis, where the transformed functions are located in the harmonic space, the wavelet transform keeps properties of both the real and harmonic space. The considered wavelet here is the Spherical Mexican Hat Wavelet (SMHW) as defined in Martínez-González et al. [120]. The spherical wavelets have been used in some analyses to test the Gaussianity of different data sets. We can mention the analysis of the COBE-DMR data [10, 27, 28] and WMAP data [25, 30, 38, 40, 125, 132, 165, 166, 172] among others. The SMHW can be obtained from the Mexican hat wavelet in the plane R^2 through a stereographic projection [6]. Given a function $f(\mathbf{n})$ evaluated on the sphere at a direction $\mathbf{n}$ and a continuous wavelet family on that space $\Psi(\mathbf{n}; \mathbf{b}, R)$, we define the continuous wavelet transform as

$$w(\mathbf{b}; R) = \int d\mathbf{n} f(\mathbf{n}) \Psi(\mathbf{n}; \mathbf{b}, R) \tag{1.4.19}$$

where $\mathbf{b}$ is the position on the sky at which the wavelet coefficient is evaluated and R is the scale of the wavelet. In the case of the SMHW we have that the wavelet only depends on the polar angle θ and the scale R [120]. In particular we have

$$\Psi_S(\theta; R) = \frac{1}{\sqrt{2\pi} N(R)} \left[1 + \left(\frac{y}{2}\right)^2\right]^2 \left[2 - \left(\frac{y}{R}\right)^2\right] e^{-y^2/2R^2} \tag{1.4.20}$$

where

$$N(R) = R \left(1 + \frac{R^2}{2} + \frac{R^4}{4}\right)^{1/2} \tag{1.4.21}$$

and

$$y = 2\tan\left(\frac{\theta}{2}\right). \tag{1.4.22}$$

We can compute the wavelet coefficient map given by equation 6.1.1 at several different scales R_j in order to enhance the non-Gaussian features dominant at a given scale.

1.4.4 The bispectrum

Finally we mention the bispectrum as one of the most popular techniques to look for non-Gaussianities in the CMB [36, 93, 94, 95, 97, 155, 156, 173]. Considering the $a_{\ell m}$ coefficients from equation 1.1.2, we can define the CMB angular bispectrum [93] as

$$B^{m_1 m_2 m_3}_{\ell_1 \ell_2 \ell_3} \equiv \langle a_{\ell_1 m_1} a_{\ell_2 m_2} a_{\ell_3 m_3} \rangle. \tag{1.4.23}$$

It is more useful to consider the angle-averaged bispectrum $B_{\ell_1 \ell_2 \ell_3}$, since it is the observable quantity, defined as

$$B_{\ell_1 \ell_2 \ell_3} \equiv \sum_{m_1 m_2 m_3} \begin{pmatrix} l_1 & l_2 & l_3 \\ m_1 & m_2 & m_3 \end{pmatrix} B^{m_1 m_2 m_3}_{\ell_1 \ell_2 \ell_3}. \tag{1.4.24}$$

The angle-averaged bispectrum can be written as

$$B_{\ell_1 \ell_2 \ell_3} \equiv \begin{pmatrix} l_1 & l_2 & l_3 \\ 0 & 0 & 0 \end{pmatrix} \sqrt{\frac{(2\ell_1+1)(2\ell_2+1)(2\ell_3+1)}{4\pi}} b_{\ell_1 \ell_2 \ell_3} \tag{1.4.25}$$

where $b_{\ell_1 \ell_2 \ell_3}$ is the reduced bispectrum. The bispectrum is a third order quantity in terms of the $a_{\ell m}$ multipoles. Therefore $\langle b_{\ell_1, \ell_2, \ell_3} \rangle = 0$ for a Gaussian random field. The CMB anisotropies are related to the primordial gravitational potential in the linear evolution case through the transfer function $g_{Tl}(k)$

$$a_{\ell m} = 4\pi(-i)^\ell \int \frac{d^3k}{(2\pi)^3} \Phi(\mathbf{k}) g_{Tl}(k) Y^*_{\ell m}\left(\frac{\mathbf{k}}{k}\right) \tag{1.4.26}$$

for the Fourier convention

$$\Phi(\mathbf{x}) = \int \frac{d^3k}{(2\pi)^3} e^{i\mathbf{kx}} \Phi(\mathbf{k}). \tag{1.4.27}$$

Replacing the equation 1.4.26 into equations 1.4.23, 1.4.24 and 1.4.25 the reduced bispectrum can be written as

$$\begin{aligned} b_{\ell_1 \ell_2 \ell_3} = & \left(\frac{2}{\pi}\right)^3 \int dr dk_1 dk_2 dk_3 r^2 (k_1 k_2 k_3)^2 B_\Phi(k_1, k_2, k_3) \times \\ & \times g_{T\ell_1}(k_1) g_{T\ell_2}(k_2) g_{T\ell_3}(k_3) j_{\ell_1}(k_1 r_1) j_{\ell_2}(k_2 r_2) j_{\ell_3}(k_3 r_3) \end{aligned} \tag{1.4.28}$$

where $B_\Phi(k_1, k_2, k_3)$ is the primordial bispectrum [61] defined as

$$\langle \Phi(\mathbf{k_1})\Phi(\mathbf{k_2})\Phi(\mathbf{k_3})\rangle = (2\pi)^3 B_\Phi(k_1, k_2, k_3)\delta(\mathbf{k_1} + \mathbf{k_2} + \mathbf{k_3}). \tag{1.4.29}$$

The reduced bispectrum can be computed for different primordial bispectra $B_\Phi(k_1, k_2, k_3)$ depending on the model that we are testing. Another useful quantity is the shape function, defined as

$$S(k_1, k_2, k_3) \equiv f_{nl} \times (k_1 k_2 k_3)^2 B_\Phi(k_1, k_2, k_3). \tag{1.4.30}$$

The shape function for the well known local and equilateral models [61] is

$$\begin{aligned} S^{local}(k_1, k_2, k_3) &\propto \frac{k_1^3 + k_2^3 + k_3^3}{k_1 k_2 k_3} \\ S^{equil}(k_1, k_2, k_3) &\propto \frac{(k_2 + k_3 - k_1)(k_1 - k_2 + k_3)(k_1 + k_2 - k_3)}{k_1 k_2 k_3}. \end{aligned} \tag{1.4.31}$$

There are different triangle configurations to compute the shape functions of several inflationary models that produce non-Gaussianities [61, 91].

The local model has a characteristic primordial gravitational potential given by

$$\Phi(\mathbf{x}) = \Phi_L(\mathbf{x}) + f_{nl} \times \left[\Phi_L^2(\mathbf{x}) - \langle \Phi_L(\mathbf{x})\rangle^2\right], \tag{1.4.32}$$

where $\Phi_L(\mathbf{x})$ is the linear Gaussian part of the primordial gravitational potential and f_{nl} is the local non-linear coupling parameter. It can be shown that the reduced bispectrum can be written as [93]

$$\begin{aligned} b^{local}_{\ell_1\ell_2\ell_3} = 2f_{nl} \int_0^\infty & r^2 dr (b^{(L)}_{l_1}(r) b^{(L)}_{l_2}(r) b^{(NL)}_{l_3}(r) + \\ + b^{(L)}_{l_1}(r) b^{(NL)}_{l_2}(r) b^{(L)}_{l_3}(r) &+ b^{(NL)}_{l_1}(r) b^{(L)}_{l_2}(r) b^{(L)}_{l_3}(r)), \end{aligned} \tag{1.4.33}$$

where $b^{(L)}_l(r)$ and $b^{(NL)}_l(r)$ are defined as

$$b^{(L)}_l(r) = \frac{2}{\pi} \int_0^\infty k^2 dk P_\Phi(k) g_{Tl}(k) j_l(kr) \tag{1.4.34}$$

and

$$b^{(NL)}_l(r) = \frac{2}{\pi} \int_0^\infty k^2 dk g_{Tl}(k) j_l(kr) \tag{1.4.35}$$

in a similar way as in Komatsu & Spergel [93], $P_\Phi(k)$ is the power spectrum of the primordial gravitational perturbations, $g_{Tl}(k)$ is the radiation transfer function, and $r \equiv c(\tau_0 - \tau)$, with τ the look-back conformal time ($\tau = 0$ at the origin and $\tau = \tau_0$ at present time).

The bispectrum can be used to obtain the f_{nl} value that best fits the observed data through a χ^2 test [see for example section V of 93]. The error bar of this value is determined by the Fisher matrix for f_{nl}:

$$\left(\frac{N}{S}\right)_{f_{nl}} \equiv \frac{\sigma(f_{nl})}{f_{nl}} = \frac{1}{\sqrt{F}}, \tag{1.4.36}$$

where

$$F = \sum_{2\leq\ell_1\leq\ell_2\leq\ell_3} \frac{B^2_{\ell_1\ell_2\ell_3}}{\sigma^2_{\ell_1\ell_2\ell_3}}, \tag{1.4.37}$$

$\sigma^2_{\ell_1\ell_2\ell_3} = \Delta_{\ell_1\ell_2\ell_3} C_{\ell_1} C_{\ell_2} C_{\ell_3}$, C_ℓ is the total power spectrum (including instrumental noise) and $\Delta_{\ell_1\ell_2\ell_3}$ is 1, 2, and 6 for the cases that all ℓ's are different, two of them are equal, and all are the same, respectively.

The bispectrum has been combined in an optimal estimator [96] to constrain efficiently the non-Gaussian signal due to f_{nl}. This method has been applied to the WMAP data [see for example 97, 156, 173].

1.4.5 Other methods to test Gaussianity

There are many estimators to test non-Gaussianity in the CMB. Acting in different spaces (real, harmonic or wavelet) they are able to extract relevant information from the map. Their expected values are usually calculated from simulations or analytically and then are compared with the values obtained from the data.

The simplest estimators are those directly related to the 1-point distribution function such as the skewness (S) or kurtosis (K) of the temperature field [114, 130], based on the third and fourth order moments of the distribution.

Other useful methods to characterise non-Gaussianity are those based on the N-point correlation function [56, 92], defined as the average product of N temperatures as measured in a fixed relative configuration of the sky,

$$C_N(\theta_1, ..., \theta_N) = \langle \Delta T(\vec{n}_1) ... \Delta T(\vec{n}_N) \rangle, \tag{1.4.38}$$

where $\vec{n}_1$, ... , $\vec{n}_N$ span a polygon characterised by the parameters θ_1,..., θ_N

There are studies based on the N-point probability density function of a pixelised CMB anisotropies map [see for example 168].

A different method to test Gaussianity of the CMB is based on scalar quantities on the sphere. These quantities are constructed using the first and second covariant derivatives of the field [58, 128] . These scalar quantities are good detectors of small deviations of Gaussianity as those characterised by the Edgeworth expansion [129]. The scalar quantities have been also studied for extrema [9], and excursion sets [11, 52] of CMB maps.

Other useful tools are the wavelets. Apart from the SMHW described before, we can mention planar wavelets [131, 136], the spherical Haar wavelet [10], directional wavelets on the sphere (elliptical Mexican Hat and Morlet) [125], steerable wavelets [166, 172], needlets [119, 139, 144], the ridgelet and the curvelet transforms [157] among others.

1.5 Anomalies in WMAP

Several analyses on WMAP data have claimed the detection of asymmetries and non-Gaussian features. We can mention the low multipole alignment statistics [see for example 34, 35, 101, 135], the phase correlations [31, 33], the hot and cold spots [103], the local curvature [25, 74], the correlation functions [57, 59, 60], structure alignments [166, 171], multivariate analysis [50], the variance of the map [130], the cold spot [38, 39, 40, 41, 42, 43, 165], etc.

The alignment and symmetry features among low-ℓ multipoles and the cold spot have been detected in several WMAP data releases and have been studied in detail. The alignment of low-ℓ multipoles, the asymmetries, and alignment of CMB features are somewhat related to the ecliptic plane and hence it might suggest to be due to some undetermined systematic effects. Several models have been proposed to explain the cold spot. For example it has been explained as a void [84, 85], as part of an anisotropic Bianchi VII_h model of the universe [86], as part of a finite cosmology model [1], as a cosmic texture [41], etc. The texture interpretation is favoured among the previous interpretations [42].

1.6 Outline

In this thesis we test the Gaussianity and present constraints on the local f_{nl} parameter using the CMB data of the Archeops and WMAP experiments. The analyses have been performed with the smooth tests of goodness-of-fit, the Minkowski functionals, the spherical Mexican hat wavelet and the bispectrum. In

Chapter 2 the Archeops data are analysed at low resolution and constraints on f_{nl} are imposed through the Sachs-Wolfe approximation [44]. New constraints on local f_{nl} are imposed on Archeops data using high resolution data and realistic simulations in Chapter 3 [45]. In Chapter 4 we constrain the local f_{nl} with the 5-yr WMAP data using the SMHW and certain inter-scale third order statistics [46]. Chapter 5 presents improved constraints on the local f_{nl} with the 5-yr WMAP data using all the third order combinations for several wavelet scales [47]. In Chapter 6 we study the efficiency of the wavelets to constrain local f_{nl} and link them to the bispectrum. The conclusions are drawn in Chapter 7 and finally a summary in Spanish language can be found in the last Chapter.

CHAPTER 2

Testing Gaussianity on Archeops data

We have performed a Gaussianity analysis using a goodness-of-fit test and the Minkowski functionals on the sphere to study the measured Archeops Cosmic Microwave Background (CMB) temperature anisotropy data for a 143 GHz Archeops bolometer. We consider large angular scales, greater than 1.8 degrees, and a large fraction of the North Galactic hemisphere, around 16%, with a galactic latitude $b > 15$ degrees. The considered goodness-of-fit test, first proposed by Rayner & Best (1989), was applied to the data after a signal-to-noise decomposition. The three Minkowski functionals on the sphere were used to construct a χ^2 statistic using different thresholds. The former method was calibrated using simulations of Archeops data containing the CMB signal and instrumental noise in order to check its asymptotic convergence. Two kind of maps produced with two different map-making techniques (coaddition and Mirage) are analysed. Archeops maps for both Mirage and coaddition map-making, are compatible with Gaussianity. From these results we can exclude a dust and atmospheric contamination larger than 7.8% (90% CL). Also the non-linear coupling parameter f_{nl} can be constrained to be $f_{nl} = 200\ ^{+1100}_{-800}$ at the 95% CL and on angular scales of 1.8 degrees. For comparison, the same method was applied to data from the NASA WMAP satellite in the same region of sky. The 1-year and 3-year releases were used. Results are compatible with those obtained with Archeops, implying in particular an upper limit for f_{nl} on degree angular scales.

2.1 Introduction

In this Chapter the smooth goodness-of-fit test first proposed by Rayner & Best [141] (hereafter R&BT) shall be implemented to analyse the Gaussianity of the Archeops data [44]. This method has already been applied successfully to the MAXIMA [29] and VSA experiments [4, 143]. The Archeops data will also be analysed with the morphological descriptors known as Minkowski functionals [67, 149]. Our approach is to use both methods in the Gaussianity analysis for comparison of the sensitivities of the two techniques and cross-checking of the results on the amount of dust contamination and the amplitude of the non-linear coupling parameter.

This is the first Gaussianity analysis of the Archeops experiment data. We analysed the data for one of the Archeops bolometers at 143 GHz. This bolometer is the most sensitive and one of the most relevant for CMB observations. As a complementary analysis, we present the results of the same goodness-of-fit test applied to WMAP data with approximately the same mask as that used for Archeops to check whether the results are consistent for both data sets.

This chapter has the following layout: the experiment, main properties of data sets and masks are summarized in section 2.2. Section 2.3 is dedicated to the calibration and checking of both methods with some "realistic" CMB anisotropy Gaussian simulations, where we know in advance the output of the techniques. Section 2.4 contains the Archeops data analysis as well as results. In Section 2.5 WMAP 1-year and 3-year data are analysed and compared with Archeops results. Finally in chapter 7 the main conclusions are presented.

2.2 Archeops data sets

2.2.1 The Archeops experiment

Archeops[1] is a balloon-borne experiment dedicated to measure the CMB temperature anisotropies from large to small angular scales [16, 160]. It has given the first link in the C_ℓ determination between the COBE large angular scales data [154] to the first acoustic peak as measured by BOOMERanG and MAXIMA [19, 73]. Archeops was also designed as a testbed for the forthcoming

[1] `http://www.archeops.org`

Planck High Frequency Instrument (HFI), [100]. Therefore, Archeops shared with Planck the same technological design: a Gregorian off-axis telescope with a 1.5 m primary mirror, bolometers operating at 143, 217, 353 and 545 GHz cooled down at 100 mK by a ^{3}He/^{4}He dilution designed to work at zero gravity and a similar scanning strategy. Archeops was launched on February 7$^{\text{th}}$, 2002, from the CNES/Swedish facility of Esrange, near Kiruna (Sweden). Twelve hours of high quality night data were gathered. This data corresponds to a coverage of approximately 30% of the sky, including the Galactic plane. More details about the instrument and the flight performance can be found in Benoît et al. [17] and Macías-Pérez et al. [116]. From its four frequency bands the two lowest (143 and 217 GHz) were dedicated to the observation of the CMB and the others (353 and 545 GHz) to the monitoring and calibration of both atmospheric and Galactic emissions.

In the following, we focus on the analysis of the most sensitive 143 GHz Archeops bolometer which also presents the lowest level of contamination by systematic effects.

Although the Archeops resolution is typically 10 arcmin, for this analysis we are interested in the Gaussianity of the large angular scale anisotropies. Therefore, we decided to use low resolution maps at HEALPix [65] $N_{\text{side}} = 32$ to consider scales above 1.8 degrees.

2.2.2 Data processing

We describe here briefly the way that Archeops data were processed. For a more detailed description see [116].

In the Time Ordered Information (TOI) corrupted data are flagged (representing less than 1.5% of the whole data set). Low frequency drifts, correlated to house-keeping data are removed using the latter as templates. A high frequency decorrelation is also performed to remove some bursts of non-stationary high-frequency noise. Corrected timelines are then deconvolved from the bolometer time constant and the flagged corrupted data are replaced by a realisation of noise. Finally, low time frequency atmospheric residuals are subtracted using a destriping procedure which slightly filters out the sky signal to a maximum of 5%.

Archeops-cleaned TOIs at 143 GHz are contaminated by atmospheric and Galactic dust residuals, even at intermediate Galactic latitudes. Atmospheric residuals contribute mainly at frequencies lower than 2 Hz in the timeline and follow approximately a ν^2 law in antenna temperature. Galactic dust presents a grey body spectrum at about 17 K with an emissivity of about ν^2. To suppress both residual dust and atmospheric signals, data are decorrelated using a linear combination of the high frequency photometric pixels (353 and 545 GHz) and of synthetic dust timelines.

In this study we used two kinds of map-making for the TOIs of Archeops data and of the simulations. The first one is an optimal map-making procedure called Mirage [174]. Mirage is based on a two-phase iterative algorithm, involving optimal map-making together with low frequency drift removal and Butterworth high-pass filtering. A conjugate gradient method is used for resolving the linear system. The second is a procedure that performs coaddition. This means that all TOI points corresponding to a given pixel are averaged.

To produce a CMB simulation, a random CMB map with the power spectrum that best fits Archeops data (see figure 2.1) is generated and from this map an Archeops TOI is produced. This TOI is treated with the two map-making methods described above to produce a map. To perform a noise simulation we produce a Gaussian constrained realisation of the Archeops noise power spectrum in the time domain. The TOI produced this way is then projected onto a map using the above map-making techniques.

The analysis was performed on a fraction of the Archeops observed region masking out pixels with Galactic latitude below 15 degrees, $|b| < 15^o$. The southern sky data were not included in the analysis as they are more contaminated by systematics in the form of residual stripes coming from the Fourier filtering and destriping of the data in the time domain [116] which produces ringing around the Galactic plane. The southern sky region was used in the CMB power spectrum analysis [160] because it increased significantly the signal-to-noise ratio at small angular scales. These scales are not affected by this systematic effect. This is not the case for the analysis presented in this Chapter where we are more interested in large angular scales where this systematic becomes important. In figure 2.2 we plot the region of data considered for the analysis. These data correspond to 1995 pixels (16% of the sky) from a total of 12288 pixels for a complete map at this resolution.

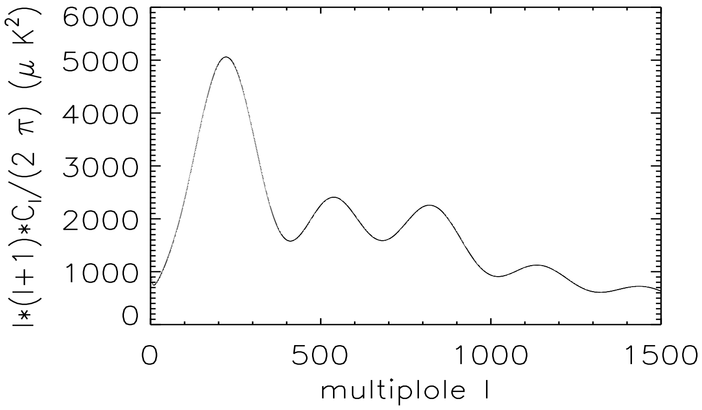

Figure 2.1 Archeops best fit power spectrum used to simulate the Archeops CMB signal.

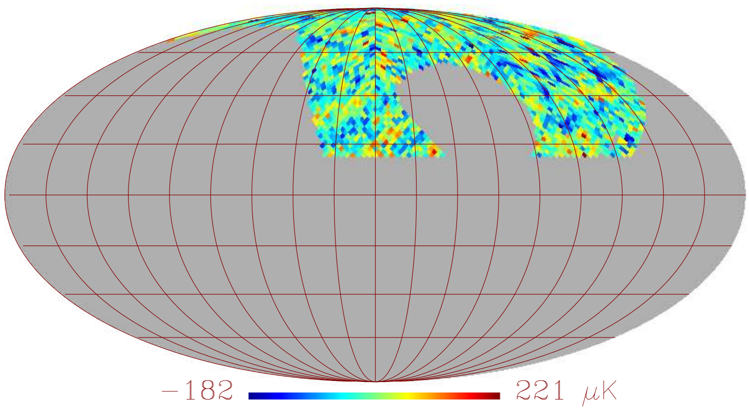

Figure 2.2 Mirage Archeops data from the best bolometer at 143 GHz presented at HEALPix resolution $N_{side} = 32$, ($\approx$ 1.8 degrees). This map is centred on Galactic longitude l = 180 degrees. Galactic and South Equator pixels have been masked. Grid lines are spaced by 20 degrees.

2.3 Calibrating the method: analysis on Gaussian simulations

To develop the R&BT non-Gaussianity test, it is necessary to calculate the signal (S) and the noise (N) correlation matrices among the selected pixels. We computed these matrices averaging simulations by means of equation 1.4.6. For this purpose Monte Carlo Gaussian simulations of Archeops CMB signal and instrumental noise were produced. The number of simulations performed for the map generated with the Mirage map-making procedure were 2.86×10^5 for the

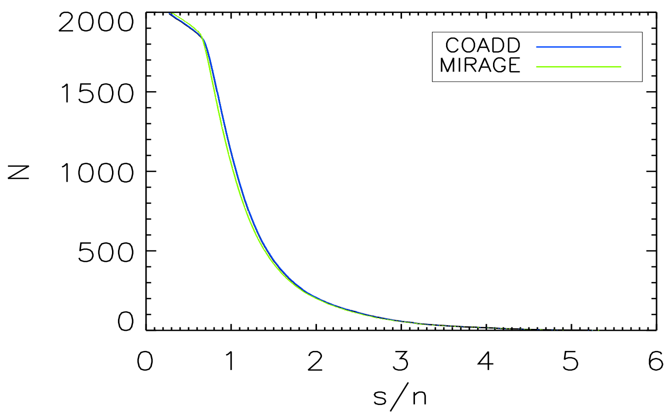

Figure 2.3 Number of normalised signal-to-noise eigenmodes y_i for which their associated A matrix eigenvalues, $(D_A)_i$, satisfy $(D_A)_i \geq (s/n)^2_c$.

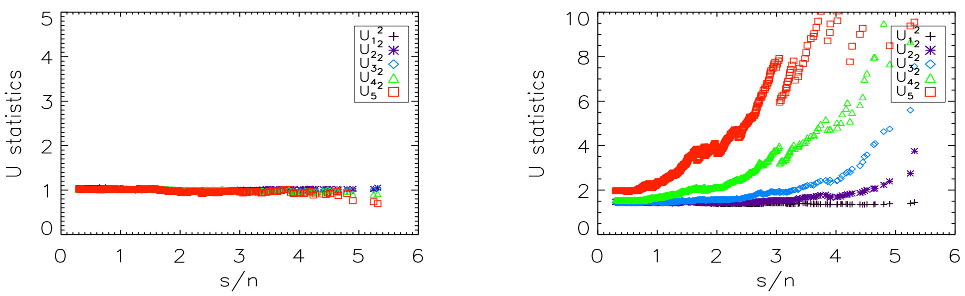

Figure 2.4 *From left to right*, mean and dispersion of U_i^2 statistics (where i goes from 1 to 5) for different signal-to-noise cuts, corresponding to 10^4 signal plus noise Mirage simulations.

signal and 2.75×10^5 for the noise, whereas for the coaddition procedure they were 5×10^5 and 5×10^5 for the signal and noise respectively. Ninety dual-core 3.2 GHz processors from the IFCA computing facilities were used. Each Mirage simulation took 180 s of real CPU time and 1.0 GB of RAM memory, whereas these values were 70 s and 0.04 GB respectively for each coaddition simulation.

The high number of simulations and the corresponding computational requirements were needed to achieve convergence in the construction of the correlation matrices. The main reason for the low convergence relies on the specific properties of our correlation matrices. Archeops noise is correlated at large scales, which means that the N matrix is neither diagonal nor sparse. The Archeops signal correlation matrix contains correlations at large scales for

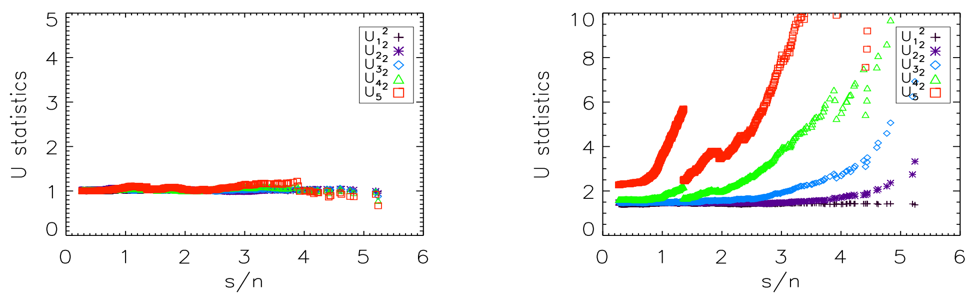

Figure 2.5 *From left to right*, mean and dispersion of U_i^2 statistics (where i goes from 1 to 5) for different signal-to-noise cuts, corresponding to 10^4 signal plus noise coaddition simulations.

which the convergence is much slower than for the small scales due to the cosmic variance. In both cases many simulations ($\sim 10^5$) were required to compute these matrices.

One way to quantify the degree of convergence of these matrices is by analysing Gaussian simulations. The U_i^2 statistics for a set of Gaussian simulations should have a χ_1^2 pdf. This can be tested, for example, by calculating the mean and the variance of the U_i^2 statistics for 10^4 Gaussian signal plus noise simulations. For the Gaussian case, the mean should be equal to 1 and the dispersion equal to $\sqrt{2}$ (this is the null hypothesis, H_0).

Following Aliaga et al. [4] and Rubiño-Martín et al. [143], the U_i^2 are computed for a subset of signal-to-noise eigenmodes which are those associated with eigenvalues of the signal-to-noise matrix A satisfying $(D_A)_i \geq (s/n)_c^2$, where $(s/n)_c$ is a given signal-to-noise ratio cut. In figure 2.3 the number of eigenmodes $\{y_i\}$'s, which obey $(D_A)_i \geq (s/n)_c^2$, in terms of s/n is plotted.

In figure 2.4 we show the mean and dispersion of the five first U_i^2 statistics for different signal-to-noise cuts corresponding to all possible eigenvalues of the A matrix. The U_i^2 values come from a set of 10^4 Gaussian Archeops signal plus noise Mirage simulations. It can be seen that for $(s/n)_c \lesssim 2$ mean values are close to 1 and the dispersion close to $\sqrt{2}$ (except for the U_5^2 statistic whose dispersion is always larger than 2). As shown by e.g. Aliaga et al. [4], the expected value of U_i^2 is equal to 1 independent of the number of $\{y_i\}$ used. This explains why the mean of U_i^2 is very close to 1 for every signal-to-noise cut. The dispersion is equal to $\sqrt{2}$ asymptotically, when the number of $\{y_i\}$ used is high. In our case, this happens for low signal-to-noise cuts, when enough $\{y_i\}$s are used

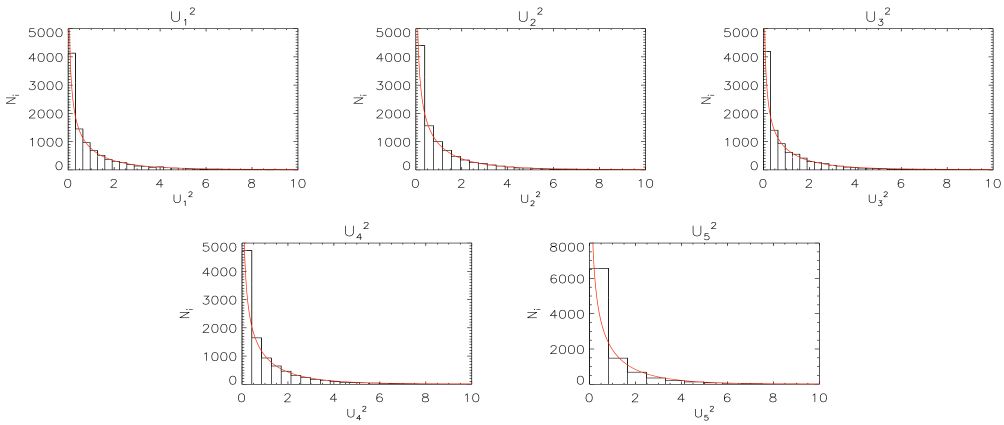

Figure 2.6 *From left to right*, and *from top to bottom*, distribution of the U_i^2 statistics, from a set of 10^4 Gaussian Mirage simulations analysed in the same region as the data (figure 2.2). The signal-to-noise cut which has been used is $(s/n)_c = 0.30$. Solid lines are the theoretical distribution (χ_1^2) normalised to the number of simulations and the size of the binned cell.

to compute the statistics. In figure 2.5 the same quantities have been plotted for the 10^4 Gaussian Archeops signal plus noise coaddition simulations. Similar conclusions can be derived in this case. Notice, however, that the results are closer to theoretical values when the analysis is performed using the Mirage maps. In this case, the correlation matrices have converged with fewer simulations than in the coaddition case. This is one of the advantages of using Mirage simulations over the coaddition ones, although the production of a Mirage map requires more CPU time and RAM memory than a coaddition map.

Since the computation of high order U_i^2 statistics involves high powers of the eigenmodes, the convergence of their dispersion to the theoretical values at a given $(s/n)_c$ is slower than for the low order ones (as seen in the right panels of figures 2.4 and 2.5).

A more exhaustive check for the convergence of the U_i^2 statistics is done by comparing their theoretical pdf with the histograms obtained from the simulated data. Given a signal-to-noise ratio cut $(s/n)_c$ for the calculation of the U_i^2 statistics, it is possible to make a histogram with the corresponding values of the U_i^2 statistics from the same sets of 10^4 simulations. Figure 2.6 compares the histograms for the first five statistics calculated using all the eigenmodes ($s/n \geq 0.30$) for the Mirage simulations with the theoretical expectation of a χ_1^2 distribution. In table 2.1 the mean and the dispersion of these histograms are

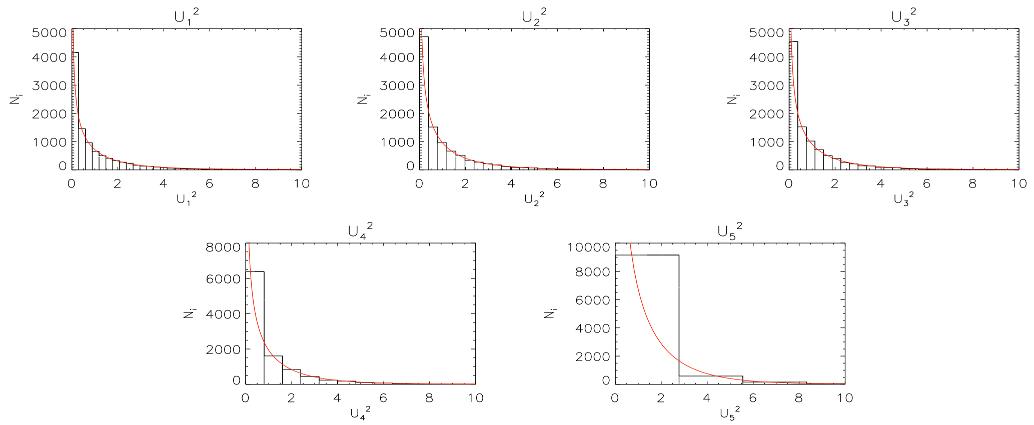

Figure 2.7 *From left to right*, and *from top to bottom*, distribution of the U_i^2 statistics, from a set of 10^4 Gaussian coaddition simulations analysed in the same region as the data (figure 2.2). The signal-to-noise cut which has been used is $(s/n)_c = 0.27$. Solid lines are the theoretical distribution (χ_1^2) normalised to the number of simulations and the size of the binned cell.

presented. In figure 2.7 the same comparison is shown for the coaddition simulations also considering all the eigenmodes ($s/n \geq 0.27$). The corresponding mean and dispersion of these histograms are given in table 2.2.

In summary, the four statistics U_1^2, U_2^2, U_3^2, and U_4^2 have pdfs compatible with the theoretical one whereas U_5^2 starts to deviate from it. The discrepancy, already present in the dispersion, increases for higher orders. The reason is that high order moments enlarge possible errors present in the computed correlation matrices and are propagated in the diagonalisation processes. In any case,

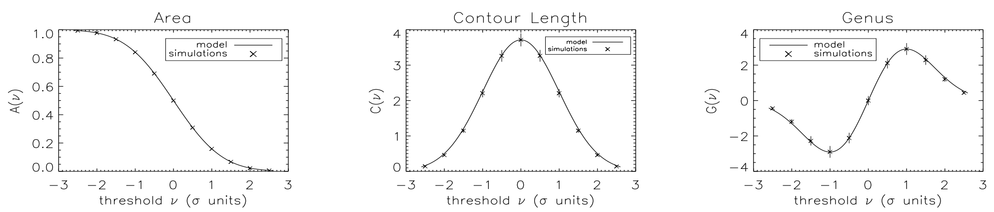

Figure 2.8 *From left to right*, mean values of the three Minkowski functionals and their corresponding error-bars for a set of 1000 (noiseless) CMB Gaussian simulations. These simulations have been generated using Archeops best fit power spectrum and have not been masked. Note the good agreement between the theoretical predictions and the results obtained from simulations.

Table 2.1 Mean and dispersion of U_i^2 statistics from 10^4 Mirage simulations for a signal-to-noise ratio cut of 0.30.

...	U_1^2	U_2^2	U_3^2	U_4^2	U_5^2	χ_1^2
μ	1.02	1.04	1.01	1.01	1.02	1.00
σ	1.45	1.47	1.43	1.55	1.96	1.41

Table 2.2 Mean and dispersion of U_i^2 statistics from 10^4 coaddition simulations for a signal-to-noise ratio cut of 0.27.

...	U_1^2	U_2^2	U_3^2	U_4^2	U_5^2	χ_1^2
μ	0.99	1.02	1.02	1.02	1.00	1.00
σ	1.40	1.47	1.48	1.62	2.27	1.41

the U_5^2 statistic can still be used for the Gaussian analysis if the distribution obtained from the simulations, instead of the theoretical one, is used as reference. Although this is not as optimal as using the theoretical χ_1^2 distribution, it is however a good compromise taking into account the huge computational resources needed to produce a very large number of simulations.

For the Minkowski functionals analysis the expected values given by equation 1.4.10 cannot be applied to our problem because of the contour restrictions of the mask and the presence of anisotropic noise. Nevertheless in order to test our Minkowski functional codes we performed an analysis on (noiseless) CMB Gaussian simulations over all sky and 1.8 degrees resolution generated using the best fit Archeops power spectrum. Analysing them for thresholds from -2.5σ to 2.5σ (where σ is the standard deviation of the corresponding simulation), we obtained results from simulations compatible with the theoretical predictions (figure 2.8).

2.4 Gaussianity test on Archeops data

We applied the R&BT to the Archeops $143K03$ bolometer map. The signal-to-noise eigenmodes were computed with the correlation matrices described in section 2.3, for each map-making case. We checked in that section that these signal and noise matrices provide U_i^2 statistics compatible with Gaussianity for Gaussian simulations.

We applied this test to the Archeops data for the Mirage and coaddition map-making. The U_i^2 statistics, computed for the 1995 pixels of the previously described Archeops data, are displayed in figures 2.9 and 2.10. The U_i^2 statistics are plotted, from i = 1 to 5, versus the signal-to-noise eigenmode cut.

For the Mirage map-making, results are displayed in figure 2.9. We can see that all the U_i^2 statistics are below 5 for all the signal-to-noise cuts. This means that the data are compatible with Gaussianity.

For coaddition map-making, we can see from figure 2.10 that whatever the signal-to-noise eigenmode cut is, U_i^2 statistics for the 143K03 bolometer data are below 5, except for U_2^2 for signal-to-noise cuts below 0.5. It reaches the maximum value of 7.97 at the minimum signal-to-noise cut of 0.27. The upper tail probability [2] for $U_2^2 = 7.97$ from the χ_1^2 distribution (equation 1.4.4) is 0.5%. Comparing with the set of coaddition Gausian simulations we found that this upper tail probability is 0.6%, (table 2.3), in good agreement with the theoretical expectation. Nevertheless, as we computed U_i^2 statistics for all possible signal-to-noise cuts, it is important to estimate the significance of finding any simulation with $U_2^2 \geq 7.97$ in at least one of them. This is the so-called "p-value" of U_2^2. The "p-value" is defined as the probability that the relevant statistic takes a value at least as extreme as that observed in the data when the null hypothesis is true. We found for U_2^2 that the "p-value" is 15.0%.

We can thus conclude that even if we have a relatively strong U_2^2 at the lowest signal-to-noise ratio, it is not improbable to have such a high value by chance. Therefore, even considering the results from the coaddition map-making, Archeops data is still compatible with our Gaussian simulations.

Although the high value found for U_2^2 for the coaddition map is not significant enough to be incompatible with Gaussianity, it is clear that there is a steady increase of U_2^2 when s/n decreases. This suggests the presence of systematics in the coaddition maps which can depend on the resolution. Moreover, the fact that it only appears in coaddition data suggests the possibility that it is a map-making issue. This also implies that systematics are better controlled in the Mirage than in the coaddition map-making. Therefore hereafter we focus only on the Mirage map-making data.

We performed a χ^2 test with the three Minkowski functionals using 11 thresholds from -2.5σ to 2.5σ. We analysed the Mirage data and a set of 1000 CMB Gaussian simulations with noise of the Mirage type. The corresponding his-

[2] $\int_a^\infty f(y)dy$

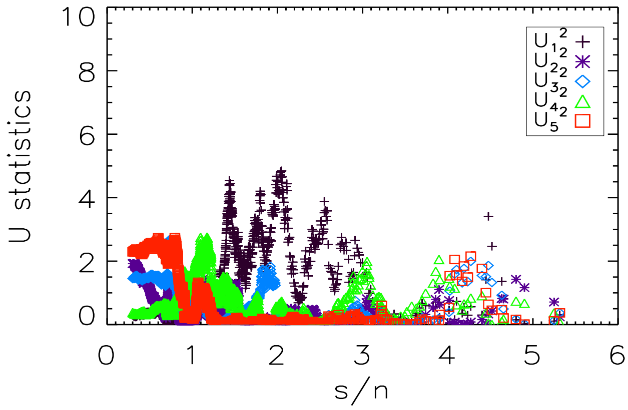

Figure 2.9 U_i^2 statistics of Mirage Archeops Data for different signal-to-noise cuts.

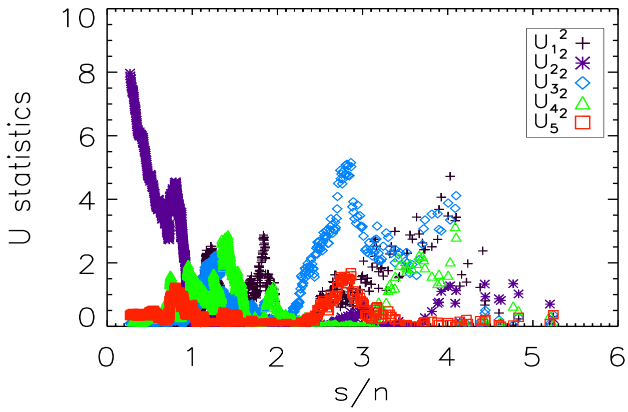

Figure 2.10 U_i^2 statistics of coaddition Archeops Data for different signal-to-noise cuts.

togram of the χ^2 values of these simulations and of the data are presented in figure 2.11. As can be seen, the data are compatible with the Gaussian simulations.

2.4.1 Systematic and foreground contamination

The R&BT can also provide a powerful tool for estimating the level of this contribution. The test consists of adding different percentages of a template map to the Archeops 143K03 bolometer map, for the Mirage and coaddition simulations cases, to compare the resulting U_i^2 statistics to those obtained with the Archeops data at 143 GHz.

Table 2.3 U_i^2 from Archeops Mirage (coaddition) map for $(s/n)_c = 0.30$ ($(s/n)_c = 0.27$) and the probability that one $s+n$ Gaussian Mirage (coaddition) simulation has a U_i^2 statistic larger than those of the data. More precisely, the probability for U_2^2 in the coaddition case is 0.6%.

...	U_1^2	U_2^2	U_3^2	U_4^2	U_5^2
Mirage	0.28	1.92	1.45	0.38	2.29
Prob.	0.60	0.17	0.23	0.54	0.12
Coaddition	0.11	7.97	0.10	0.04	0.34
Prob.	0.73	0.01	0.75	0.83	0.52

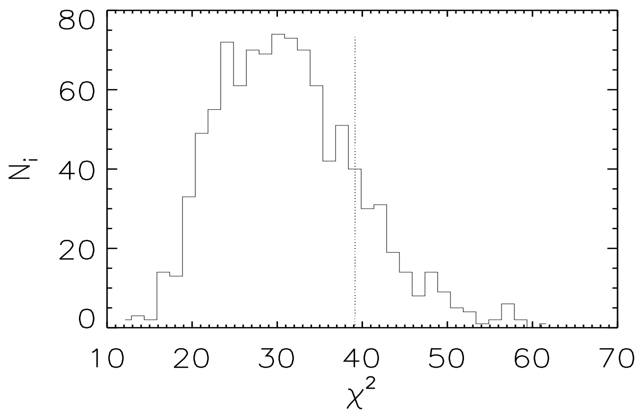

Figure 2.11 Distribution of the χ^2 values from the Minkonwski Gaussianity test for Archeops Mirage map. Vertical line shows the data results. Their cumulative probability is 83.9%.

This template map is computed from the coadded Archeops 353 GHz map [140]. This map contains thermal dust emission, atmospheric residuals as the dominant components and also instrumental noise and CMB residuals. Thus, extrapolated to 143 GHz it will provide a good template of what could be a dust plus atmospheric contamination at this frequency.

Thermal dust is assumed to have a grey-body emission: $\nu^2 B(\nu)$ which can be approximated in the Rayleigh-Jeans domain to $T_{\rm RJ} \propto \nu^2$ [140]. The atmospheric residuals emission law has been estimated empirically by the Archeops collaboration [116] and is also proportional to ν^2 in the Rayleigh-Jeans domain. Dust and atmospheric residuals being the two main components, the Archeops 353 GHz map has been extrapolated to 143 GHz by assuming this emission power

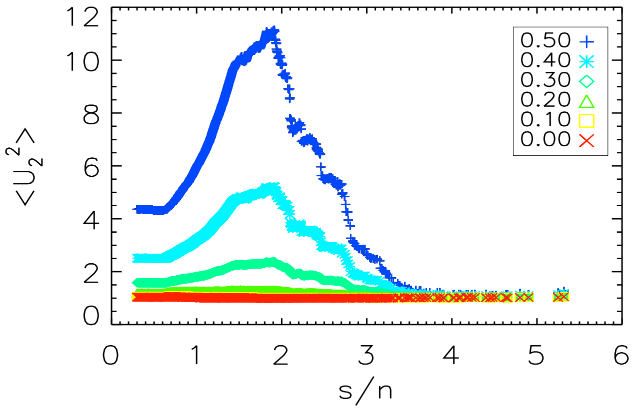

Figure 2.12 Mean of 10^4 U_2^2 statistics, from 10^4 signal plus noise Mirage simulations plus a factor α_d times the contamination template. $0.0 \leq \alpha_d \leq 0.5$.

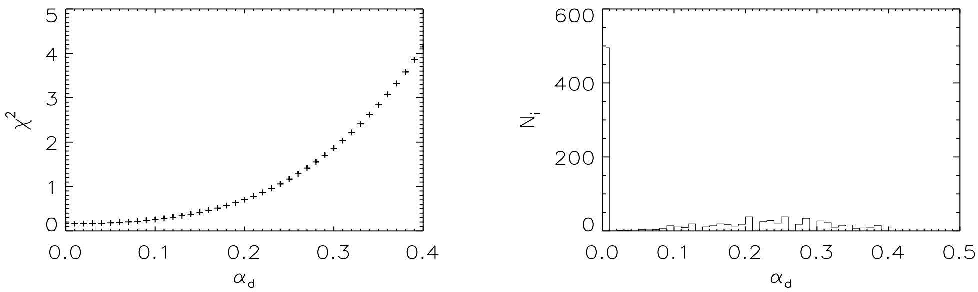

Figure 2.13 *From left to right,* χ^2 value of Archeops data for different α_d and the histogram of best fit α_d for a set of 1000 Gaussian simulations without dust. These results have been obtained with the U_2 statistic.

law. Due to the extrapolation, the CMB contribution on the 353 GHz template map is negligible with respect to the CMB at 143 GHz.

U_2^2 statistic is the most sensitive to this effect as can be seen in figure 2.12 for the Mirage case where this statistic presents a prominent peak at signal-to-noise ratio cuts around 1.88.

To determine the level of contamination we performed a χ^2 test with the U_2 statistic computed at $(s/n)_c = 1.88$. It is optimal to perform a χ^2 test with U_2 because U_2 is normally distributed for the null hypothesis. Thus we can define

$$\chi^2(\alpha_d) = \frac{1}{\sigma^2_{\alpha_d}(U_2)} (U_2 - \langle U_2 \rangle_{\alpha_d})^2 \tag{2.4.1}$$

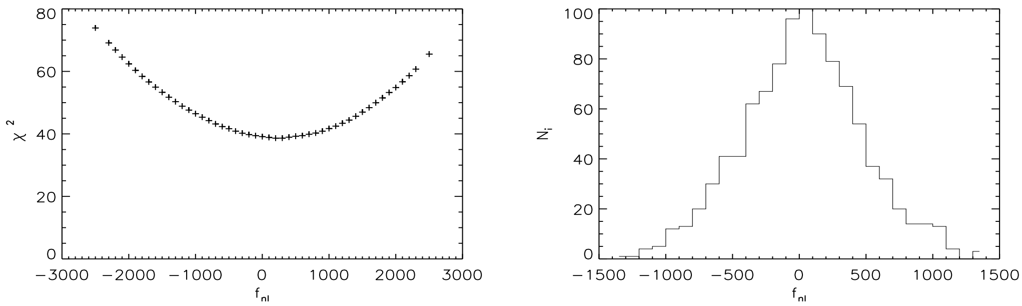

Figure 2.14 *From left to right,* χ^2 value of Archeops data for different f_{nl} and the histogram of best fit f_{nl} for a set of 1000 CMB Gaussian simulations with noise. Results were obtained with the Minkowski functionals.

where $\langle U_2 \rangle_{\alpha_d}$ and $\sigma_{\alpha_d}(U_2)$ are the mean and the dispersion of U_2 for CMB Gaussian simulations with noise plus a factor α_d times the contamination template. In the left panel of figure 2.13 we present the χ^2 of Archeops Mirage data for different α_d. We can see that the minimum χ^2 (best fit) occurs for α_d=0.0. Analysing Gaussian simulations without dust we find that most of them reach the best fit for low values of α_d (right panel; figure 2.13). Specifically $\alpha_d \leq 0.27$ for 90% confidence level (CL), and $\alpha_d \leq 0.33$ for 95% CL. By comparing the dispersion of both maps, Archeops and 0.27 times the contamination template, we can exclude a dust plus atmospheric contamination larger than 7.8%.

We computed another χ^2 statistic using the Minkowski functionals for the dust analysis. In this case

$$\chi^2(\alpha_d) = \sum_{i,j} (\vec{v}(i) - \langle \vec{v}(i) \rangle_{\alpha_d}) C^{-1}_{ij} (\vec{v}(j) - \langle \vec{v}(j) \rangle_{\alpha_d}) \tag{2.4.2}$$

i and j cover 11 thresholds from -2.5σ to 2.5σ and the three Minkowski functionals. $\langle \vec{v}(i) \rangle_{\alpha_d}$ is the mean value of the corresponding functional at the corresponding threshold for Gaussian CMB simulations with noise plus α_d times the dust template. C is the covariance matrix for Gaussian CMB simulations with noise. The value of α_d that best fits Archeops data is $\alpha_d = 0.0$. Analysing Gaussian simulations without dust we find that $\alpha_d \leq 0.28$ for 90% CL, and $\alpha_d \leq 0.35$ for 95% CL.

2.4.2 Primordial non-Gaussianity

There are several possible inflationary scenarios in which the primordial fluctuations are not Gaussian distributed. The idea is to work with a simple non-Gaussianity model and to impose some constraints on it. In particular, we consider the "weak non-linear coupling case" [13, 93, 109]

$$\Phi(\vec{x}) = \Phi_L(\vec{x}) + f_{nl}\{\Phi^2(\vec{x}) - \langle\Phi^2(\vec{x})\rangle\} \tag{2.4.3}$$

where $\Phi(\vec{x})$ is the primordial gravitational potential, (which satisfies $\langle\Phi(\vec{x})\rangle = 0$), $\Phi_L(\vec{x})$ is the linear random component (Gaussian distributed), and f_{nl} is the non-linear dimensionless[3] coupling parameter.

Scales larger than 1 degree are larger than the horizon scale at the recombination time, when CMB was formed [108]. In this regime it is possible to make a good approximation linking CMB fluctuations and gravitational fluctuations through the Sachs-Wolfe effect [145] $\Delta T(\vec{n})/T = \Phi(\vec{n})/3$ (notice however that a better approximation should include the integrated Sachs-Wolfe effect).

We analysed signal plus noise simulations with a f_{nl} term in this way,

$$\begin{aligned} \Delta T_s'(\vec{n}) &= \Delta T_s(\vec{n}) + \frac{3f_{nl}}{T}\{\Delta T_s(\vec{n})^2 - \langle\Delta T_s(\vec{n})^2\rangle\} \\ \Delta T(\vec{n}) &= \Delta T_s'(\vec{n}) + \Delta T_n(\vec{n}) \ , \end{aligned} \tag{2.4.4}$$

where ΔT_s is a Gaussian signal simulation, ΔT_n is a Gaussian noise simulation, $T = 2.725\ K$ and ΔT is the analysed simulation.

We performed a χ^2 analysis for the primordial non-Gaussianity similar to the dust case for both U_2 and the Minkowski functionals. The signal-to-noise eigenmodes y_i are weakly dependent on f_{nl}. It can be seen that the mean value of y_i^2 for simulations with f_{nl} is

$$\langle y_i^2\rangle_{f_{nl}} = 1 + \frac{a_i}{1+(D_A)_i} \times f_{nl} + \frac{b_i}{1+(D_A)_i} \times f_{nl}^2 \tag{2.4.5}$$

$$a_i = \frac{1}{T}\sum_{j,k}(R_A^t L_N^{-1})_{ij}(\langle s_j s_k^2\rangle + \langle s_k s_j^2\rangle)(L_N^{-t} R_A)_{ki} \tag{2.4.6}$$

$$b_i = \frac{1}{T^2}\sum_{j,k}(R_A^t L_N^{-1})_{ij}(\langle s_j^2 s_k^2\rangle - \langle s^2\rangle^2)(L_N^{-t} R_A)_{ki} \tag{2.4.7}$$

where b_i is about an order of magnitude larger than a_i for most of the s/n eigenmodes. This implies that $\langle y_i^2\rangle_{f_{nl}} - 1 \sim O(f_{nl}^2)$ which explains the low sensitivity

[3]We use the units system with $c = 1$.

of U_2 to f_{nl} variations. In particular, we found that it is much less sensitive than the Minkowski functionals. If we consider for example, a value of $f_{nl} = 2300$, we find a relative variation $(\langle y_i^2 \rangle_{f_{nl}} - \langle y_i^2 \rangle_0)/\langle y_i^2 \rangle_0 \simeq 0.05$ (and therefore a similar ratio for U_2 and U_2^2) for the former and $(\langle F^2 \rangle_{f_{nl}} - \langle F^2 \rangle_0)/\langle F^2 \rangle_0 \simeq 0.50$ for the latter.

Therefore we performed a χ^2 test with the three Minkowski functionals using different thresholds between -2.5σ and 2.5σ. In the left panel of figure 2.14 we present the χ^2 value of the data for different f_{nl} cases. We can see that the minimum χ^2 value is reached for $f_{nl} = 200$. Taking into account also the results obtained when analysing Gaussian simulations (right panel; figure 2.14) we can put the following constraints on f_{nl} from the Archeops data: $f_{nl} = 200\,^{+600}_{-300}$ at 68% CL, $f_{nl} = 200\,^{+900}_{-600}$ at 90% CL, and $f_{nl} = 200\,^{+1100}_{-800}$ at 95% CL.

2.5 Complementary analysis: WMAP in the same region

WMAP is a NASA satellite dedicated to observe the anisotropies of the CMB with high accuracy at five different frequencies between 23 and 94 GHz. Scientific results of this mission have provided us a clearer image of the early universe, and reduced the uncertainties in several cosmological parameters. Data products of this mission can be found on the web[4].

2.5.1 The WMAP data

We have analysed WMAP data with the same goodness-of-fit and the Minkowski functionals tests already used on Archeops data. The main purpose of this analysis is to compare Archeops results with a different experiment to discriminate among systematics, foreground emissions and intrinsic CMB non-Gaussian features. It is clear that the WMAP frequencies complement very well those of Archeops. A detailed analysis of the possible WMAP non-Gaussianities with this goodness-of-fit method deserves further study.

The maps we analysed were produced from the 1-year and 3-year WMAP foreground cleaned maps for the differencing assemblies corresponding to the cosmological frequencies 40, 60 and 90 GHz. The main properties of these maps are described in detail in Bennett et al. [14] and Hinshaw et al. [78] respectively.

[4] `http://lambda.gsfc.nasa.gov/`

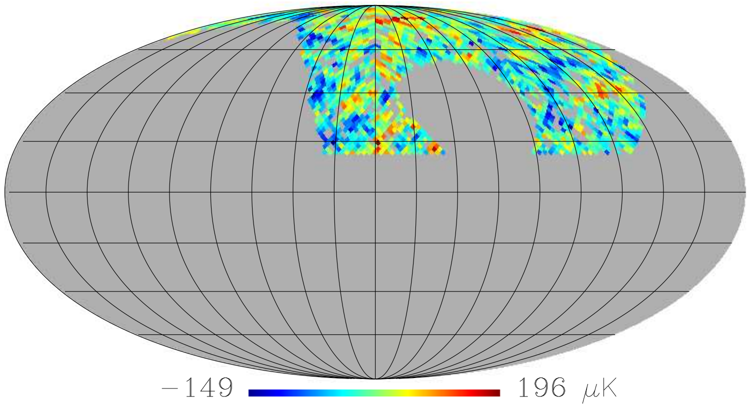

Figure 2.15 WCM3 Data at HEALPix resolution $N_{side} = 32$ (it corresponds to a pixel size of ≈ 1.8 degrees). This map is centred on Galactic longitude l = 180 degrees. The pixels contaminated by Galactic and extragalactic emission are covered with the mask described in the text. Grid lines are spaced by 20 degrees.

Specifically we have used the "combined map" as described in Bennett et al. [14], [see also 165]. The WMAP CMB simulations which are used in the analysis are also combined simulations, that is, CMB signal simulations were produced for each channel and then combined in the same manner as for the data.

According to Bennett et al. [14], WMAP noise is highly uncorrelated, that is, the noise from a given pixel i is independent of the noise from another pixel j. The noise combined simulations are produced from the "combined variance map" as shown for example in Vielva et al. [165].

We have analysed both combined maps, 1-year and 3-year (hereafter WCM1 and WCM3). The WMAP mask considered for both analyses was the 3-year Kp0 one because it is the most conservative for WCM3 and also contains the 1-year Kp0 mask. See Hinshaw et al. [78] for details about new masks and Bennett et al. [15] for original masks. The actual mask we used is the 3-year WMAP Kp0 degraded to our resolution times the Archeops mask[5]. Its number of pixels is 1648. In figure 2.15 WCM3 data is plotted using this mask.

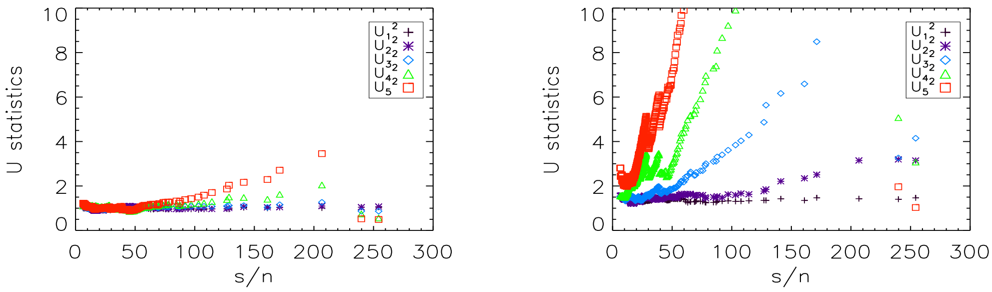

Figure 2.16 *From left to right*, mean and dispersion of U_i^2 statistics (where i goes from 1 to 5) for different signal-to-noise cuts, corresponding to 10^3 signal plus noise WCM3 simulations.

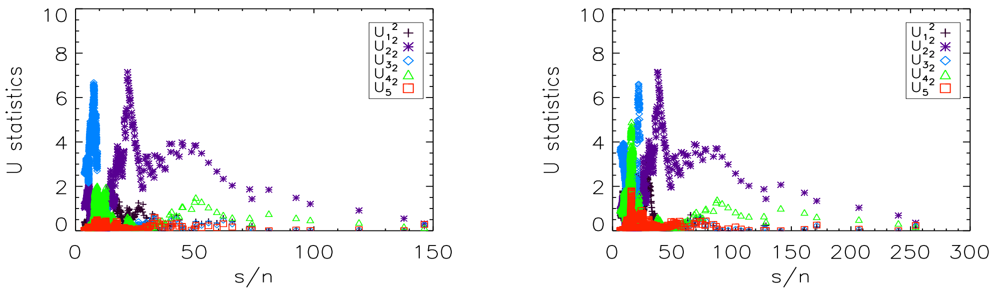

Figure 2.17 *From left to right*, U_i^2 statistics for WCM1 and WCM3 presented for different signal-to-noise cuts.

2.5.2 Gaussianity test on WMAP data

In order to perform the R&BT test on WCM1 and WCM3 maps we followed the same steps as for the Archeops analysis. We calculated their corresponding S and N matrices for the 1648 pixels available after applying the combined Archeops-WMAP mask.

We assume the best fit model of the 3-year WMAP data for both analysis, WCM1 and WCM3. At the resolution with which we are dealing, 1.8 degrees, the power spectra of the 1-year and 3-year data are very approximately the same. This assumption implies that the S matrix is the same for both releases. The S matrix is computed from 1.2×10^5 Gaussian simulations according to equation 1.4.6. Each simulation was produced in the same 90 dual core processors men-

[5] For comparison, we also repeated the goodness-of-fit analysis on Archeops data using this combined mask, finding similar results to those obtained in section 2.4 using the Archeops mask.

tioned previously, and took an average CPU time of 360 s and an average RAM memory of 0.4 GB.

As commented above, WMAP noise is highly uncorrelated and therefore we can assume that the noise matrices are diagonal. This means that the correlation element corresponding to pixels i and j is $N_{ij} = \sigma_i^2 * \delta_{ij}$, where σ_i^2 is the combined noise of pixel i. Noise matrices for WCM1 and WCM3 must be constructed with their corresponding noise variances which differ by an approximate factor of 3.

Two additional sets of 10^3 Gaussian signal plus noise simulations (corresponding to WCM1 and WCM3 maps) were performed for the calibration of the matrices. In figure 2.16, we present the mean and the dispersion of the U_i^2 statistics at different signal-to-noise cuts for the WCM3 case. Note that the numerical range for the possible signal-to-noise cuts $(s/n)_c$ is wider than for the Archeops case, because WCM3 noise is smaller than that of Archeops at this resolution. The $(s/n)_c$ range for WCM1 is approximately the same as that of WCM3 reduced by a factor $\sqrt{3}$. The mean and the dispersion for WCM1 simulations are similar to those obtained for WCM3. It can be seen that mean values of U_i^2

Table 2.4 Mean and dispersion of U_i^2 statistics from 10^3 WCM1 simulations for $(s/n)_c = 3.64$.

...	U_1^2	U_2^2	U_3^2	U_4^2	U_5^2	χ_1^2
μ	1.09	1.15	1.02	1.09	1.02	1.00
σ	1.56	1.50	1.47	1.71	2.02	1.41

Table 2.5 Mean and dispersion of U_i^2 statistics from 10^3 WCM3 simulations for $(s/n)_c = 6.33$.

...	U_1^2	U_2^2	U_3^2	U_4^2	U_5^2	χ_1^2
μ	1.00	1.18	1.04	1.10	1.22	1.00
σ	1.42	1.56	1.51	1.56	2.81	1.41

statistics are close to 1 for almost all signal-to-noise cuts and all the computed statistics, but the dispersion becomes higher than square root of two for high signal-to-noise cuts and for statistics with high order moments, such as U_5^2 and higher order statistics.

As for the Archeops case, these high values are explained by the small errors present in the computed correlation matrices plus small numerical errors in the

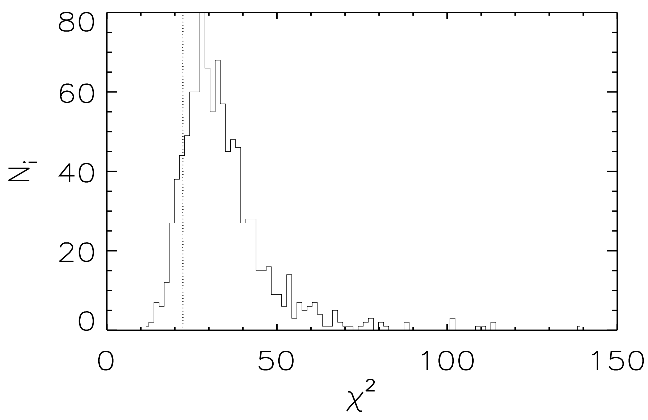

Figure 2.18 Distribution of the χ^2 values from the Minkonwski Gaussian test for WCM3 data. Vertical line shows the data results. Their cumulative probability is 12.0%.

diagonalisation of these matrices, which are amplified through the high order moments. In table 2.4 we present the mean and the dispersion of U_i^2 statistics for 10^3 WCM1 simulations with noise for all the eigenmodes ($s/n \geq 3.64$). Note how the dispersion increases with the order of the statistics. In table 2.5 the same quantities are presented for 10^3 WCM3, obtained also from all the eigenmodes ($s/n \geq 6.33$). The effect is the same for the high order moment statistics. The results for the U_i^2 statistics for WCM1 and WCM3 data maps are presented in figure 2.17. As can be seen, all U_i^2 values satisfy $U_i^2 \leq 7.15$. The upper limit 7.15 corresponds to a upper tail probability of 0.7% for the theoretical distribution. To confirm or rule out a possible non-Gaussian detection, this result should be studied more carefully. Firstly, we have that for both WCM1 and WCM3 U_2^2 is the only statistic which reaches some sharp peaks above 6.6 (which corresponds to a upper tail probability for the theoretical distribution of 1.0%). From the plots in figure 2.17, U_2^2 reaches this peak at $(s/n)_c = 21.81$ for WCM1 and $(s/n)_c = 37.92$ for WCM3. We estimated the upper tail probability for the U_i^2 statistics of the data at the mentioned signal-to-noise cut by performing 10^3 Gaussian simulations. These results are presented in tables 2.6 and 2.7. As we can see for the U_2^2 statistic, we have this probability as 1.0% and 0.7% for WCM1 and WCM3 respectively, very similar to the theoretical value.

This probability is obtained for the precise signal-to-noise cut where U_2^2 reaches its maximum. Since the width of the maxima is much smaller than the range of variation of the signal-to-noise eigenvalues, it makes sense to ask for the

Table 2.6 WCM1 U_i^2 statistics for $(s/n)_c = 21.81$, and their corresponding upper tail probabilities.

...	U_1^2	U_2^2	U_3^2	U_4^2	U_5^2
WCM1	0.90	7.15	0.32	0.63	0.09
Prob.	0.37	0.01	0.52	0.35	0.67

Table 2.7 WCM3 U_i^2 statistics for $(s/n)_c = 37.92$, and their corresponding upper tail probabilities.

...	U_1^2	U_2^2	U_3^2	U_4^2	U_5^2
WCM3	0.13	7.15	0.00	0.61	0.01
Prob.	0.73	0.01	0.95	0.36	0.88

significance of the detection. Thus, from the simulations we computed the "p-value", i.e. the probability of finding a value of U_2^2 larger than 7.15 at any signal-to-noise cut, the maximum value reached by the data. This probability is 18% for WCM1 and 17% for WCM3.

From the previous discussion, we conclude that the sharp peaks found in the data are not significant. Also, well studied cases of artificial CMB non-Gaussianities, such as skewness or kurtosis produced using the Edgeworth expansion [see 120, for applications of this expansion to the CMB non-Gaussianity analyses], usually show deviations of the U_i^2 statistics in the form of a large plateau. Besides, we note that at the signal-to-noise cuts where the maxima are found, there are fewer than 100 $\{y_i\}$ numbers to compute the U_i^2 statistics (around 70), and the test only works correctly asymptotically ($n >> 1$).

WCM3 data were also analysed with the Minkowski functionals as in the Archeops case (that is, using 11 thresholds between -2.5σ and 2.5σ and the three functionals). The histogram corresponding to the χ^2 values for 1000 Gaussian simulations and the value for WCM3 data are presented in figure 2.18. As we can see, the WCM3 data are again compatible with Gaussianity.

Finally, we performed an analysis on simulations with the f_{nl} parameter as defined in equation 2.4.4. The procedure was the same as that performed for Archeops case. As discussed in section 2.4.2, we only use the Minkowski functionals for the f_{nl} case. The χ^2 value for WCM3 data is minimum for $f_{nl} = 100$. Analysing Gaussian simulations, the constraints found for f_{nl} are: $f_{nl} = 100\,^{+200}_{-200}$ at 68% CL, $f_{nl} = 100\,^{+400}_{-300}$ at 90% CL, $f_{nl} = 100\,^{+500}_{-400}$ at 95% CL. These limits are compatible with those obtained from Archeops since the tighter constraints found for WCM3 can be explained by the significantly smaller noise in that experiment. In particular, if we analyse simulated Archeops data with noise normalised to the same amplitude as that of WCM3 we find similar limits for f_{nl}.

CHAPTER 3

Constraints on f_{nl} with Archeops data

We present a Gaussianity analysis of the Archeops Cosmic Microwave Background (CMB) temperature anisotropy data maps at high resolution to constrain the non-linear coupling parameter f_{nl} characterising well motivated non-Gaussian CMB models. We used the data collected by the most sensitive Archeops bolometer at 143 GHz. The instrumental noise was carefully characterised for this bolometer, and for another Archeops bolometer at 143 GHz used for comparison. Angular scales from 27 arcmin to 1.8 degrees and a large fraction of the sky, 21%, covering both hemispheres (avoiding pixels with Galactic latitude $|b| < 15$ degrees) were considered.

The three Minkowski functionals on the sphere evaluated at different thresholds were used to construct a χ^2 statistics for both the Gaussian and the non-Gaussian CMB models. The Archeops maps were produced with the Mirage optimal map-making procedure from processed time ordered data. The analysis is based on simulations of signal (Gaussian and non-Gaussian f_{nl} CMB models) and noise which were processed in the time domain using the Archeops pipeline and projected on the sky using the Mirage optimal map-making procedure.

The Archeops data were found to be compatible with Gaussianity after removal of highly noisy pixels at high resolution. The non-linear coupling parameter was constrained to $f_{nl} = 70^{+590}_{-400}$ at 68% CL and $f_{nl} = 70^{+1075}_{-920}$ at 95% CL, for realistic non-Gaussian CMB simulations.

3.1 Introduction

In this Chapter we shall use the Minkowski functionals [67, 127, 149] to analyse the Archeops data at high resolution [45]. This new Gaussianity analysis of the Archeops data complements the first analysis presented in Curto et al. [44] where only low resolution maps (about 1.8 degrees of resolution) were analysed and the f_{nl} constraints were imposed on non-Gaussian CMB maps simulated using the quadratic Sachs-Wolfe approximation. In this chapter the constraints on the non-linear coupling parameter f_{nl} are obtained using higher resolution (27 arcmin) Archeops data and realistic non-Gaussian simulations of the CMB fluctuations with the algorithms developed by Liguori et al. [109, 110].

This chapter is organized as follows. Section 3.2 presents the Archeops data and the Gaussian and non-Gaussian simulations performed. In Section 3.3 we perform an analysis of the instrumental noise which will provide the correct masks for our analysis. Section 3.4 is devoted to the f_{nl} constraints and the comparison with the Sachs-Wolfe approximation. We summarize and draw our conclusions in chapter 7.

3.2 Data and simulations

3.2.1 The data

We used the data collected with two bolometers at 143 GHz. We used the data of the 143K03 bolometer for the main analysis (see section 3.4) and the data of the 143K03 and 143K04 bolometers for the noise analysis (see section 3.3). However, for the f_{nl} constraints, the data from the second bolometer 143K04 are not used due to their higher noise level and worse systematic errors. The characteristics of the bolometers are described in Macías-Pérez et al. [116]. In Curto et al. [44] the Gaussianity analysis of Archeops data was performed at low resolution, in particular HEALPix [65] $N_{side} = 32$. Here we complement that work and analyse the data at the same and higher resolutions: $N_{side} = 32$, 64, and 128 using the realistic non-Gaussian simulations presented below.

First we processed and cleaned the Time Ordered Information (hereafter TOI) as described in Tristram et al. [160]. Then the data maps at different resolutions were produced using the Mirage optimal map-making procedure [174].

All the analyses presented here were performed on a fraction of the Archeops observed region after masking out pixels with Galactic latitude $|b| < 15^o$. This corresponds to 21% of the total sky. Unlike the analysis in Curto et al. [44], restricted to north Galactic latitudes, south Galactic latitudes are included in the analysis.

3.2.2 Gaussian simulations

We have performed Gaussian simulations of the CMB signal and of the Archeops noise as described in Curto et al. [44]. The noise simulations were obtained from Gaussian random realisations of the time-domain noise power spectrum of the bolometers. The constructed noise time ordered data were then projected using the Mirage optimal map-making procedure. The CMB Gaussian simulations were obtained from random realisations of the best–fit Archeops CMB power spectrum. From these maps we constructed Archeops time ordered data and then we project them using Mirage. In this way, the filtering of the Archeops data was taken into account.

3.2.3 Non-Gaussian CMB simulations

There are several alternative theories to the standard inflation theory that introduce non-Gaussian fluctuations in the CMB. One simple model that describes weakly non-Gaussian fluctuations in matter and radiation is obtained by introducing a quadratic term in the primordial gravitational potential [66, 93, 146, 162]

$$\Phi(\vec{x}) = \Phi_L(\vec{x}) + f_{nl}\{\Phi_L^2(\vec{x}) - \langle \Phi_L^2(\vec{x}) \rangle\} \tag{3.2.1}$$

where $\Phi_L(\vec{x})$ is a linear random field which is Gaussian distributed and has zero mean, and f_{nl} is is the non-linear coupling parameter. Non-Gaussianity of this type is generated in various classes of non-standard inflationary models [see, e. g. 13, for a review]. To obtain the CMB anisotropies generated by such a primordial gravitational potential we use the algorithm described in Liguori et al. [109] for the temperature maps or Liguori et al. [110] for temperature and polarization maps.

In this case the multipole coefficients a_{lm} of the CMB temperature map can be written as

$$a_{lm} = a_{lm}^{(G)} + f_{nl} a_{lm}^{(NG)} \tag{3.2.2}$$

where $a_{lm}^{(G)}$ is the Gaussian contribution and $a_{lm}^{(NG)}$ is the non-Gaussian contribution.

For our simulations we use the ΛCDM model that best fits the WMAP data and a modified version of the CMBFAST code [175] to obtain the Gaussian and non-Gaussian contributions as described above. We produced a set of 300 high resolution full sky temperature Gaussian maps ΔT_G and their complementary non-Gaussian maps ΔT_{NG} at the same resolution. The total CMB map with a non-Gaussian contribution is therefore

$$\Delta T = \Delta T_G + f_{nl} \Delta T_{NG}. \tag{3.2.3}$$

To constrain f_{nl} with Archeops data we need to transform these simulations into Archeops simulations. For this purpose, each simulated non-Gaussian map given by equation 3.2.3 was converted into Archeops time-ordered data accounting for the Archeops pointing. These time-ordered data were re-normalised to account for intercalibration errors between Archeops and WMAP[1], and added to Gaussian simulations of the Archeops instrumental noise constructed as above. Then the time ordered data was projected on the sky using Mirage. Although, the Mirage algorithm is weakly non-linear, i.e., the map obtained from ΔT_G and ΔT_{NG} separately is slightly different from the one obtained from the sum of the two contributions, we have tested that the Minkowski functionals are very similar in both cases. Thus, for our analysis, we can construct the Archeops simulations for different values of f_{nl} by adding the Mirage map for ΔT_G to the one for ΔT_{NG} multiplied by f_{nl}. This corresponds to an important saving of CPU time as the Mirage algorithm is a significantly time consuming process [44].

Thus, we transformed our sets of 300 ΔT_G and ΔT_{NG} simulations into CMB Archeops simulations (s_g and s_{ng}) at the three considered resolutions N_{side} =32, 64, and 128. The final non-Gaussian simulations accounting for f_{nl} were computed from $s_g + f_{nl} s_{ng} + n_g$ where n_g corresponds to the Archeops Gaussian noise simulations.

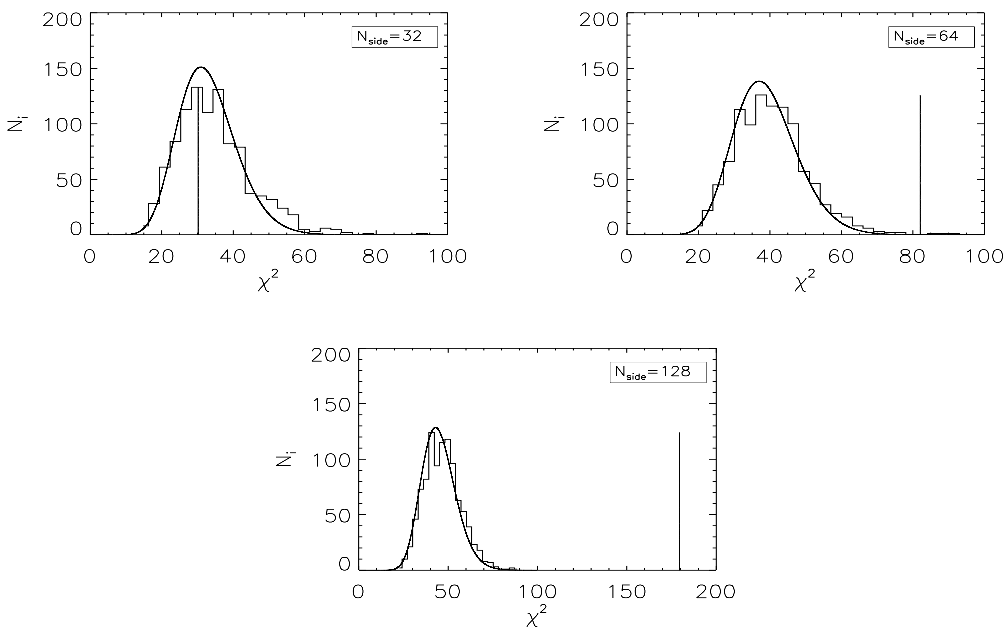

Figure 3.1 Distribution of the χ^2 values from the Minkowski Gaussianity analysis for the Archeops 143K03-143K04 map at $N_{side} = 32$, $N_{side} = 64$, and $N_{side} = 128$. The vertical lines show data, the histograms are obtained from a set of 10^3 simulations, and the solid lines are the expected χ^2 distributions for $3n_{th}$ degrees of freedom.

3.3 Gaussianity analysis of the Archeops instrumental noise

From Macías-Pérez et al. [116] it is expected that the noise at a given pixel behaves as Gaussian when the pixel has been observed a sufficiently large number of times, about 100 times. In order to check the noise behaviour, we perform a Gaussianity analysis of the Archeops instrumental noise. This is needed to exclude from the main Gaussianity analysis the possible scales and regions of the sky where the Archeops noise is non-Gaussian.

3.3.1 Two bolometer analysis

A simple way to analyse the instrumental noise is to subtract the data of two different bolometers at the same frequency so that the sky signal is removed in the final map. We used the data collected by two different Archeops bolometers at 143 GHz: 143K03 and 143K04. As the CMB contribution is the same for both

[1]The normalisation is simply obtained by multiplying the simulated TOI by a constant factor $f = 1/1.07$ as described in Tristram et al. [160].

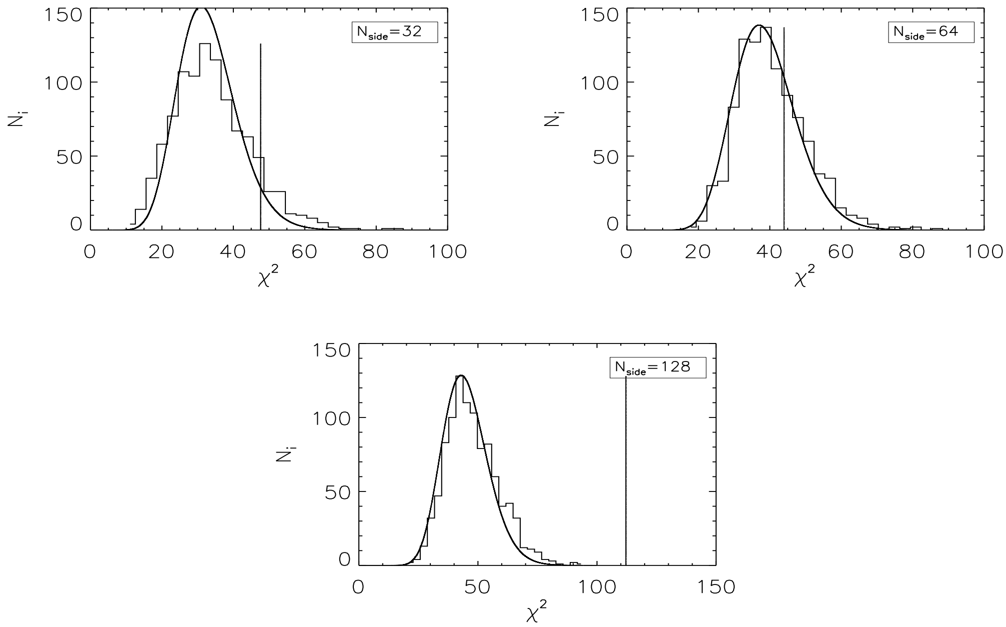

Figure 3.2 Distribution of the χ^2 values from the Minkowski Gaussianity analysis for the Archeops 143K03 noise map at $N_{side} = 32$, $N_{side} = 64$, and $N_{side} = 128$. Vertical lines show data, the histograms corresponds to sets of 10^3 noise simulations, and the solid lines are the χ^2 distribution with $3n_{th}$ degrees of freedom.

bolometers but the noise is not, after subtraction and assuming no systematic errors only the noise contributions remain. Defining d_{K03} as the data collected by 143K03 and d_{K04} the data collected by 143K04, the map that we analysed is

$$d = d_{K03} - d_{K04} \approx n_{K03} - n_{K04}. \tag{3.3.1}$$

We analysed the difference data maps given by equation 3.3.1 for three different resolutions: $N_{side} = 32$, $N_{side} = 64$, and $N_{side} = 128$. To construct simulations of the difference map, we used a set of 10^3 Gaussian signal simulations and 10^3 Gaussian noise simulations for each bolometer and each resolution. These simulations are used to compute the mean value $\langle v_i \rangle$ and the covariance matrix C_{ij} of the Minkowki functionals as described in section 1.4.2.

In figure 3.1 we present, from left to right, the Gaussianity analysis of the difference maps at the three resolution considered, $N_{side} = 32$, $N_{side} = 64$, and $N_{side} = 128$. The histograms correspond to the values of the χ^2 obtained for 10^3 simulations of difference maps. The vertical lines correspond to the value of χ^2 for the Archeops data. The solid lines are the theoretical $\chi^2_{3n_{th}}$ distribution normalised to the number of simulations and the size of the binned cell.

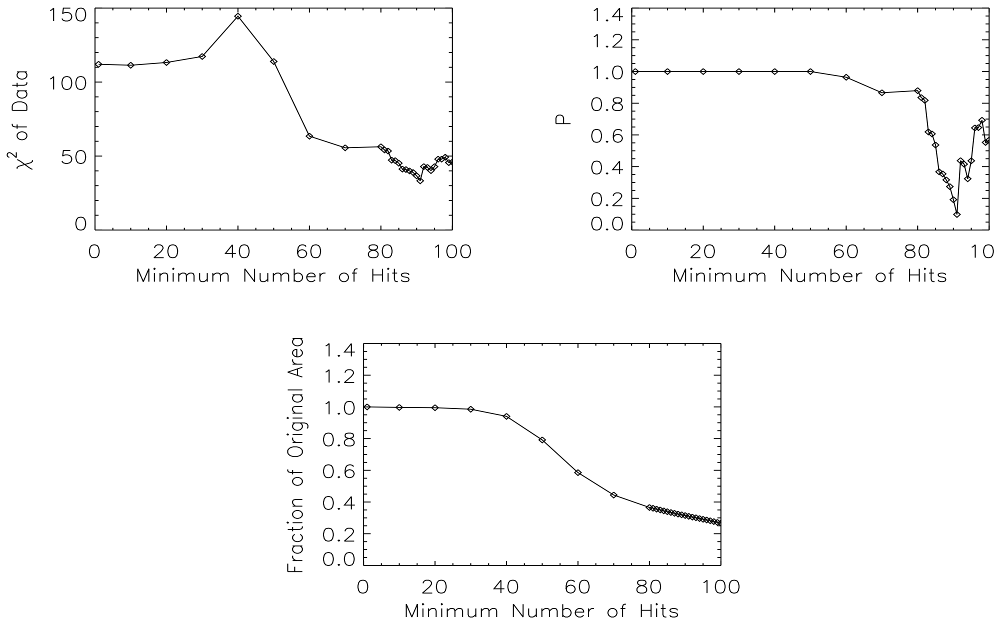

Figure 3.3 *From left to right*, χ^2 statistic of the 143K03 noise map, its cumulative probability, and the fraction of available area for different values of the minimum number of hits at $N_{side} = 128$. This map becomes compatible with Gaussianity when the minimum number of hits is approximately 90.

From this analysis we can see that the data given by equation 3.3.1 becomes non-Gaussian at high resolution. This is most probably due to highly noisy pixels in the difference maps corresponding to regions of the sky observed with little redundancy. A previous analysis [116] has shown that the Archeops instrumental noise in the map domain is Gaussian distributed for a given pixel when this pixel has been observed a significant amount of time, typically above a few hundred independent observations (hits) per pixel, although no precise estimate of the required number of hits per pixel was given.

This can be easily done using the statistical tools presented in this chapter. For this purpose we perform our analysis excluding highly noisy pixels defined as those pixels presenting a number of hits below a given threshold. We computed the χ^2 statistic of the data (equation 3.3.1), its cumulative probability, and the remaining area using different thresholds for the number of hits. By comparing to the Gaussian simulations we observe that for both $N_{side} = 64$ and $N_{side} = 128$, increasing the threshold of the number of hits implies that the data becomes compatible with Gaussianity. In particular, for $N_{side} = 64$ the data become compatible with Gaussianity when pixels with fewer than 250 hits are removed (leaving 46% of the original area) and for $N_{side} = 128$ the data start to become compatible with Gaussianity when pixels with fewer than 150 hits are removed (leaving 13% of the original area).

3.3.2 Single bolometer analysis

From the above analysis we have proved that highly noisy pixels are responsible for the non-Gaussianity of the Archeops noise at high resolution. In order to obtain proper limits for the f_{nl} parameter we need to exclude these pixels in our final analysis of the $143K03$ map.

To avoid any contamination from the $143K04$ noise map when characterizing the noise map for the 143K03 bolometer the latter was computed using the WMAP data as follows

$$n_{K03} = d_{K03} - WMAP_{K03} * f \tag{3.3.2}$$

where $WMAP_{K03}$ is the combined WMAP data computed as described in [44] and converted into an Archeops map as described in section 3.2.3. f is an intercalibration parameter between WMAP and Archeops, $f = 1/1.07$, as given by Tristram et al. [160]. In this case, as the noise on the WMAP data at the considered map resolutions is negligible compared to the Archeops noise, we expect no contamination.

We analysed the noise map given by equation 3.3.2 for three different pixel resolutions: $N_{side} = 32$, $N_{side} = 64$, and $N_{side} = 128$. For each resolution, we also analysed a set of 10^3 Archeops noise simulations n_{K03}. The results are presented in figure 3.2. The histograms correspond to the χ^2 of the Minkowski functionals of a set of 10^3 n_{K03} Gaussian simulations, vertical lines correspond to the data maps given by equation 3.3.2 and the solid lines are the $\chi^2_{3n_{th}}$ distributions. We can see that for low resolution ($N_{side} = 32$ and $N_{side} = 64$) the noise map is compatible with the Gaussian noise simulations. Therefore for these two resolutions we can use the full available area in the f_{nl} analysis.

In the case of $N_{side} = 128$ the noise map is not compatible with Gaussianity. As above, we reanalysed this noise map removing highly noisy pixels with a number of hits below a given threshold. This analsysis is presented in figure 3.3 where from left to right we plot the χ^2 statistic of the 143K03 noise map, its cumulative probability, and the fraction of available area for different values of

Table 3.1 χ^2 for the three Minkowski functionals for different resolutions and thresholds.

Resolution	Area (%)	χ^2_{data}	DOF	$\langle\chi^2\rangle$	$\sqrt{\langle(\chi^2-\langle\chi^2\rangle)^2\rangle}$	$P(\chi^2 \leq \chi^2_{data})$
32	100	43.62	33	33.55	10.05	0.868
64	100	44.39	39	40.55	10.33	0.679
128	32	50.59	45	46.29	10.79	0.688
32,64	100,100	85.14	72	73.88	14.29	0.804
32,64,128	100,100,32	134.05	117	120.30	18.40	0.791

the minimum number of hits. We can see that the Archeops noise for the 143K03 bolometer becomes clearly Gaussian when we remove pixels with a number of hits lower than 90. This means that the area where the noise is Gaussian is 32% of the original area at $N_{side} = 128$. In conclusion, the regions of the sky that we can use for the Gaussianity analysis are the whole initial area at $N_{side} = 32$ and $N_{side} = 64$ and 32% of the initial area at $N_{side} = 128$.

The 143K04 bolometer has a qualitatively similar behaviour for the noise analysis. That is, the noise map is compatible with Gaussianity at low resolution and is non-Gaussian at high resolution. Nevertheless as the noise for this bolometer has more systematic errors than the 143K03 bolometer, the thresholds for the number of hits where the maps become compatible with Gaussianity analysis are higher. This implies that the available area where the noise is Gaussian is smaller.

3.4 Results

In this section, we perform the Gaussianity analysis of the 143K03 Archeops bolometer data in order to constrain the non-linear coupling parameter, f_{nl}. For this, we first consider realistic non-Gaussian simulations as described in section 3.2.3. Then the results are compared to the ones obtained for non-Gaussian simulations for which only the Sachs-Wolfe contribution is included, as in [44].

3.4.1 Gaussianity analysis

For this analysis we apply the statistical methods described in section 1.4.2 to the Archeops 143K03 bolometer data. Figure 3.4 shows the Minkowski func-

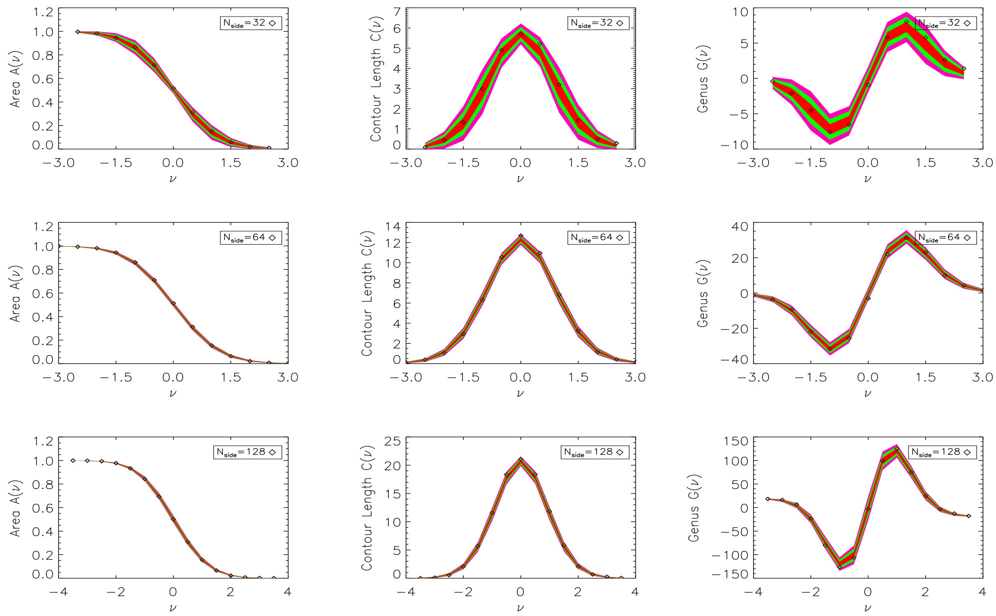

Figure 3.4 *From left to right,* and *from top to bottom,* the area, contour length, and genus of the data (asterisk *) as a function of threshold for the 143K03 maps with $N_{side} = 32$, $N_{side} = 64$, and $N_{side} = 128$. We also plot the acceptance intervals for the 68% (inner in red), the 95% (middle in green), and 99% (outer in magenta) significance levels given by 10000 Gaussian simulations of signal and noise.

tionals as a function of threshold for maps with $N_{side} = 32$, $N_{side} = 64$, and $N_{side} = 128$. In addition, we plot the acceptance intervals for the 68% (inner), the 95% (middle), and 99% (outer) significance levels obtained from 10000 noise and signal Gaussian simulations of the Archeops 143K03 data as described in section 3.2. For all the analysed cases the data are compatible with Gaussianity at least at the 99% significance level.

In figure 3.5 we present the results of the Gaussianity analysis of the Archeops 143K03 bolometer data at different resolutions using the χ^2 test described by equations 1.4.11 and 1.4.17. In particular, we analysed the data at $N_{side} = 32$ (11 thresholds, 3 functionals), $N_{side} = 64$ (13 thresholds, 3 functionals), $N_{side} = 128$ (15 thresholds, 3 functionals), the combination of the data at $N_{side} = 32$ and $N_{side} = 64$ (total of 24 thresholds, 3 functionals), and the combination of the data at $N_{side} = 32$, $N_{side} = 64$, and $N_{side} = 128$ (total of 39 thresholds, 3 functionals). To avoid confusion by the non-Gaussianity of the Archeops noise at high resolutions, the high noise pixels were excluded as discussed in the previous section. The histograms in the plot correspond to the analysis of 2000 Archeops

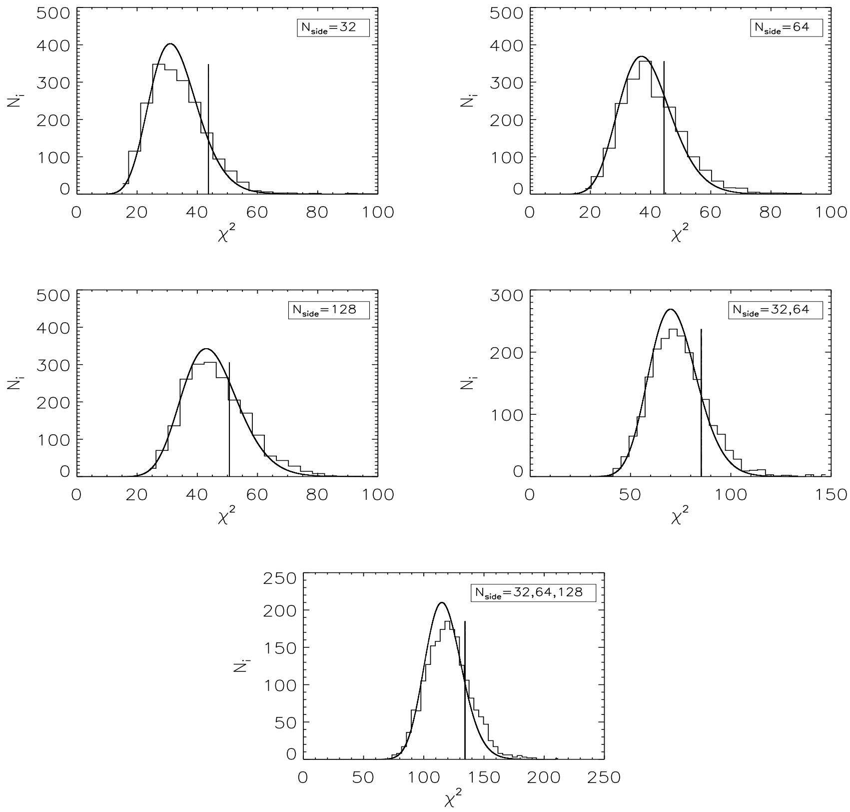

Figure 3.5 *From left to right*, and *from top to bottom*, the Gaussianity analysis of Archeops data maps at resolutions: $N_{side} = 32$, $N_{side} = 64$, $N_{side} = 128$, the combinations $N_{side} = 32, 64$, and the combinations $N_{side} = 32, 64, 128$. The histograms correspond to the χ^2 of 2000 Gaussian simulations, the vertical lines are the χ^2 of the data and the solid lines are the expected χ^2 distribution with $3N_{th}$ degrees of freedom.

signal plus noise Gaussian simulations at each resolution, the solid lines correspond to the expected $\chi^2_{3N_{th}}$ distribution, and the vertical lines correspond to χ^2 values of the data at each resolution. For all the resolutions and combination of resolutions, the Archeops data are consistent with Gaussianity as expected from the previous figure. In table 3.1 we present the χ^2 value of the data for the different cases that we have analysed, the total number of degrees of freedom, the mean and the dispersion of the χ^2 value of the Gaussian simulations, and the cumulative probability of the data computed from the distribution given by the simulations.

If we use all the available area at $N_{side} = 128$ we find that Archeops data are not compatible with Gaussianity. In particular, we have obtained $P(\chi^2 \leq \chi^2_{data}) = 0.995$ analysing the data at $N_{side} = 128$, and $P(\chi^2 \leq \chi^2_{data}) = 0.994$ analysing

Table 3.2 Best fit f_{nl} of Archeops data at different resolutions, mean, dispersion and some percentiles of the f_{nl} distributions obtained from 2000 Gaussian simulations.

Resolution	Area (%)	Best Fit f_{nl}	$\langle f_{nl} \rangle$	$\sigma(f_{nl})$	$X_{0.160}$	$X_{0.840}$	$X_{0.025}$	$X_{0.975}$
32	100	90	48	702	-670	785	-1370	1445
64	100	75	-29	645	-665	615	-1315	1270
128	32	-45	112	880	-810	1000	-1665	1805
32,64	100,100	70	-3	550	-525	535	-1130	1070
32,64,128	100,100,32	70	19	503	-470	520	-990	1005

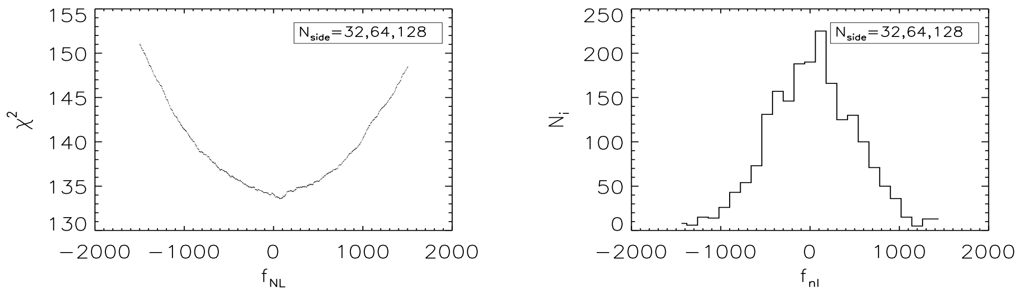

Figure 3.6 *From left to right,* $\chi^2(f_{nl})$ of Archeops data vs f_{nl} and the best fit value of f_{nl} for a set of 2000 Archeops Gaussian simulations ($s_{k03} + n_{k03}$) combining the maps at resolutions $N_{side} = 32, 64, 128$.

the data at $N_{side} = 32, 64, 128$. These non-Gaussian deviations can be clearly associated with the non-Gaussianity of the Archeops noise at high resolution due to highly noisy pixels.

3.4.2 Constraints on f_{nl} for realistic non-Gaussian simulations

The constraints in the f_{nl} parameter were obtained using 300 CMB non-Gaussian simulations such as the one described in section 3.2.3 and applying to the Archeops 143K03 bolometer data the χ^2 test in the case of non-Gaussian fluctuations defined by an f_{nl} parameter (equation 1.4.15). We computed an Archeops TOI for each realization and from it we computed the corresponding Mirage Archeops simulation for the 143K03 bolometer. We did this for the Gaussian and non-Gaussian part separately. So we have

$$d_{k03}(f_{nl}) = s_{g,k03} + f_{nl} * s_{ng,k03} + n_{g,k03} \tag{3.4.1}$$

where $s_{g,K03}$ is a Gaussian CMB simulation, $s_{ng,K03}$ is its corresponding non-Gaussian part, and $n_{g,K03}$ is a Gaussian instrumental noise simulation.

We computed the mean value of the Minkowki functionals, $\langle V \rangle_{f_{nl}}$, for $-1500 \leq f_{nl} \leq 1500$. We assumed that in this interval the covariance matrix associated with them was dominated by the Gaussian contribution: i.e. $C_{ij}(f_{nl}) \simeq C_{ij}(f_{nl} = 0)$. Therefore, it was computed from 10^4 Gaussian simulations of signal and noise ($s_{g,k03} + n_{g,k03}$) of the Archeops 143K03 bolometer. We obtained the $\chi^2(f_{nl})$ of Archeops data given by equations 1.4.15 and 1.4.18 for the same combination of resolutions as the ones described in the above Gaussianity analysis. In all cases we find the value of f_{nl} that minimizes $\chi^2(f_{nl})$. This is the best-fit value for the f_{nl} parameter. The significance of these values is estimated using 2000 Gaussian simulations. For each simulation we computed $\chi^2(f_{nl})$ vs f_{nl} and obtained its best fit f_{nl}. At the end we have a set of 2000 values of this parameter. As the simulations are Gaussian, these values are centred around $f_{nl} = 0$.

Table 3.2 lists the best-fit f_{nl} to the data for each case analysed. We also present the main properties of the distribution of the f_{nl} parameter as obtained from the simulations. The smaller dispersion corresponds to the case where we combine the data at the three resolutions N_{side} =32, 64, and 128 (only 32% of the available area). Therefore this case leads to the best constraints of f_{nl} for the Archeops data. In figure 3.6 we present the $\chi^2(f_{nl})$ vs f_{nl} of the Archeops data and the histogram of the best fit f_{nl} obtained from 2000 Gaussian simulations for this optimal case. From this we conclude that $f_{nl} = 70^{+590}_{-400}$ at 68% CL and $f_{nl} = 70^{+1075}_{-920}$ at 95% CL.

We may wonder if the constraints on the f_{nl} parameter could be improved by increasing the area at $N_{side} = 128$. We have shown that, if the noise were Gaussian, including the whole area available would have produced very similar constraints. The reason is that the excluded pixels were the noisiest ones and therefore increasing the area would not improve the results.

3.4.3 Comparing with the Sachs-Wolfe approximation

On large angular scales the main contribution to the CMB anisotropies is given by the Sachs Wolfe effect: $\Delta T/T = -\phi/3$ [93, 145], where ϕ is the primordial potential. Therefore, in this case, the temperature map can be approximated in

Table 3.3 Best fit of Sachs-Wolfe f_{nl} of Archeops data at different resolutions, mean, dispersion and some percentiles.

Resolution	Area (%)	Best Fit f_{nl}	$\langle f_{nl} \rangle$	$\sigma(f_{nl})$	$X_{0.160}$	$X_{0.840}$	$X_{0.025}$	$X_{0.975}$
32	100	-150	33	418	-375	425	-800	875
64	100	400	-3	252	-250	250	-500	500
128	32	-175	10	232	-225	250	-450	450
32,64	100,100	200	10	233	-225	250	-450	500
32,64,128	100,100,32	25	8	170	-175	175	-325	350

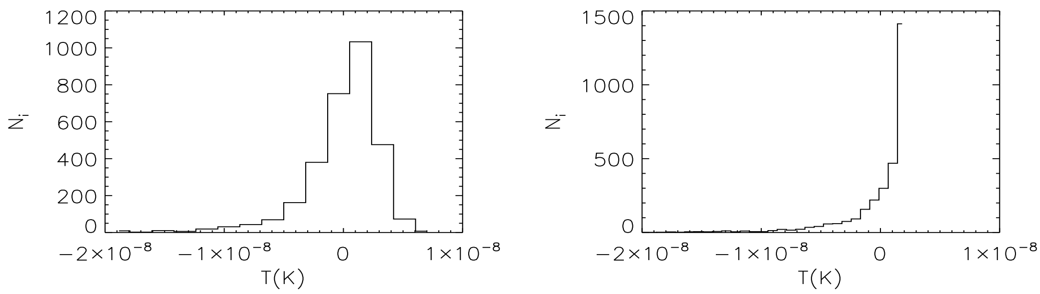

Figure 3.7 *From left to right*, the non-Gaussian part of a full sky CMB simulation at low resolution ($N_{side} = 16$) and the corresponding Sachs-Wolfe quadratic approximation.

terms of a linear and a non-linear contribution in the following simple way:

$$\frac{\Delta T}{T} = \frac{\Delta T_L}{T} - 3f_{nl}\left(\frac{\Delta T_L^2}{T^2} - \left\langle \frac{\Delta T_L}{T} \right\rangle^2\right) \tag{3.4.2}$$

where ΔT_L is Gaussian. We call this the Sachs-Wolfe approximation and to avoid confusion hereafter the f_{nl} parameter in this case is called f_{nl}^{SW}. This approximation has been used in several works [for example 28, 44, 90]. For this approximation the Archeops non-Gaussian simulations can be obtained as follows

$$d_{k03}(f_{nl}) = s_{g,k03} - \frac{3f_{nl}^{SW}}{T_0}(s_{g,k03}^2 - \langle s_{g,k03}^2 \rangle) + n_{g,k03}, \tag{3.4.3}$$

where $s_{g,k03}$ and $n_{g,k03}$ are Gaussian CMB and noise simulations respectively. As discussed above, this approximation is only valid for angular resolutions of a few degrees [93]. Nevertheless we performed the non-Gaussianity analysis of the Archeops data at all considered scales in order to contrain f_{nl}^{SW} and then tested the validity of this approximation as a function of the scale. In table 3.3 we present the results of this analysis. We can see that for all the considered resolutions, the f_{nl} constraints are better than for the case with the realistic simulations. This difference becomes more important as the resolution increases. The best constraints on f_{nl} in this case are $f_{nl}^{SW} = 25^{+200}_{-150}$ at 68% CL and $f_{nl}^{SW} = 25^{+375}_{-300}$ at 95% CL using the combination of the data at $N_{side} = 32, 64$, and 128 (only 32% of the available area).

In general the Sachs-Wolfe approximation overestimates the non-Gaussianity of the CMB fluctuations for a given f_{nl} value. This can be clearly seen in figure 3.7 where we present from left to right the histogram of the non-Gaussian part of a full sky CMB realistic simulation ΔT_{NG} and the corresponding quadratic approximation $-3f_{nl}/T_0(\Delta T_G^2 - \langle \Delta T_G \rangle^2)$ at resolution $N_{side} = 16$ i.e. a pixel size of 3.6 degrees. We can see that even at this scale the simulations are very different. The approximation is just the square of a Gaussian distribution centred to have zero mean whereas the exact simulation is more Gaussian-like. This explains why the constraints on the f_{nl} parameters are tighter for the Sachs-Wolfe approximation than for the exact case. Therefore, the results obtained with the Sachs-Wolfe approximation should be taken with caution, since the error bars are clearly underestimated.

CHAPTER 4

WMAP 5-year constraints on f_{nl} with wavelets

We present a Gaussianity analysis of the WMAP 5-year Cosmic Microwave Background (CMB) temperature anisotropy data maps. We use several third order estimators based on the spherical Mexican hat wavelet. We impose constraints on the local non-linear coupling parameter f_{nl} using well motivated non-Gaussian simulations. We analyse the WMAP maps at resolution of 6.9 arcmin for the Q, V, and W frequency bands. We use the $KQ75$ mask recommended by the WMAP team which masks out 28% of the sky. The wavelet coefficients are evaluated at 10 different scales from 6.9 to 150 arcmin. With these coefficients we compute the third order estimators which are used to perform a χ^2 analysis. The χ^2 statistic is used to test the Gaussianity of the WMAP data as well as to constrain the f_{nl} parameter. Our results indicate that the WMAP data are compatible with the Gaussian simulations, and the f_{nl} parameter is constrained to $-8 < f_{nl} < +111$ at 95% CL for the combined V+W map. This value has been corrected for the presence of undetected point sources, which add a positive contribution of $\Delta f_{nl} = 3 \pm 5$ in the V+W map. Our results are very similar to those obtained by Komatsu et al. [97] using the bispectrum.

4.1 Introduction

In this chapter we perform a wavelet-based analysis of the 5-year WMAP data in order to constrain the f_{nl} parameter. We use the high resolution WMAP data maps (6.9 arcmin) and realistic non-Gaussian simulations performed following the algorithms developed by Liguori et al. [109, 110].

The chapter is organised as follows. Section 4.2 presents the statistical method, the estimators that we use to test Gaussianity and constrain f_{nl}, as well as the data maps and simulations to be analysed. In Section 4.3 we summarise the results of this work. The conclusions are drawn in chapter 7.

4.2 Methodology

4.2.1 The estimators

In previous works, constraints on f_{nl} with wavelets have been obtained using only the skewness of the wavelet coefficients at different scales [e.g. 25, 132]. In this Chapter, other third order moments involving different scales are also considered[1]. In particular, we will consider 9 scales: $R_1 = 6.9'$, $R_2 = 10.3'$, $R_3 = 13.7'$, $R_4 = 25'$, $R_5 = 32'$, $R_6 = 50'$, $R_7 = 75'$, $R_8 = 100'$, and $R_9 = 150'$. In addition we will consider the unconvolved map, which will be represented hereafter as scale R_0. Larger scales are less sensitive to the local f_{nl} model. As it will be shown in the results section, the combination of these estimators is as efficient as the bispectrum. The estimators that we use in this analysis are based on third order combinations of the wavelet coefficient maps $w_i(R_j)$ evaluated in sets of three contiguous scales. For each scale R_j and the next two scales R_{j+1}

[1]Notice that inter-scale wavelet estimators have been previously used in the context of blind Gaussianity analyses, see e.g. Mukherjee et al. [131], Pando et al. [136] (for analyses involving two scales) and Cayón et al. [27] (involving three scales).

and R_{j+2} we can define

$$
\begin{aligned}
q_1(R_j) &= \frac{1}{N_j}\sum_{i=0}^{N_{pix}-1}\frac{w_{i,j}^3}{\sigma_j^3} \\
q_2(R_j,R_{j+1}) &= \frac{1}{N_{j,j+1}}\sum_{i=0}^{N_{pix}-1}\frac{w_{i,j}^2 w_{i,j+1}}{\sigma_j^2\sigma_{j+1}} \\
q_3(R_j,R_{j+1}) &= \frac{1}{N_{j,j+1}}\sum_{i=0}^{N_{pix}-1}\frac{w_{i,j} w_{i,j+1}^2}{\sigma_j\sigma_{j+1}^2} \\
q_4(R_j,R_{j+1},R_{j+2}) &= \frac{1}{N_{j,j+1,j+2}}\sum_{i=0}^{N_{pix}-1}\frac{w_{i,j} w_{i,j+1} w_{i,j+2}}{\sigma_j\sigma_{j+1}\sigma_{j+2}} \\
q_5(R_j,R_{j+2}) &= \frac{1}{N_{j,j+2}}\sum_{i=0}^{N_{pix}-1}\frac{w_{i,j}^2 w_{i,j+2}}{\sigma_j^2\sigma_{j+2}} \\
q_6(R_j,R_{j+2}) &= \frac{1}{N_{j,j+2}}\sum_{i=0}^{N_{pix}-1}\frac{w_{i,j} w_{i,j+2}^2}{\sigma_j\sigma_{j+2}^2}
\end{aligned}
\tag{4.2.1}
$$

where N_{j_1,j_2,j_3} is the number of available pixels after combining the scales R_{j_1}, R_{j_2}, and R_{j_3}, N_{pix} is the total number of pixels, $w_{i,j} = w_i(R_j)$, and σ_j is the dispersion of $w_{i,j}$. Each map $w_{i,j}$ is masked out with an appropriate mask at the scale R_j and its mean value outside the mask is removed. These estimators have a Gaussian-like distribution when are computed for a set of Gaussian simulations. Thus, we can use effectively a χ^2 statistics to test Gaussianity and to constrain f_{nl}. Considering all the estimators evaluated in all the scales we can construct a vector

$$\mathbf{v} = (q_1(R_0), q_2(R_0,R_1), q_3(R_0,R_1),, q_4(R_0,R_1,R_2), ...) \tag{4.2.2}$$

with a dimension of $n_v = n_{sc} + 2(n_{sc}-1) + 3(n_{sc}-2)$ for $n_{sc} \geq 2$, where n_{sc} is the number of considered scales. This vector is used to compute the χ^2 estimator

$$\chi^2 = \sum_{k,l=0}^{n_v-1}(v_k - \langle v_k\rangle)C_{kl}^{-1}(v_l - \langle v_l\rangle) \tag{4.2.3}$$

where $\langle\rangle$ is the expected value for the Gaussian case and C_{kl} is the covariance matrix $C_{kl} = \langle v_k v_l\rangle - \langle v_k\rangle\langle v_l\rangle$. The Gaussianity analysis consists on computing the χ^2 statistic for the data and compare it to the distribution of this quantity obtained from Gaussian simulations.

The second part of the analysis consists on setting constraints on the f_{nl} through a χ^2 test. In this case

$$\chi^2(f_{nl}) = \sum_{k,l=0}^{n_v-1} (v_k - \langle v_k \rangle_{f_{nl}}) C_{kl}^{-1}(f_{nl})(v_l - \langle v_l \rangle_{f_{nl}}) \tag{4.2.4}$$

where $\langle\rangle_{f_{nl}}$ is the expected value for a model with f_{nl} and $C_{kl} = \langle v_k v_l \rangle_{f_{nl}} - \langle v_k \rangle_{f_{nl}} \langle v_l \rangle_{f_{nl}}$. For low values of f_{nl} ($f_{nl} \leq 1500$) we can use the following approximation $C_{kl}(f_{nl}) \simeq C_{kl}(f_{nl} = 0) = C_{kl}$. The best-fit f_{nl} for the data is obtained by minimization of $\chi^2(f_{nl})$. Error bars for this parameter at different confidence levels are computed using Gaussian simulations.

4.2.2 Data and simulations

For our analysis, we use the 5-year WMAP foreground reduced data, which are available in the LAMBDA web site[2]. We combine the maps of different radiometers, using the inverse of the noise variance as an optimal weight, as described in Bennett et al. [15]. In particular we use five combined maps: Q+V+W, V+W, Q, V, and W. The Q+V+W map has the eight maps corresponding to the two radiometers of the Q band (41 GHz), two radiometers of the V band (61 GHz) and four radiometers of the W band (94 GHz). Similar combinations are constructed for the V+W, Q, V and W maps. The pixel resolution of these maps is 6.9 arcmin, corresponding to a HEALPix [65] N_{side} parameter of 512. The mask that we use is the $KQ75$ which discards 28% of the sky.

We should take into account the effect of the mask in the wavelet coefficient maps. Pixels near the border of the mask (the Galactic cut and other features) are affected by the zero value of the mask [165]. Therefore we need one extended mask for each scale that removes these affected pixels from the analysis. We use the method described in McEwen et al. [125] to construct our extended masks. We compute the wavelet coefficients at each scale of the $KQ75$ mask without the holes corresponding to the point sources, and consider only the pixels with low values (that is, the less affected pixels). Then we multiply by $KQ75$ to mask out the point sources. In particular, our threshold is 0.001, i.e., all the pixels which have a wavelet coefficient for the $KQ75$ mask larger than 0.001 in absolute value are masked out. In addition we also test the effect of the extension of the mask by applying a less restrictive threshold of 0.01. In figure

[2] http://lambda.gsfc.nasa.gov

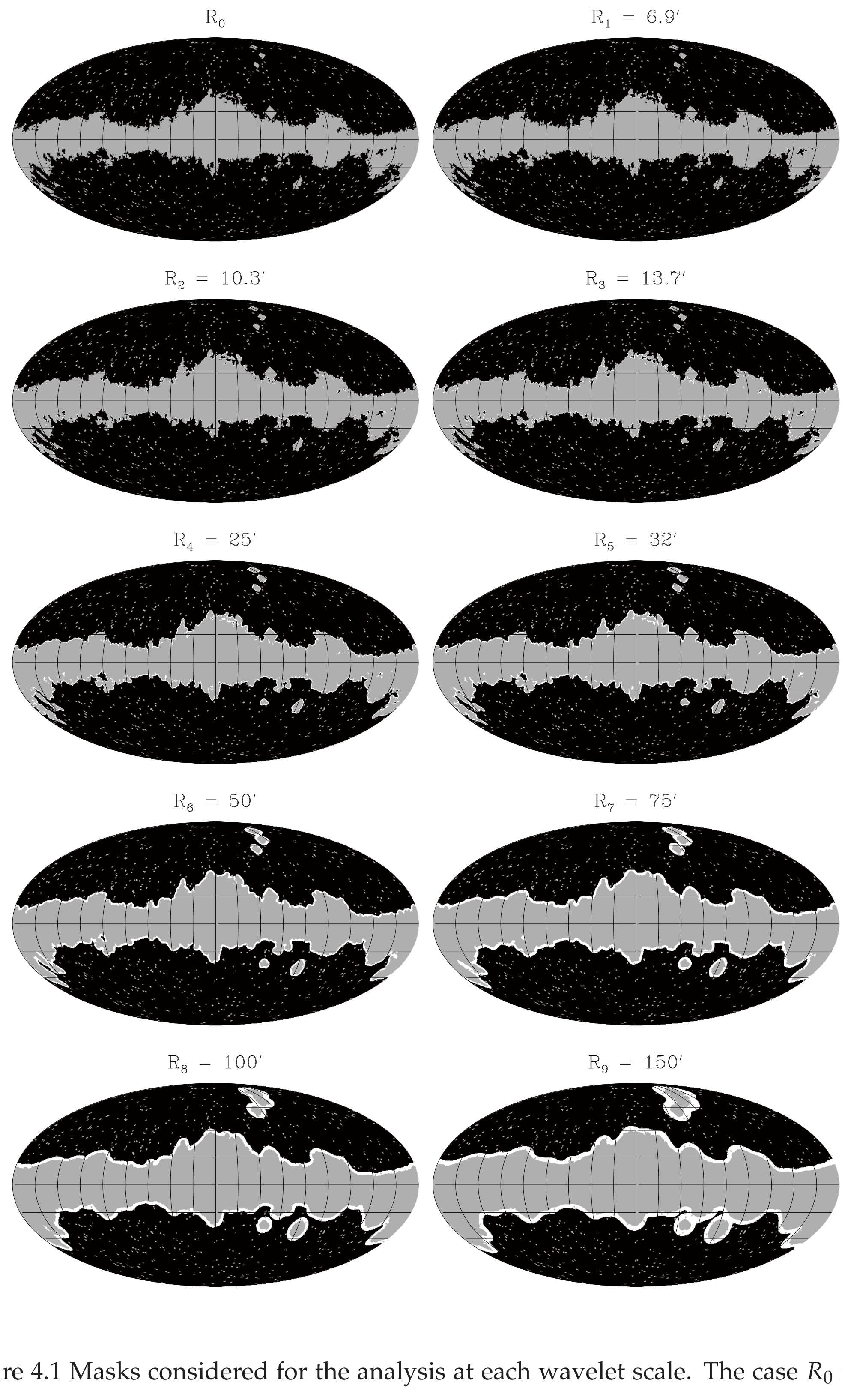

Figure 4.1 Masks considered for the analysis at each wavelet scale. The case R_0 is the $KQ75$ mask. The others correspond to the restrictive extended masks (black) and the less restrictive extended masks (white+black). The grid corresponds to a size of 20 degrees.

4.1 we present the masks that we use for the 10 considered scales.

We also need Gaussian and non-Gaussian simulations for this analysis. The Gaussian simulations are performed as follows. For a given power spectrum C_ℓ (we use the best fit power spectrum for WMAP provided by LAMBDA), we generate a set of Gaussian $a_{\ell m}$. From these multipoles we produce a map for each different radiometer by convolving with the corresponding beam transfer function. We also include the pixel properties by convolving with the pixel transfer function. We add a Gaussian noise realisation to each radiometer simulation and then we combine them in the same way as the data maps. Following the analysis of the WMAP team, we assume that the instrumental noise is well approximated by Gaussian white noise at each pixel. This noise is characterised by a dispersion that depends on the pixel position and the corresponding radiometer. Although the data also contain small residuals of $1/f$ noise [88, 89] their contribution here is expected to be negligible.

The non-Gaussian simulations are produced following a model which introduces a quadratic term in the primordial gravitational potential [66, 93, 146, 162]:

$$\Phi(\mathbf{x}) = \Phi_L(\mathbf{x}) + f_{nl}\{\Phi_L^2(\mathbf{x}) - \langle\Phi_L^2(\mathbf{x})\rangle\} \tag{4.2.5}$$

where $\Phi_L(\mathbf{x})$ is a linear random field which is Gaussian distributed and has zero mean. This kind of non-Gaussianity is generated in various non-standard inflationary scenarios [see, e.g. 13]. The simulations with f_{nl} are generated following the algorithms described in Liguori et al. [109, 110]. In particular we have a set of 300 Gaussian simulations in the $a_{\ell m}$ space, $a_{\ell m}^{(G)}$ and their corresponding non-Gaussian part $a_{\ell m}^{(NG)}$. A simulation with a given value of f_{nl} is constructed as

$$a_{\ell m} = a_{\ell m}^{(G)} + f_{nl} a_{\ell m}^{(NG)}. \tag{4.2.6}$$

To produce each non-Gaussian WMAP simulation with f_{nl} we transform the multipoles defined in equation 4.2.6 into each differencing assembly map using the corresponding beam and pixel transfer functions and we add a Gaussian noise realisation. Then, we combine these maps to form the Q+V+W, V+W, Q, V and W combined maps.

4.3 Results

In this section we present the Gaussianity analysis of the WMAP data using the Q+V+W, V+W, Q, V, and W combined data maps. First we consider the estimators defined in equations 4.2.1 and the χ^2 statistic given in equation 4.2.3 and compare the values obtained for the WMAP data with the distribution constructed with Gaussian simulations. Second we constrain the local non-linear coupling parameter f_{nl} using realistic non-Gaussian simulations. Finally we estimate the contribution of the undetected point sources to the best fit value of f_{nl}.

4.3.1 Analysis of WMAP data

We estimate the wavelet coefficient maps at the 10 considered scales defined in section 4.2.1. In particular, for $n_{sc} = 10$ we have 52 estimators as the ones defined in equation 4.2.1. In figure 4.2 we present these statistics for the WMAP data compared with the values obtained for 1000 Gaussian simulations. We analyse the Q+V+W, V+W, Q, V, and W combined maps using the restrictive extended masks, and we also analyse the V+W map with the less restrictive extended masks (marked in the tables and figures with $(V+W)^*$). The q_1 estimator (defined in equation 4.2.1, corresponding to the skewness) has a similar shape than the one obtained for the 1-year and 3-year data maps [40, 132, 165]. In all the cases the skewness obtained for the data is compatible with the skewness of Gaussian simulations. We can see in figure 4.2 that the values of the estimators with $k \geq 36$ are systematically below the mean. However, for a correct interpretation of this trend it is important to take into account that those estimators are strongly correlated at large scales. In particular, considering the normalised correlation matrix in the V+W case, $C_{ij}/(\sigma_i\sigma_j)$, we have that its elements are $C_{ij}/(\sigma_i\sigma_j) \sim 0.7$ on average for vector indices greater or equal than 36, whereas $C_{ij}/(\sigma_i\sigma_j) \sim 0.4$ for vector indices lower than 36.

We have also performed a χ^2 analysis in order to check if the data are compatible with Gaussian simulations. This is plotted in figure 4.3. We estimate the mean and the covariance used in equation 4.2.3 with another set of 1000 Gaussian simulations. We can see that for all the cases, the data are compatible with the Gaussian simulations. The statistical properties of the histograms are presented in table 4.1, where we give the χ^2 value obtained for the data, the de-

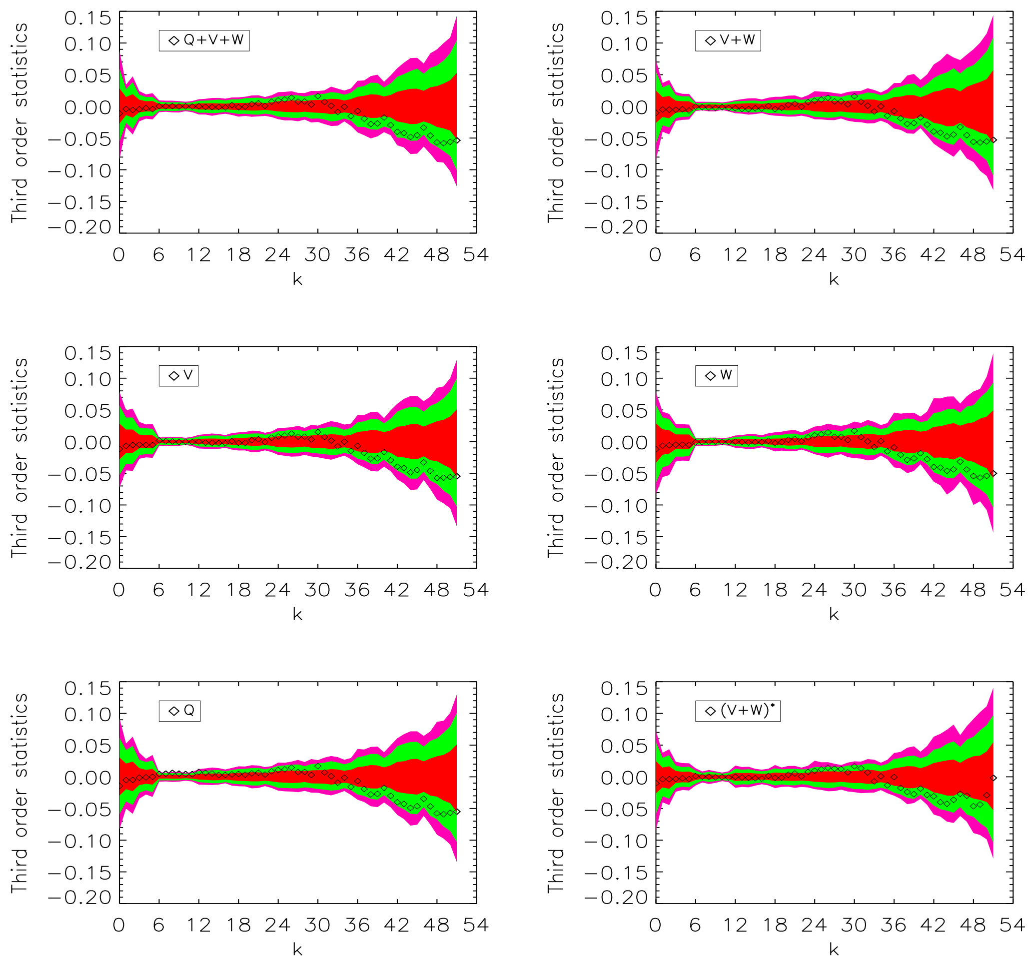

Figure 4.2 The 52 statistics v_k, given in equation 4.2.2, evaluated at 10 different scales for the WMAP combined maps. From left to right and top to bottom, we present the values corresponding to the Q+V+W, V+W, V+W, Q, V, W maps using the restrictive extended masks, and the V+W map using the less restrictive extended masks. The diamonds correspond to the data. We also plot the acceptance intervals for the 68% (inner in red), 95% (middle in green), and 99% (outer in magenta) significance levels given by 1000 Gaussian simulations of signal and noise.

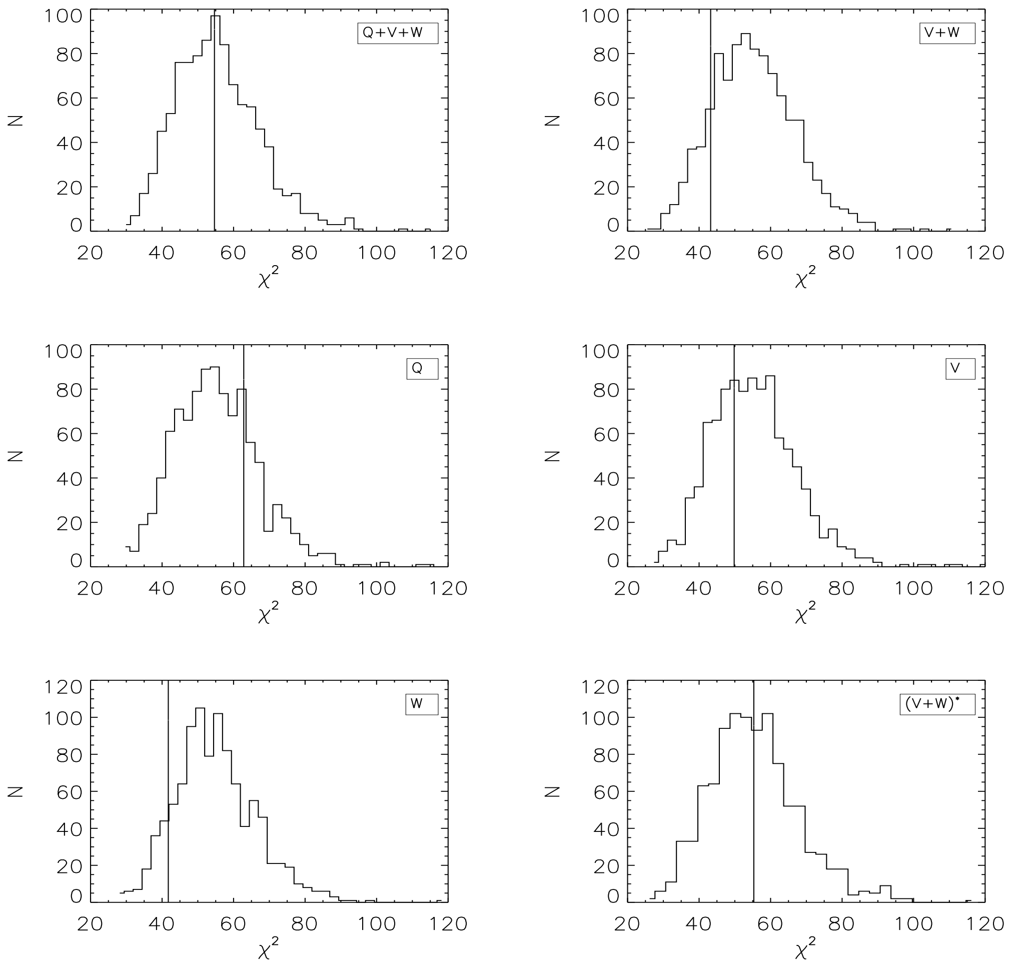

Figure 4.3 The distribution of the χ^2 statistics obtained from Gaussian simulations of the Q+V+W, V+W, Q, V, W maps using the restrictive extended masks, and the V+W map using the less restrictive extended masks. The vertical lines correspond to the values obtained from the data.

grees of freedom of the χ^2 statistic (DOF), the mean and the dispersion obtained for Gaussian simulations and the cumulative probability for the data.

Finally we impose constraints on the f_{nl} parameter using the considered maps. We calculate the expected values of all the estimators for different f_{nl} cases[3] (see left panel of figure 4.4 for the combined V+W map). Then, we perform a χ^2 analysis using equation 4.2.4 in order to find the best fit value for f_{nl} for each data map. We also analyse Gaussian simulations in order to obtain the frequentist error bars. In the central and right panels of figure 4.4 we present a plot of $\chi^2(f_{nl})$ versus f_{nl} for the combined V+W data and a histogram of the best fit f_{nl} for 1000 Gaussian simulations of the combined V+W map. Table 4.2 lists the f_{nl} values which best fits the five considered maps, and the main properties of the distributions of best-fit f_{nl} obtained from Gaussian simulations. From this table we have at 95% CL that $-8 < f_{nl} < 118$ for the combined V+W map, $-42 < f_{nl} < +93$ for Q+V+W, $-63 < f_{nl} < +102$ for Q, $-46 < f_{nl} < +109$ for V, and $-38 < f_{nl} < +114$ for W (using the restrictive extended masks defined in section 4.2.2). These values are compatible with the ones obtained by Komatsu et al. [97] using the bispectrum. Notice that f_{nl} increases as we go from Q to W maps. The f_{nl} value obtained for the V+W map is the same as the one that Komatsu et al. [97] obtains for this map using $\ell_{max} = 700$ and the $KQ75$ mask. The Q+V+W map has a smaller f_{nl} value. The best-fit f_{nl} increases with frequency for the Q, V, and W maps, and the $\sigma(f_{nl})$ of the Q map is larger than the one of the V and W maps. This also agrees with Komatsu et al. [97].

The less restrictive extended masks give tighter results for the constraints on f_{nl} compared with the restrictive ones. In particular, from table 4.2, we have that $-5 < f_{nl} < +114$ at 95% CL. In this case the dispersion of f_{nl} is smaller since the available area is larger for all the scales. The additional pixels are not significantly affected by the mask for this analysis and the wavelet is still efficient. These constraints are very similar to those obtained with the bispectrum [97], which are $-5 < f_{nl} < +115$ at 95% CL.

Notice however that other works, e.g. Yadav & Wandelt [173], have found evi-

[3] We use 300 simulations to calculate the mean values of the estimators for different f_{nl} cases and 1000 Gaussian simulations to calculate the covariance matrix. We analysed the convergence of the mean values by computing the best-fit f_{nl} value of the data using two independent sets of 150 simulations. The difference in the obtained value is lower than 1 and therefore even with $\sim$100 simulations the convergence is achieved. Analogously, for the covariance matrix we have checked that convergence is achieved with $\sim$1000 Gaussian simulations.

Table 4.1 χ^2 constructed from the 52 statistics for Q+V+W, V+W, Q, V, and W data maps using equation 4.2.3. We also present the mean and the dispersion of the χ^2 corresponding to 1000 Gaussian simulations, and the cumulative probability for the χ^2 of the data.

Map	χ^2_{data}	DOF	$\langle\chi^2\rangle$	σ	$P(\chi^2 \leq \chi^2_{data})$
Q+V+W	54.65	52	55.49	11.78	0.63
V+W	43.23	52	55.22	11.73	0.20
Q	62.84	52	55.31	12.08	0.86
V	49.81	52	55.24	11.96	0.44
W	41.74	52	54.92	11.34	0.16
(V+W)*	55.31	52	55.47	12.47	0.65

* The V+W map is analysed using the less restrictive extended masks.

dences of non-zero value for f_{nl} at 2.8σ CL using the KSW bispectrum. We do not find deviations with respect to the zero value using the 5-year data at 95 % CL and the same result is presented in Komatsu et al. [97]. We may wonder if that deviation is introduced by the 3-year WMAP mask (Kp0), uncertainties in the characterisation of the beams, or some systematics present in the 3-year data. To check this possibility we analysed the V+W 3-year WMAP data (updated after the 5-year release) using our estimators, the Kp0 mask and its corresponding extended masks. The results are $-17 < f_{nl} < +108$ at 95% CL, which are compatible with the 5-year results. Therefore our method is not able to detect the deviations reported in Yadav & Wandelt [173] using the 3-year data. This may be explained by the fact that the wavelet method probes different combinations of scales than the bispectrum and also responds differently to possible systematics present in the data.

We have also tested other third order estimators that involve the derivatives (in particular the squared modulus of the gradient and the Laplacian) of the wavelet coefficient maps. These estimators are less sensitive to the f_{nl} parameter and its error bars are significantly wider than the ones obtained with the estimators of equation 4.2.1.

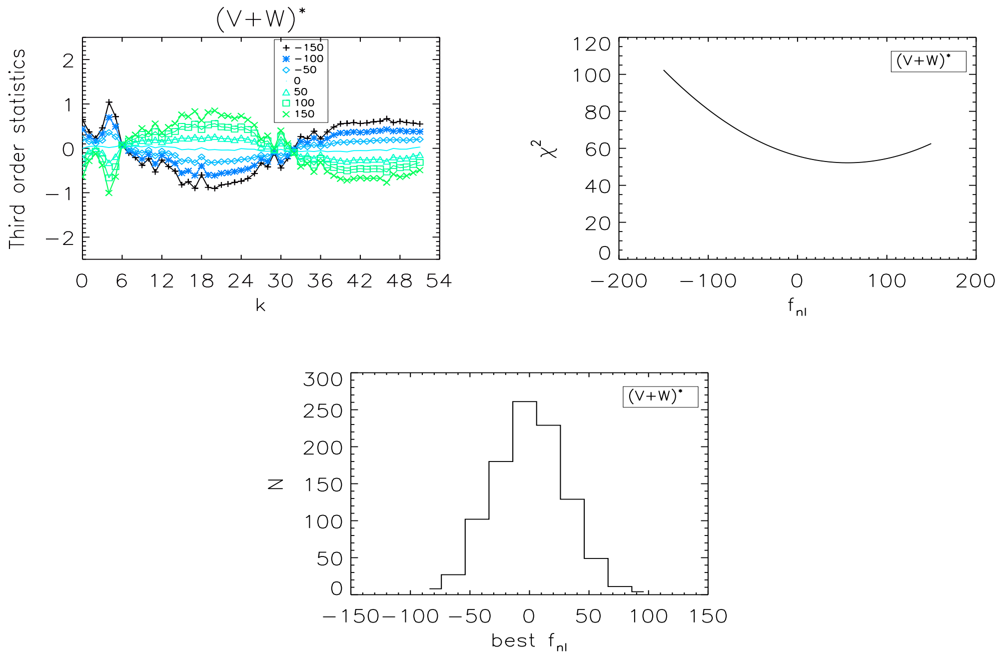

Figure 4.4 *From left to right and top to bottom*, the normalised mean values of the estimators for 300 simulations of the V+W map with different f_{nl} contributions, the $\chi^2(f_{nl})$ statistics for the WMAP combined V+W data map, and the histogram of the best fit f_{nl} values for a set of 1000 Gaussian simulations of the V+W map. We have used the less restrictive extended masks. Similar results are obtained with the restrictive extended masks.

Table 4.2 Best fit f_{nl} values obtained from Q+V+W, V+W, Q, V and W combined maps. We also present the mean, dispersion and some percentiles of the distribution of the best fit f_{nl} values obtained from Gaussian simulations.

Map	best f_{nl}	$\langle f_{nl} \rangle$	$\sigma(f_{nl})$	$X_{0.160}$	$X_{0.840}$	$X_{0.025}$	$X_{0.975}$
Q+V+W	26.	-2.	34.	-34.	30.	-68.	67.
V+W	58.	-1.	33.	-35.	34.	-66.	60.
Q	16.	-1.	42.	-43.	41.	-79.	86.
V	30.	0.	39.	-39.	38.	-76.	79.
W	40.	-4.	39.	-44.	35.	-78.	74.
(V+W)*	56.	0.	30.	-31.	30.	-61.	58.

* The V+W map is analysed using the less restrictive extended masks.

4.3.2 Contribution of undetected point sources

It has been shown that the Mexican hat wavelet is very useful in detecting point sources [26, 163] since their contribution is enhanced in the wavelet coefficient maps at certain scales. Therefore it is important to study the contribution of the undetected point sources on the f_{nl} estimation. The skewness and kurtosis of wavelet coefficient maps due to point sources have been studied in Argüeso et al. [7]. We estimate the contribution of the point sources to our estimators by performing Monte Carlo simulations. We use a straightforward model to simulate the radio sources following the one described in Komatsu et al. [97]. In this model it is assumed that all the sources have the same intensity flux, (F_{src} =0.5 Jy), and that they are randomly distributed in the sky following a Poisson distribution. The source contribution to the temperature at any pixel is given by

$$T_{src}(\mathbf{n}) = \frac{\sinh(x/2)^2}{x^4} \frac{1}{24.8\ MJy/K} \frac{F_{src}}{\Omega_{pix}} \epsilon \tag{4.3.1}$$

where $x = \nu/(56.8\ GHz)$, $\Omega_{pix} = 4\pi/N_{pix}$, ϵ is a Poisson random variable of mean $\langle\epsilon\rangle = \Omega_{pix} n_{src}$ and n_{src} is the density of sources. The power spectrum for this type of source distribution can be easily calculated [159].

$$C_l^{ps} = n_{src} T_0^2 \frac{\sinh^4(x/2)}{x^8} \left(\frac{F_{src}}{67.55\ MJy} \right)^2 \tag{4.3.2}$$

Using $n_{src} = 85\ sr^{-1}$ and a pixel resolution of $N_{side} = 512$ we have a power spectrum of $C_l^{ps} = 8.68 \times 10^{-3}\ \mu K^2 sr$ for the Q band. This model roughly reproduces the measured values of the power spectrum and the bispectrum [97, 134].

For this analysis we have performed 1000 point source simulations for the V+W map. We add these point source simulations to the V+W simulations of CMB with noise. For each one we estimate its best fit f_{nl} and compare it with the values obtained for the same simulation but without point sources. The difference gives us an estimate of the contamination due to the point sources. They add a contribution of $\Delta f_{nl} = 11 \pm 4$ to the CMB considering the restrictive extended masks. For the less restrictive extended masks the point source contribution is $\Delta f_{nl} = 3 \pm 4$. The difference with the previous result is explained because the zero values of the $KQ75$ mask affect the efficiency of the wavelet to detect point sources. This can be seen in the left panel of figure 4.5 where we plot the mean values for the third order estimators for the V+W simulations including point sources for both kinds of extended masks. The mean value of several estimators, specially the skewness for small scales, is lower for the less restrictive extended masks. This reduces the Δf_{nl} value. Considering the contribution of the point sources, our estimate of f_{nl} for this case is $+22 < f_{nl} < +83$ at 68% CL and $-8 < f_{nl} < +111$ at 95% CL. For comparison, the bias introduced by point sources for the bispectrum is $\Delta f_{nl} = 5 \pm 2$ [97].

We also estimate the contribution of undetected point sources using the more realistic source number counts dN/dS, derived from the work of de Zotti et al. [176]. The dependence of dN/dS with the frequency is very small in the range between 61 GHz and 94 GHz. Thus, for simplicity, we assume the same dN/dS for both V and W maps, evaluated at a frequency of 71 GHz. We select a range of intensities between $S_{min} = 1$ mJy and $S_{max} = 1$ Jy. Then we generate point source simulations following the distribution dN/dS derived from de Zotti et al. [176]. The simulations are transformed from intensity flux to temperature as in the previous case (following equation 4.3.1). For this analysis we have also performed 1000 point source simulations for the $V + W$ map and have added them to Gaussian CMB plus noise simulations. We analyse the resultant simulations as in the previous case to obtain the contribution to f_{nl} due to the point sources. They add a contribution of $\Delta f_{nl} = 3 \pm 5$ to the CMB considering the less restrictive extended masks and $\Delta f_{nl} = 17 \pm 5$ considering the restrictive extended masks. As in the previous case, the differences in Δf_{nl} using the restrictive and less restrictive extended masks are explained because the zero values of the $KQ75$ mask affect the efficiency of the wavelet. This is plotted in the right panel of figure 4.5.

Therefore, considering the realistic point source model and the less restrictive masks our estimate of f_{nl} remains unchanged ($-8 < f_{nl} < +111$ at 95% CL).

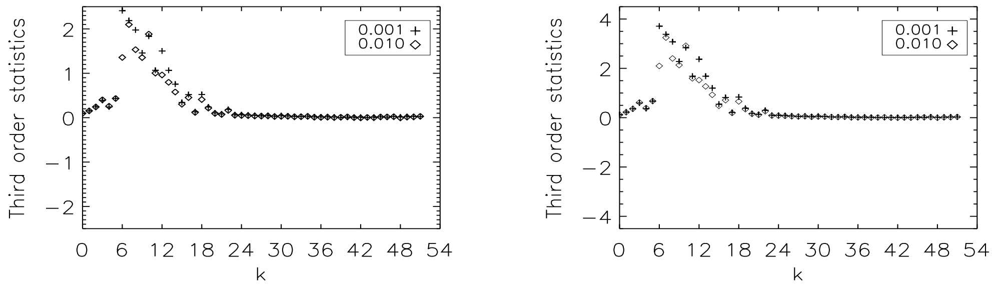

Figure 4.5 Normalised mean value of the third order estimators for 1000 Gaussian simulations plus point source simulations of the V+W combined map using the restrictive mask (threshold of 0.001) and the less restrictive mask (threshold of 0.010). In the left panel we use the model with point sources of constant flux, F_{src}=0.5 Jy, and in the right panel we use the model with a dN/dS derived from de Zotti et al. [176].

CHAPTER 5

Improved constraints on f_{nl} with the WMAP 5-yr data

We present new constraints on the non-linear coupling parameter f_{nl} with the Wilkinson Microwave Anisotropy Probe (WMAP) data. We use a method based on the spherical Mexican hat wavelet (SMHW) which provides improved constraints on the f_{nl} parameter. This chapter is a continuation of a previous work by Curto et al. where several third order statistics based on the SMHW were considered. In this chapter, we use all the possible third order statistics computed from the wavelet coefficient maps evaluated at 12 angular scales. The scales are logarithmically distributed from 6.9 arcmin to 500 arcmin. Our analysis indicates that f_{nl} is constrained to $-18 < f_{nl} < +80$ at 95% confidence level (CL) for the combined V+W WMAP map. This value has been corrected by the presence of undetected point sources, which adds a positive contribution of $\Delta f_{nl} = 6 \pm 5$. Our result excludes at $\sim$99% CL the best-fitting value f_{nl} =87 reported by Yadav & Wandelt. We have also constrained f_{nl} for the Q, V and W frequency bands separately, finding compatibility with zero at 95 % CL for the Q and V bands but not for the W band. We have performed some further tests to understand the cause of this deviation which indicate that systematics associated to the W radiometers could be responsible for this result. Finally we have performed a Galactic North-South analysis for f_{nl}. We have not found any asymmetry, i.e. the best-fitting f_{nl} for the northern pixels is compatible with the best-fitting f_{nl} for the southern pixels.

5.1 Introduction

This chapter is a continuation of the wavelet-based analysis by Curto et al. [46] of the WMAP[1] data. We use high resolution WMAP data maps, and compute the wavelet coefficients for 12 angular scales logarithmically spaced from 6.9 arcmin to 500 arcmin. With these wavelet coefficients we compute all the possible third order moments involving these scales.

The chapter is organised as follows. Section 5.2 presents the estimators used to test Gaussianity and to constrain f_{nl}, the data maps and the simulations. Section 5.3 summarises the main results of this chapter and the conclusions are in chapter 7.

5.2 Methodology

This analysis is based on the spherical Mexican hat wavelet (SMHW) as defined in Martínez-González et al. [120]. For references about the use of the SMHW to test Gaussianity in the CMB see for example the review by Martínez-González [123]. We compute the wavelet coefficient maps at several scales R_i logarithmically separated (R_{i+1}/R_i constant). The considered scales are: $R_1 = 6.9'$, $R_2 = 10.6'$, $R_3 = 16.3'$, $R_4 = 24.9'$, $R_5 = 38.3'$, $R_6 = 58.7'$, $R_7 = 90.1'$, $R_8 = 138.3'$, $R_9 = 212.3'$, $R_{10} = 325.8'$, $R_{11} = 500'$. We also include the unconvolved map, which will be represented by the scale R_0 as in Curto et al. [46]. For each possible combination of three scales R_i, R_j, and R_k (where the indices i, j, and k can be repeated) we define a third order statistic

$$q_{ijk} = \frac{1}{N_{i,j,k}} \sum_{p=0}^{N_{pix}-1} \frac{w_{p,i} w_{p,j} w_{p,k}}{\sigma_i \sigma_j \sigma_k} \tag{5.2.1}$$

where N_{pix} is the total number of pixels of the map, $N_{i,j,k}$ is the number of pixels available after combining the extended masks corresponding to the three scales R_i, R_j and R_k, $w_{p,i} = w_p(R_i)$ is the wavelet coefficient in the pixel p evaluated at the scale R_i, and σ_i is the dispersion of $w_{p,i}$. Each map $w_{p,i}$ is masked out with the corresponding extended mask at the scale R_i as in Curto et al. [46]. For a set of n scales we have $n_{stat} = (n + 3 - 1)!/[3!(n - 1)!]$ third order statistics such as the one defined in equation (5.2.1). We have tested with simulations

[1] http://map.gsfc.nasa.gov/

that these statistics have a Gaussian-like distribution. We can construct a vector $\mathbf{q}$ of dimension n_{stat}

$$\mathbf{q} = [q_{0,0,0}; q_{0,0,1}; ...; q_{0,0,11}; q_{0,1,1}; ...; q_{11,11,11}]. \tag{5.2.2}$$

With this vector we can perform two different analyses using a χ^2 statistic: one to test Gaussianity and a second one to constrain f_{nl} [equations (7) and (8) of 46].

We use the 5-yr WMAP foreground reduced data, available in the Legacy Archive for Microwave Background Data Analysis (LAMBDA) web site[2]. We combine the maps of different radiometers using the inverse of the noise variance as an optimal weight [15]. In particular we analyse the V+W, Q, V and W combined maps at a resolution of 6.9 arcmin, corresponding to a HEALPix [65] $N_{side} = 512$. We use the $KQ75$ mask and also a set of extended masks for the wavelet coefficient maps. We use the same masks as the ones described in Curto et al. [46] for a threshold of 0.01. This corresponds to an available fraction of the sky from 71.2% for the R_1 scale to 31.4% for the R_{11} scale. Notice that larger scales have the restriction of a lower available area, which means a lower sensitivity to f_{nl}.

Finally we analyse the data and compare them with Gaussian and non-Gaussian simulations. The Gaussian simulations are performed using the best fit power spectrum C_ℓ for WMAP provided by LAMBDA and the instrumental white noise of each WMAP radiometer. The non-Gaussian simulations with the f_{nl} contribution are computed following the algorithms described in Liguori et al. [109, 110] and transformed into WMAP maps with the instrumental noise included. We also estimate the unresolved point source contribution to f_{nl} for the V+W case by analysing point source simulations. These simulations have been generated as in Curto et al. [46] following the source number counts dN/dS given by de Zotti et al. [176].

5.3 Results

In this section we present the Gaussianity analysis of the WMAP data for the combined V+W, Q, V, and W data maps. We also constrain f_{nl} for these maps

[2] http://lambda.gsfc.nasa.gov

Table 5.1 χ^2 constructed from the 364 statistics for V+W, Q, V, and W data maps. We also present the mean and the dispersion of the χ^2 corresponding to 1,000 Gaussian simulations, and the cumulative probability for the χ^2 of the data.

Map	χ^2_{data}	DOF	$\langle\chi^2\rangle$	σ	$P(\chi^2 \leq \chi^2_{data})$
V+W	349	364	379	49.2	0.29
Q	384	364	378	48.7	0.63
V	348	364	377	47.8	0.27
W	354	364	376	47.9	0.35

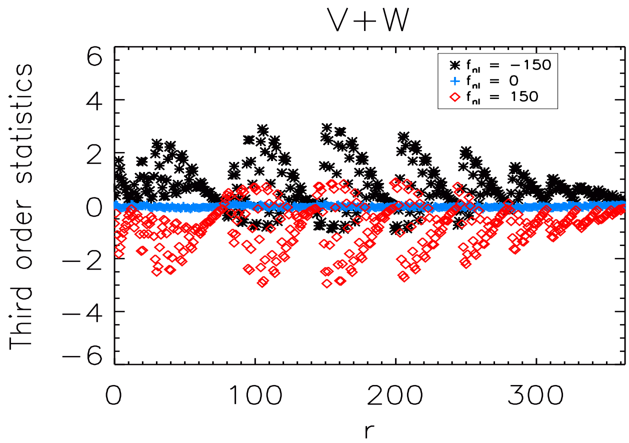

Figure 5.1 The expected values of the normalised third order statistics q_r for V+W simulations with different values of f_{nl}, where $r \equiv \{i, j, k\}$ is ordered following equation 5.2.2.

through a χ^2 test. We estimate the contribution of point sources to the V+W map. Finally we constrain f_{nl} for northern and southern pixels separately.

5.3.1 Analysis of WMAP data

We evaluate the wavelet coefficients at the 12 considered scales. With these coefficients we compute the third order estimators defined in equation 5.2.1. For 12 scales, we have 364 possible third order statistics. We compute these statistics for the data maps and for Gaussian simulations. The covariance matrix used in the χ^2 statistics is constructed from 10,000 Gaussian simulations. For the considered cases, V+W, Q, V and W, we have that the data are inside the 2σ error bars, i.e., the data are compatible with Gaussian simulations. We compute

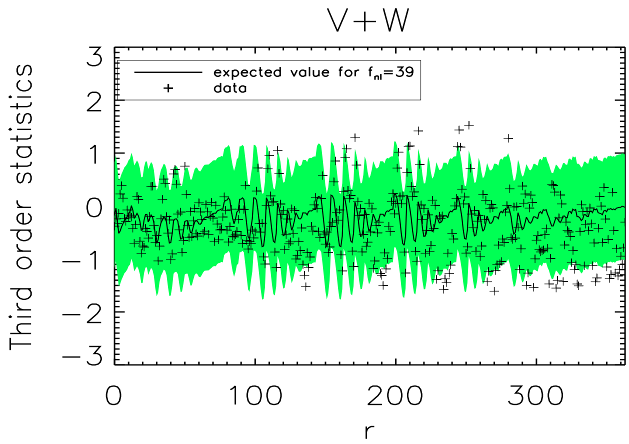

Figure 5.2 The normalised third order statistics q_r for the combined V+W data map. The solid line corresponds to the expected values for the best-fitting f_{nl} model ($f_{nl} = 39$). We also plot the 1σ error bars in green.

Table 5.2 Best-fitting f_{nl} values obtained from V+W, Q, V and W combined maps. We also present the mean, dispersion and some percentiles of the distribution of the best fit f_{nl} values obtained from Gaussian simulations.

Map	best f_{nl}	$\langle f_{nl} \rangle$	$\sigma(f_{nl})$	$X_{0.160}$	$X_{0.840}$	$X_{0.025}$	$X_{0.975}$
V+W	39	-1	25	-26	24	-51	47
Q	11	0	33	-31	34	-63	66
V	23	0	30	-28	30	-55	59
W	65	-4	30	-33	26	-59	58

a χ^2 statistic by comparing the data with the expected value of Gaussian simulations following Curto et al. [46]. We as well compute the χ^2 of an additional set of 1,000 Gaussian simulations. The χ^2 statistic of the data is compatible with the χ^2 of the Gaussian simulations. This is presented in table 5.1.

We impose constraints on f_{nl} through a χ^2 test. We calculate the expected values of the estimators for different f_{nl} cases using a set of 300 non-Gaussian simulations. In figure 5.1 we plot the expected values of the 364 statistics q_r for several f_{nl} cases for the V+W map. In figure 5.2 we plot the values of these statistics for the data map and compare them with the expected values for the best-fitting f_{nl} model. Then we perform a χ^2 analysis to find the best-fitting value of f_{nl} for each map. We also analyse Gaussian simulations in order to obtain the frequentist error bars. Table 5.2 lists the best-fitting f_{nl} values for the V+W, Q, V and W combined maps and the main properties of the histograms of the best-fitting f_{nl} obtained from Gaussian simulations. In the left panel of figure 5.3 we plot the $\chi^2(f_{nl})$ versus f_{nl} for the V+W map, and in the right panel of figure 5.3 we plot the histogram of the best-fitting f_{nl} of 1,000 Gaussian simulations. We have $-12 < f_{nl} < +86$ for V+W, $-52 < f_{nl} < +77$ for Q, $-32 < f_{nl} < +82$ for V and $+6 < f_{nl} < +123$ for W (all at 95% CL). Note that f_{nl} increases as the frequency grows from Q to V and W bands. This suggests the possible presence of foregrounds residuals as they are more important at low frequencies and they add a negative contribution to f_{nl} [173].

We also estimate the contribution of the point sources for the V+W combined map as in Curto et al. [46]. We add the point source simulations to the CMB plus noise simulations. For each one of them we compute its best-fitting f_{nl} and compare it with the obtained for the same case without including the point source simulation. The difference returns an estimate of the contamination on f_{nl} due to point sources. For the V+W map we have $\Delta f_{nl} = 6 \pm 5$. Therefore our estimate taking into account the point sources is $-18 < f_{nl} < +80$ at 95% CL for the V+W map. Comparing with the best-fitting value for the V+W map given by Yadav & Wandelt [173], $f_{nl} = 87$, our analysis excludes that value at $\sim$99% CL.

5.3.2 Constraints on f_{nl} with the W band

The W map best-fitting f_{nl} value is only compatible with zero at 99% CL. This result is in apparent discrepancy with the values obtained for the V and V+W maps, which are compatible with zero at 95%CL. The point sources add a low contribution to the W map, $\Delta f_{nl} = 1 \pm 2$, and therefore they do not explain its best-fitting value of f_{nl} =65. We may wonder if that value can be obtained by a statistical fluctuation. Considering simulations with different models ($f_{nl} = 0$, $f_{nl} = 40$ and $f_{nl} = 70$) we have confirmed that the best-fitting f_{nl} for W is compatible with the values obtained for the V and V+W maps.

To understand the relatively large f_{nl} value found in the W map we have performed some additional tests. First of all, we have checked if this deviation could be due to the presence of residual foregrounds by studying the V-W map for the clean and the raw (before template subtraction) maps as well as the raw maps for the Q,V,W and V+W cases (see table 5.3). We find that there is a very significant (positive) deviation in the clean V-W map. Since this combination contains mainly residual foregrounds and noise, both could be responsible for the deviation. Interestingly, when we repeat the test for the raw V-W map, where foreground contamination should be more important, the best f_{nl} value becomes compatible with the simulations. This seems to indicate that foreground emission tends to bias the estimated f_{nl} towards lower values. This is also observed for the best f_{nl} value estimated for the raw Q, V, W and V+W maps, which is systematically lower than the one obtained for the clean maps. Therefore, for the case of the raw V-W map, some effect from systematics may be cancelled by foreground residuals.

If foregrounds are not responsible for the deviation found in the W and V-W maps, we may wonder if it is due to systematics present in the W radiometers. To test this possibility, we have studied two different combinations of the four W radiometers, where CMB and foregrounds are basically cancelled. One of these combinations is consistent with Gaussian simulations but the second one shows again a deviation at the 95 per cent CL, indicating the possible presence of some spurious signal in the noise of one or several of the W radiometers. In order to localise further the origin of this signal, we have also studied each W radiometer separately, finding a deviation at the level of 98 per cent for the W_2 radiometer, with a best f_{nl} value of 91, while the rest of the radiometers are consistent with the zero value at the 95 per cent CL. Finally we have also considered the difference between the two V radiometers, which is found to be compatible with Gaussianity. This further indicates that, if a systematic is responsible of the V-W map, this would be present in the W frequency channel

Table 5.3 Best-fitting f_{nl} values for different WMAP radiometers and combinations of them for raw and clean data. We also present the mean and the dispersion of the best-fitting f_{nl} values obtained from Gaussian simulations.

Map	foreground	best f_{nl}	$\langle f_{nl} \rangle$	$\sigma(f_{nl})$
V+W	raw	34	-1	25
Q	raw	-3	0	33
V	raw	16	0	30
W	raw	60	0	30
V-W	raw	-0.02	0.02	0.29
V-W	clean	1.02	0.02	0.29
W_1	clean	39	1	41
W_2	clean	91	-3	45
W_3	clean	23	2	47
W_4	clean	59	0	44
$W_1 + W_2 - W_3 - W_4$	clean	-0.52	0.00	0.34
$W_1 - W_2 + W_3 - W_4$	clean	0.85	0.00	0.35
$V_1 - V_2$	clean	-0.01	0.01	0.34

(see table 5.3).

All these tests suggest that the relatively large f_{nl} value obtained for W may come from systematics present in the W radiometers. In any case, a more exhaustive study is necessary in order to establish the origin of this deviation.

5.3.3 f_{nl} for the North and South hemispheres

The localization property of the wavelets allows a local analysis of the f_{nl} parameter. In particular, we test the Gaussianity and estimate the best-fitting f_{nl} value of the V+W combined map using only northern (Galactic latitude $b > 0$) and southern pixels ($b < 0$) in equation 5.2.1. For both cases the third order statistics obtained for the data are compatible with Gaussian simulations (inside the 2σ error bars). In table 5.4 we list the best-fitting f_{nl} values for the northern and southern hemispheres and the main properties of the distribution of the best-fitting f_{nl} obtained from 1,000 Gaussian simulations. We estimated the contribution of the unresolved point sources as in the previous subsection,

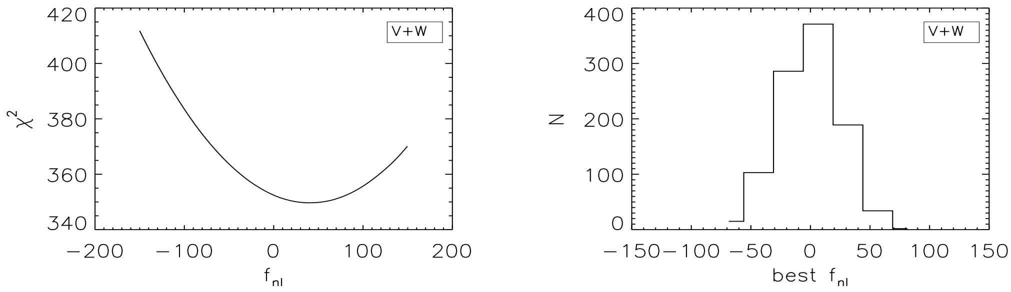

Figure 5.3 The $\chi^2(f_{nl})$ statistics versus f_{nl} for the V+W data map and the histogram for the best-fitting f_{nl} values for a set of 1000 Gaussian V+W simulations. The dispersion is $\sigma(f_{nl}) = 25$.

Table 5.4 Best-fitting f_{nl} values obtained for the northern and southern hemispheres. We also present the mean, dispersion and some percentiles of the distribution of the best fit f_{nl} values obtained from Gaussian simulations.

Region	best f_{nl}	$\langle f_{nl} \rangle$	$\sigma(f_{nl})$	$X_{0.160}$	$X_{0.840}$	$X_{0.025}$	$X_{0.975}$
North	46	2	37	-35	40	-71	74
South	35	-1	38	-39	37	-80	69

and the values are $\Delta f_{nl} = 7 \pm 7$ for the North and $\Delta f_{nl} = 5 \pm 7$ for the South. Taking into account this, the results are $-32 < f_{nl} < 113$ for the North and $-50 < f_{nl} < 99$ for the South at 95% CL. These values are compatible with zero at 95% CL. We also study the compatibility of the best-fitting value for the North and South hemispheres between them. We compute the difference of the best-fitting f_{nl} value $\Delta f_{nl} = f_{nl}^{(N)} - f_{nl}^{(S)}$ for the North and South hemispheres for the set of 1,000 V+W Gaussian simulations. The difference is $\Delta f_{nl}^{(data)} = 11$ for the data, and for the simulations is $\Delta f_{nl} = 3 \pm 55$. The cumulative probability is $P(\Delta f_{nl} \leq \Delta f_{nl}^{(data)}) = 0.57$ and therefore the difference for the data is compatible with the results obtained from simulations. This means that we do not find any asymmetry in the North-South f_{nl} value.

CHAPTER 6

Cubic statistics with wavelets

We study the spherical Mexican hat wavelet (SMHW) as a detector of primordial non-Gaussianity of the local type on the Cosmic Microwave Background (CMB) anisotropies. For this purpose we define third order statistics based on the wavelet coefficient maps and the unconvolved map. We find the dependence of these statistics in terms of the non-linear coupling parameter f_{nl} and the bispectrum of this kind of non-Gaussianity. We compare the analytical values for these statistics with the results obtained with non-Gaussian simulations for an ideal full-sky CMB experiment without noise.

Finally we study the power of this method to detect f_{nl}, i. e. the variance of this parameter $\sigma^2(f_{nl})$, and compare it with the $\sigma^2(f_{nl})$ obtained from the primary bispectrum for the same experiment. The results show that the wavelet cubic statistics are as efficient as the bispectrum as the optimal detector of this type of primordial non-Gaussianity.

6.1 The third order statistics

6.1.1 Introduction

The third order statistics of this analysis are based on the SMHW. See Antoine & Vandergheynst [6], Martínez-González et al. [120], Martínez-González [123], Vielva [167] for detailed information about the wavelets and a list of applications to the CMB anisotropies. Given a function $f(\mathbf{n})$ defined at a position $\mathbf{n}$ on the sphere and a continuous wavelet family on that space $\Psi(\mathbf{n}; \mathbf{b}, R)$, we define the continuous wavelet transform as

$$w(\mathbf{b};R) = \int d\mathbf{n} f(\mathbf{n}) \Psi(\mathbf{n};\mathbf{b},R) \tag{6.1.1}$$

where $\mathbf{b}$ is the position on the sky at which the wavelet coefficient is evaluated and R is the scale of the wavelet.

Considering a set of different angular scales $\{R_i\}$ we define a third order statistic depending on three scales $\{i,j,k\}$ [47]

$$q_{ijk} = \frac{1}{4\pi} \frac{1}{\sigma_i \sigma_j \sigma_k} \int d\mathbf{n} w(R_i,\mathbf{n}) w(R_j,\mathbf{n}) w(R_k,\mathbf{n}) \tag{6.1.2}$$

where σ_i is the dispersion of the wavelet coefficient map $w(R_i,\mathbf{n})$. In the particular case of $i=0$, $w(R_0,\mathbf{n}) = f(\mathbf{n})$. Using the properties of the wavelet, we have

$$w(R_i,\mathbf{n}) = \sum_{\ell m} a_{\ell m} \omega_\ell(R_i) Y_{\ell m}(\mathbf{n}) \tag{6.1.3}$$

and

$$\sigma_i^2 = \sum_\ell C_\ell (2\ell+1)/(4\pi) \omega_\ell^2(R_i) \tag{6.1.4}$$

where $\omega_\ell(R)$ is the window function of the wavelet at a scale R. It can be shown that $\omega_\ell(R)$ is [147]

$$\omega_\ell(R) = 2\pi \int_0^\pi d\theta sin\theta P_\ell(cos\theta) \Psi_S(\theta;R). \tag{6.1.5}$$

This means that the convolution with the wavelet is equivalent to filter the maps with a window function $\omega_l(R)$ which depends on the scale. In the figure 6.1 we plot the wavelet window function for several angular scales. For small scales, the wavelet filters low multipoles and viceversa. Therefore it is important to select a set of angular scales that ranges all the interesting multipoles.

6.1.2 The statistics and the primordial non-Gaussianity

Considering the equations 6.1.2 and 6.1.3, the third order moments can be written as

$$q_{ijk} = \frac{1}{4\pi} \frac{1}{\sigma_i \sigma_j \sigma_k} \sum_{\ell_1,\ell_2,\ell_3,m_1,m_2,m_3} a_{\ell_1 m_1} a_{\ell_2 m_2} a_{\ell_3 m_3} \omega_{\ell_1}(R_i) \omega_{\ell_2}(R_j) \omega_{\ell_3}(R_k) \times$$
$$\times \begin{pmatrix} \ell_1 & \ell_2 & \ell_3 \\ m_1 & m_2 & m_3 \end{pmatrix} \begin{pmatrix} \ell_1 & \ell_2 & \ell_3 \\ 0 & 0 & 0 \end{pmatrix} \sqrt{\frac{(2\ell_1+1)(2\ell_2+1)(2\ell_3+1)}{4\pi}}, \tag{6.1.6}$$

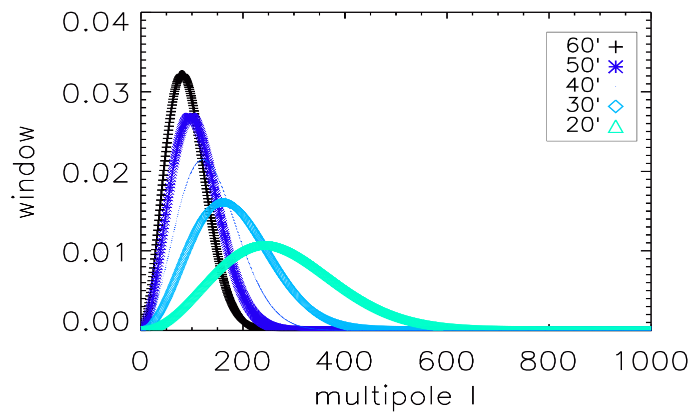

Figure 6.1 The window function for the SMHW at different angular scales. Note that the wavelet filters high multipoles for low angular scales and viceversa.

where we have used the Gaunt integral

$$\int d^2\mathbf{n} Y_{\ell_1 m_1}(\mathbf{n}) Y_{\ell_2 m_2}(\mathbf{n}) Y_{\ell_3 m_3}(\mathbf{n}) = \begin{pmatrix} \ell_1 & \ell_2 & \ell_3 \\ m_1 & m_2 & m_3 \end{pmatrix} \begin{pmatrix} \ell_1 & \ell_2 & \ell_3 \\ 0 & 0 & 0 \end{pmatrix} \sqrt{\frac{(2\ell_1+1)(2\ell_2+1)(2\ell_3+1)}{4\pi}} \quad (6.1.7)$$

The mean value of the third order statistic q_{ijk} can be written in terms of the reduced bispectrum defined in equation 1.4.33:

$$\langle q_{ijk} \rangle = \frac{1}{4\pi} \frac{1}{\sigma_i \sigma_j \sigma_k} \sum_{\ell_1, \ell_2, \ell_3} \omega_{\ell_1}(R_i) \omega_{\ell_2}(R_j) \omega_{\ell_3}(R_k) I^2_{\ell_1 \ell_2 \ell_3} b_{\ell_1 \ell_2 \ell_3}, \quad (6.1.8)$$

where $I_{\ell_1 \ell_2 \ell_3}$ is defined as

$$I_{\ell_1 \ell_2 \ell_3} = \begin{pmatrix} \ell_1 & \ell_2 & \ell_3 \\ 0 & 0 & 0 \end{pmatrix} \sqrt{\frac{(2\ell_1+1)(2\ell_2+1)(2\ell_3+1)}{4\pi}} \quad (6.1.9)$$

Now assuming a primordial gravitational potential of the form [93]

$$\Phi(\mathbf{x}) = \Phi_L(\mathbf{x}) + f_{nl} \times \left[\Phi_L^2(\mathbf{x}) - \langle \Phi_L(\mathbf{x}) \rangle^2 \right], \quad (6.1.10)$$

it is possible to derive its corresponding bispectrum (see equation 1.4.33) in terms of f_{nl}. The expected value of the third order moments is

$$\langle q_{ijk} \rangle_{f_{nl}} = \frac{1}{4\pi} \frac{f_{nl}}{\sigma_i \sigma_j \sigma_k} \sum_{\ell_1, \ell_2, \ell_3} \omega_{\ell_1}(R_i) \omega_{\ell_2}(R_j) \omega_{\ell_3}(R_k) I^2_{\ell_1 \ell_2 \ell_3} \times b^{prim}_{\ell_1 \ell_2 \ell_3}. \quad (6.1.11)$$

This means that the third order moments are proportional to f_{nl}

$$\langle q_{ijk} \rangle_{f_{nl}} = f_{nl} \times \alpha_{ijk}, \quad (6.1.12)$$

where

$$\alpha_{ijk} = \frac{1}{4\pi}\frac{1}{\sigma_i\sigma_j\sigma_k}\sum_{\ell_1,\ell_2,\ell_3}\omega_{\ell_1}(R_i)\omega_{\ell_2}(R_j)\omega_{\ell_3}(R_k)I^2_{\ell_1\ell_2\ell_3}\times b^{prim}_{\ell_1\ell_2\ell_3}. \tag{6.1.13}$$

The pixel properties are taken into account by replacing C_ℓ by $C_\ell\omega^{pix}_\ell\omega^{pix}_\ell$ in the equation 6.1.4 and $b^{prim}_{\ell_1\ell_2\ell_3}$ by $b^{prim}_{\ell_1\ell_2\ell_3}\omega^{pix}_{\ell_1}\omega^{pix}_{\ell_2}\omega^{pix}_{\ell_3}$ in the equation 6.1.13, where ω^{pix}_ℓ is the pixel window function [65].

We have evaluated the α_{ijk} statistics using the analytic equation 6.1.13 and non-Gaussian simulations for the set of 12 angular scales that we used in the chapter 5. We have used a full-sky ideal experiment without noise and a characteristic angular resolution of 6.9 arcmin. We need the primordial bispectrum defined in the equation 1.4.33 to evaluate analytically the statistics α_{ijk}. We have computed the primordial bispectrum up to $\ell_{max} = 1535$ using the $gTfast$ software by E. Komatsu [93] based on CMBFast [150] to evaluate the transfer function. The cosmological parameters for this analysis are $\Omega_{cdm} = 0.25$, $\Omega_b = 0.05$, $\Omega_\Lambda = 0.70$, $\tau = 0.09$, $h = 0.73$ and a scale invariant spectral index $n = 1$ for the power spectrum $P(k)$. We have used a set of 300 non-Gaussian simulations generated with the same cosmological parameters following the algorithm defined in Liguori et al. [109, 110]. The mean value of the α_{ijk} statistics of these simulations and its error-bars are plotted in the figure 6.2. These values are compared with the theoretical value obtained from equation 6.1.13. We can see that for most of the statistics there is agreement between the simulations and the analytic model . From the set of 364 statistics there are 2 cases with the analytic value at a 3σ distance with respect to the mean value. This value is the expected one for a set of 364 Gaussian-like variables.

6.1.3 The covariance of the third order statistics

The covariance matrix of the third order moments can be computed in the Gaussian limit using the properties of the covariance for the bispectrum. Considering the Gaussian case we have

$$C_{ijk,rst} = \langle q_{ijk}q_{rst}\rangle - \langle q_{ijk}\rangle\langle q_{rst}\rangle = \langle q_{ijk}q_{rst}\rangle. \tag{6.1.14}$$

From the definition of q_{ijk}

$$\langle q_{ijk}q_{rst}\rangle = \frac{1}{(4\pi)^2}\frac{1}{\sigma_i\sigma_j\sigma_k}\frac{1}{\sigma_r\sigma_s\sigma_t}\int \mathbf{d\hat{n}_1 d\hat{n}_2}\times$$
$$\times\langle w(R_i,\mathbf{n_1})w(R_j,\mathbf{n_1})w(R_k,\mathbf{n_1})w(R_r,\mathbf{n_2})w(R_s,\mathbf{n_2})w(R_t,\mathbf{n_2})\rangle. \tag{6.1.15}$$

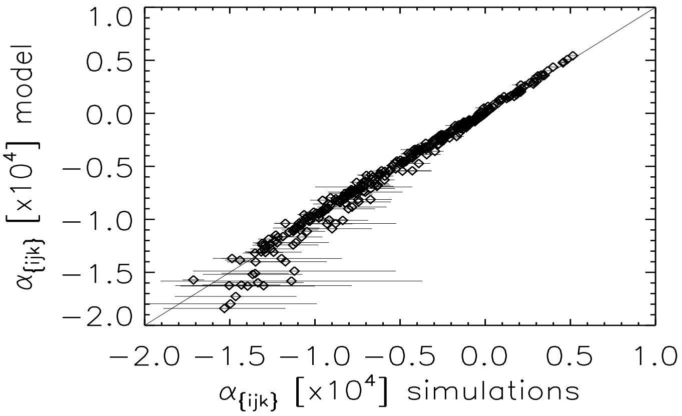

Figure 6.2 The α_{ijk} statistics computed analytically and with $n_{sim} = 300$ non-Gaussian simulations. The error-bars correspond to the dispersion $\sigma(\alpha_{ijk})/\sqrt{n_{sim}}$ obtained with the simulations.

Using the Wick's theorem and the properties of Gaussian distributions [see equation 13 of 77]

$$\begin{aligned}\langle w(R_i,\mathbf{n_1})w(R_j,\mathbf{n_1})w(R_k,\mathbf{n_1})w(R_r,\mathbf{n_2})w(R_s,\mathbf{n_2})w(R_t,\mathbf{n_2})\rangle =\\ \langle w(R_i,\mathbf{n_1})w(R_j,\mathbf{n_1})\rangle\langle w(R_k,\mathbf{n_1})w(R_r,\mathbf{n_2})\rangle\langle w(R_s,\mathbf{n_2})w(R_t,\mathbf{n_2})\rangle\\ + \, permutations \; (total \; 15 \; terms)\end{aligned} \tag{6.1.16}$$

From these terms, there are only 6 that do not vanish in equation 6.1.15. They are those which involve the two coordinates $\mathbf{n_1}$ and $\mathbf{n_2}$ in the same average. Taking this into account and the properties of the two point correlation functions [see equation 14 of 77] we have

$$\begin{aligned}\langle q_{ijk}q_{rst}\rangle = \frac{1}{(4\pi)^2}\frac{1}{\sigma_i\sigma_j\sigma_k}\frac{1}{\sigma_r\sigma_s\sigma_t}\sum_{l_1l_2l_3} I^2_{l_1l_2l_3}C_{l_1}C_{l_2}C_{l_3}\times\\ \times\{\omega_{l_1}(R_i)\omega_{l_1}(R_r)\omega_{l_2}(R_j)\omega_{l_2}(R_s)\omega_{l_3}(R_k)\omega_{l_3}(R_t)+\\ +\omega_{l_1}(R_i)\omega_{l_1}(R_r)\omega_{l_2}(R_j)\omega_{l_2}(R_t)\omega_{l_3}(R_k)\omega_{l_3}(R_s)+\\ +\omega_{l_1}(R_i)\omega_{l_1}(R_s)\omega_{l_2}(R_j)\omega_{l_2}(R_r)\omega_{l_3}(R_k)\omega_{l_3}(R_t)+\\ +\omega_{l_1}(R_i)\omega_{l_1}(R_s)\omega_{l_2}(R_j)\omega_{l_2}(R_t)\omega_{l_3}(R_k)\omega_{l_3}(R_r)+\\ +\omega_{l_1}(R_i)\omega_{l_1}(R_t)\omega_{l_2}(R_j)\omega_{l_2}(R_r)\omega_{l_3}(R_k)\omega_{l_3}(R_s)+\\ +\omega_{l_1}(R_i)\omega_{l_1}(R_t)\omega_{l_2}(R_j)\omega_{l_2}(R_s)\omega_{l_3}(R_k)\omega_{l_3}(R_r)\}\end{aligned} \tag{6.1.17}$$

The pixel properties are taken into account here by replacing C_ℓ by $C_\ell\omega_\ell^{pix}\omega_\ell^{pix}$.

6.1.4 Fisher matrix of the third order statistics

We discuss the detectability of the primary non-Gaussianity with the third order moments. Assuming that the third order statistics are Gaussian-like (due to the central limit theorem this approximation holds very well for high resolution maps in equation 6.1.2), it is optimal to use the Gaussian likelihood to constrain the f_{nl} parameter

$$L(f_{nl}) = C_0 \times e^{-\chi^2(f_{nl})/2} \tag{6.1.18}$$

where C_0 is a constant and $\chi^2(f_{nl})$ is

$$\chi^2(f_{nl}) = \sum_{ijk,rst} (q^{obs}_{ijk} - \langle q_{ijk}\rangle_{f_{nl}}) C^{-1}_{ijk,rst} (q^{obs}_{rst} - \langle q_{rst}\rangle_{f_{nl}}). \tag{6.1.19}$$

$C^{-1}_{ijk,rst}$ is the inverse of the covariance matrix of the third order statistics that we have computed analytically in the previous section, q^{obs}_{ijk} are the third order statistics obtained from the data and $\langle q_{ijk}\rangle_{f_{nl}}$ are the expected values of the third order statistics for a given model with f_{nl}. As we have seen in section 6.1.2, $\langle q_{ijk}\rangle_{f_{nl}} = f_{nl}\alpha_{ijk}$, with α_{ijk} a constant independent of f_{nl}. Using this on equation 6.1.19

$$\chi^2(f_{nl}) = \sum_{ijk,rst} (q^{obs}_{ijk} - f_{nl}\alpha_{ijk}) C^{-1}_{ijk,rst} (q^{obs}_{rst} - f_{nl}\alpha_{rst}). \tag{6.1.20}$$

The variance of the f_{nl} parameter can be computed using the Fisher matrix

$$\sigma^2(f_{nl}) = \frac{-1}{\frac{\partial^2 logL(f_{nl})}{\partial f^2_{nl}}} = \frac{1}{\frac{1}{2}\frac{\partial^2\chi^2(f_{nl})}{\partial f^2_{nl}}}. \tag{6.1.21}$$

The second derivative of the $\chi^2(f_{nl})$ with respect to f_{nl} in equation 6.1.20 is

$$\frac{\partial^2\chi^2(f_{nl})}{\partial f^2_{nl}} = 2\sum_{ijk,rst} \alpha_{ijk} C^{-1}_{ijk,rst} \alpha_{rst}. \tag{6.1.22}$$

Therefore introducing equation 6.1.22 into equation 6.1.21 we obtain

$$\sigma^2(f_{nl}) = \frac{1}{\sum_{ijk,rst} \alpha_{ijk} C^{-1}_{ijk,rst} \alpha_{rst}}. \tag{6.1.23}$$

6.2 Constraints on f_{nl} with the primary bispectrum and wavelets

We compare the constraints on f_{nl} using the primordial bispectrum Fisher matrix following the method described in [93] and the wavelets as described in section 6.1.4.

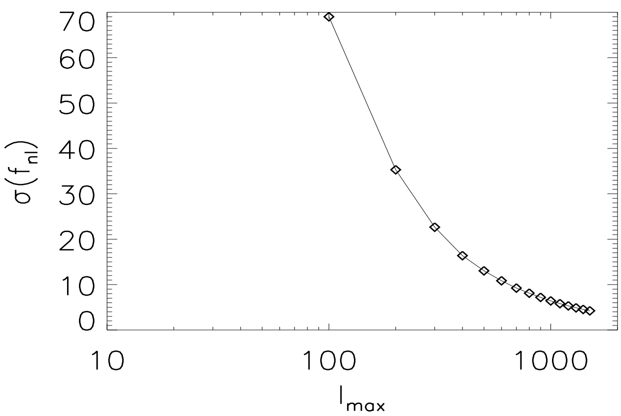

Figure 6.3 $\sigma(f_{nl})$ for different ℓ_{max} using the Fisher matrix of the bispectrum (equations 1.4.36 and 1.4.37).

6.2.1 $\sigma(f_{nl})$ with the primordial bispectrum

We consider the primordial bispectrum described in section 1.4.4, a noiseless experiment with an angular resolution of 6.9 arc minutes ($\ell_{max} = 1535$), and a cosmological model characterised by $\Omega_{cdm} = 0.25$, $\Omega_b = 0.05$, $\Omega_\Lambda = 0.70$, $\tau = 0.09$, $h = 0.73$ and $n = 1$. The variance of f_{nl} is computed through the Fisher matrix of the bispectrum (see equations 1.4.36 and 1.4.37). We have computed $\sigma(f_{nl})$ for different $\ell_3 \leq \ell_{max}$ (see figure 6.3). Note that as we include higher multipoles (i.e. smaller scales) $\sigma(f_{nl})$ decreases obtaining a limit of $\sigma(f_{nl}) = 4.13$ for $\ell_{max} = 1535$.

6.2.2 $\sigma(f_{nl})$ with wavelets

We consider the ideal experiment and the cosmological parameters used in section 6.2.1 for the primordial bispectrum. To maximise the non-Gaussian signal we take a wide interval of different angular scales. We select 21 angular scales from 2.9 arc minutes to 167.07 degrees logarithmically spaced. See table 6.1 for the list of considered scales and figure 6.4 for the wavelet window function corresponding to these scales. We compute the third order quantities α_{ijk} given by the equation 6.1.13 and the covariance matrix of the q_{ijk} statistics given by the equation 6.1.17 for these angular scales. There are $(21 + 3 - 1)!/[3!(21 - 1)!] = 1771$ different third order statistics for 21 angular scales.

Table 6.1 List of 21 angular scales logarithmically spaced between 6.9 arc minutes to 167.07 degrees. These scales are used to obtain $\sigma(f_{nl})$ with wavelets.

index i	0	1	2	3	4	5	6
scale R_i	map	$2.9'$	$4.5'$	$6.9'$	$10.6'$	$16.3'$	$24.9'$
index i	7	8	9	10	11	12	13
scale R_i	$38.3'$	$58.7'$	$90.1'$	$138.3'$	$212.3'$	$325.8'$	$500'$
index i	14	15	16	17	18	19	20
scale R_i	$767.3'$	$1177.6'$	$1807.2'$	$2773.4'$	$4256.3'$	$6531.9'$	$10024.3'$

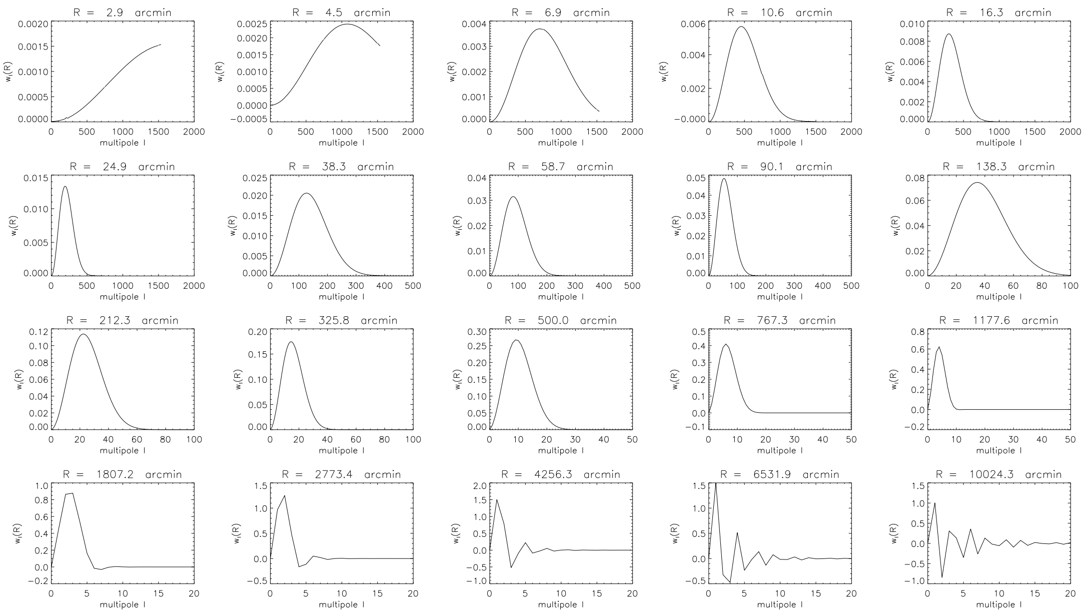

Figure 6.4 The window function of the SMHW for the selected angular scales. Note that the scales of 2.9 and 4.5 arc minutes are lower than the pixel size (6.9 arc minutes). However they provide additional information because of the shape of the wavelet.

The variance of f_{nl} given by equation 6.1.23 requires the inverse of the covariance matrix $C_{ijk,rst}$. This covariance matrix has a large condition number (defined as the ratio of the maximum and minimum eigenvalues). This implies that the computation of its inverse is an ill-conditioned problem. Therefore the numerical errors present due to the limited precision of our computers (of the order of $2^{1-53} \simeq 10^{-16}$) can affect the value of $\sigma(f_{nl})$.

To reduce the condition number, and therefore the errors in $\sigma(f_{nl})$, we proceed by removing subsets of statistics that are highly correlated (above a given

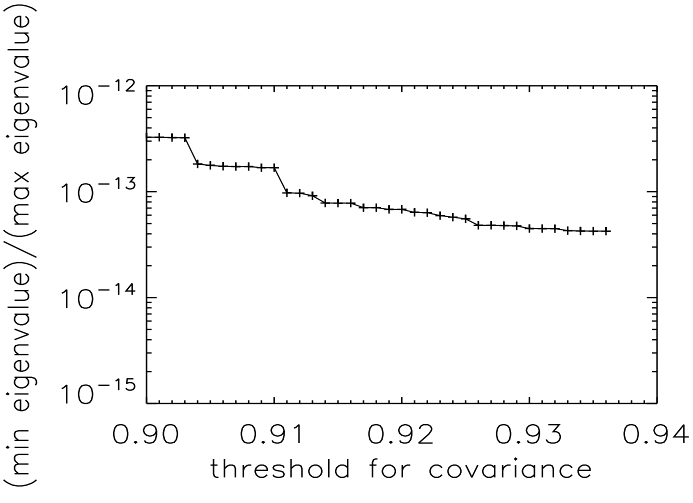

Figure 6.5 The inverse of the condition number of the covariance matrix for different thresholds for the highly correlated statistics. The covariance matrix for thresholds greater than 0.936 has a negative minimum eigenvalue which suggests significant errors since a covariance matrix is positive definite.

threshold) to the remaining statistics. In figure 6.5 we plot the values of the condition number of the covariance matrix for different thresholds for the highly correlated statistics. On the other side, we propagate errors from $C^{-1}_{ijk,rst}$ to $\sigma(f_{nl})$. The best estimate of the $\sigma(f_{nl})$ is obtained by a balance between the maximum acceptable errors for $\sigma(f_{nl})$ and the minimum number of rejected statistics. Note that it is important to use as many scales as possible in order to collect the maximum non-Gaussian signal in a similar way as for the bispectrum.

In order to compute the errors in $\sigma(f_{nl})$ in terms of the errors of C^{-1} we consider the equation 6.1.23 and define $y \equiv \sigma^2(f_{nl})$ and $x_{ijk,rst} \equiv C^{-1}_{ijk,rst}$. We assume that the numerical errors of each element of the covariance matrix are Gaussian and independent. Then we can write

$$\sigma^2(y) = \sum_{ijk,rst} \left(\frac{\partial y}{\partial x_{ijk,rst}} \right)^2 \sigma^2(x_{ijk,rst}). \tag{6.2.1}$$

Doing some straightforward calculations one can obtain easily that

$$\frac{\sigma^2(y)}{y^2} = \frac{\sum_{ijk,rst} \alpha^2_{ijk} \sigma^2(x_{ijk,rst}) \alpha^2_{rst}}{(\sum_{ijk,rst} \alpha_{ijk} x_{ijk,rst} \alpha_{rst})^2}. \tag{6.2.2}$$

Now considering $z \equiv \sqrt{y} = \sigma(f_{nl})$, we have that

$$\frac{\sigma^2(z)}{z^2} = \frac{1}{4y^2}\sigma^2(y). \tag{6.2.3}$$

and therefore

$$\frac{\sigma(z)}{z} = \frac{\sigma(\sigma(f_{nl}))}{\sigma(f_{nl})} = \frac{1}{2}\frac{\sqrt{\sum_{ijk,rst}\alpha_{ijk}^2\sigma^2(x_{ijk,rst})\alpha_{rst}^2}}{(\sum_{ijk,rst}\alpha_{ijk}x_{ijk,rst}\alpha_{rst})}. \tag{6.2.4}$$

Now we need an estimation of the errors of the inverse covariance matrix. Considering the computed inverse matrix C_{app}^{-1} we can write

$$C_{app}^{-1} = C^{-1} + \Delta C^{-1}, \tag{6.2.5}$$

where C^{-1} is the exact inverse matrix of C and ΔC^{-1} are the errors of the approximate inverse matrix. Multiplying C and C_{app}^{-1}

$$C \times C_{app}^{-1} = C \times (C^{-1} + \Delta C^{-1}) \equiv I + R_{res} \tag{6.2.6}$$

where R_{res} is a residual matrix and I is the identity matrix. Therefore we can write

$$C \times \Delta C^{-1} = R_{res}. \tag{6.2.7}$$

Now if we multiply the elements of equation 6.2.7 by C_{app}^{-1}

$$C_{app}^{-1} \times C \times \Delta C^{-1} = C_{app}^{-1} \times R_{res}. \tag{6.2.8}$$

The $C_{app}^{-1} \times C \times \Delta C^{-1}$ matrix product can be written as

$$C_{app}^{-1} \times C \times \Delta C^{-1} = (C^{-1} + \Delta C^{-1}) \times C \times \Delta C^{-1} = \Delta C^{-1} + \Delta C^{-1} \times C \times \Delta C^{-1}. \tag{6.2.9}$$

The $\Delta C^{-1} \times C \times \Delta C^{-1}$ matrix in equation 6.2.9 is a second order quantity compared with ΔC^{-1} and therefore it can be neglected[1]. Using this approximation and the equation 6.2.8 we have

$$\Delta C^{-1} \simeq C_{app}^{-1} \times R_{res} \tag{6.2.10}$$

which gives a direct estimate of the errors of the inverse covariance matrix in terms of R_{res} and C_{app}^{-1} that can be computed easily.

In figure 6.6 we plot $\sigma(f_{nl})$ and its relative error due to the errors in the inverse covariance matrix. We can see that for low thresholds (~ 0.90), the relative errors of $\sigma(f_{nl})$ are negligible because the covariance matrix is not ill-conditioned and the errors in the inverse are irrelevant. However, in this situation a significant fraction of the non-Gaussian signal is lost with the rejected statistics

[1] We have checked that each element of the $\Delta C^{-1} \times C \times \Delta C^{-1}$ matrix is at least 10^6 times lower than the corresponding element of the ΔC^{-1} matrix for thresholds of ~ 0.92

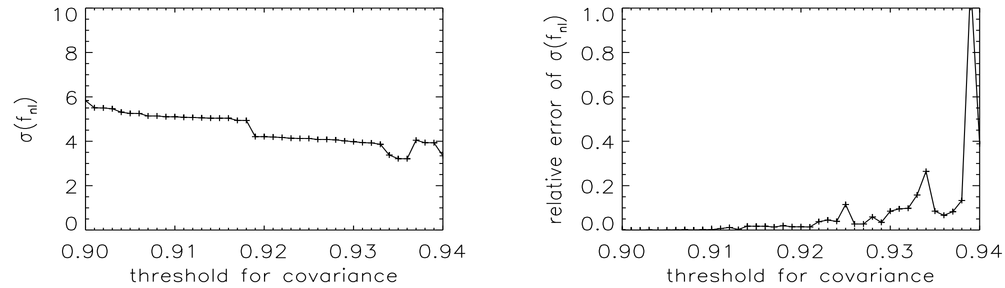

Figure 6.6 *From left to right,* $\sigma(f_{nl})$ and its relative error due to the errors in the inverse covariance matrix.

and therefore $\sigma(f_{nl}) \sim 6$. As the threshold for the correlations is increased the number of available statistics is larger, the non-Gaussian signal is more important and $\sigma(f_{nl})$ decreases. When the threshold is 0.925 the relative error is 11% and for higher thresholds the errors become more important. Considering 10% as an upper limit for the error $\sigma(f_{nl}) = 4.21$. This value is very similar to the $\sigma(f_{nl})$ obtained with the Fisher matrix of the primordial bispectrum. Therefore we have shown that a wavelet based method is as efficient as a bispectrum based method to constrain the primordial non-Gaussianity of the local type in this ideal experiment.

CHAPTER 7

Conclusions

The search of non-Gaussian deviations in the CMB anisotropies has become a question of considerable interest, as it can be used to discriminate different possible scenarios of the early Universe and also to study the secondary sources of non-Gaussianity. The standard single-field and slow roll inflation predicts that the fluctuations generated during inflation and imprinted in the CMB anisotropies are nearly Gaussian distributed. We have reviewed alternative inflationary models and other sources of primordial non-Gaussianity in chapter 1. Several tests of non-Gaussianity on CMB anisotropies maps have been presented in this thesis. The data collected by the Archeops experiment (a technological precedent of the Planck LFI instrument) has been analysed using a goodness-of-fit test and the Minkowski functionals. We have constrained the levels of atmospheric and dust contamination for this experiment and imposed constraints on the f_{nl} parameter. The data of the WMAP experiment has been analysed using several estimators based on the SMHW. In a first analysis we have constrained f_{nl} to values that are compatible with zero and equivalent to the results presented by the WMAP team. We have done a second analysis where all the possible third order statistics are considered. In this case, the constraints on f_{nl} have been improved. Finally we have studied the efficiency of the wavelet to detect f_{nl} and its dependence with the bispectrum, considered the most efficient detector of this kind of non-Gaussianity. Let us summarise the conclusions of each chapter of this thesis.

7.1 Chapter 2

In this chapter we have performed a Gaussianity analysis of the Archeops data at low resolution using the smooth tests of goodness-of-fit and the Minkowski functionals.

The expected behaviour of the U_i^2 statistics as a χ_1^2 distribution has been confirmed for the order index interval $1 \leq i \leq 4$ with "realistic" simulations assuming Gaussian CMB anisotropies. For higher moments, $i > 4$, the mean of the distribution is $\mu \simeq 1$ but the dispersion is $\sigma \gtrsim 2$. This is because of the propagation of errors through higher order moments which in practice complicates the use of high order U_i^2 in our analysis.

From the analysis of both kinds of Archeops maps, coaddition and Mirage, we have found that both are compatible with Gaussianity. Only the U_2^2 statistic for coaddition map is close to 8 for low $(s/n)_c$. Although in principle the probability that U_2^2 takes values greater than 8 for a given signal-to-noise cut in the Gaussian hypothesis is very low (see table 2.3), the corresponding "p-value" for having U_2^2 larger than 8 at any signal-to-noise cut is 0.1482. This is not negligible and thus this detection is not significant. Moreover this effect does not appear in the Mirage map, and therefore should be assigned to issues related to the map-making process.

The analysis with the Minkowski functionals on the Mirage map also returns compatibility with Gaussianity.

Our analysis also implies constraints on the amount of contamination that can be present at 143 GHz. Using as template for dust and atmosphere the Archeops map at 353 GHz, we limit the possible contamination to be lower than 7.8% at 90% CL using U_2 statistic. A similar limit is obtained with the Minkowski functionals.

We also compared the Archeops results with the WMAP 1 and 3-year data in the same region of the sky. For both sets of data, a sharp peak in U_2^2 was found at specific signal-to-noise cuts. Although the probability of finding such a peak at a given signal-to-noise cut is very small, the "p-value" obtained when different cuts are allowed is appreciable. Therefore we can conclude that the WMAP data, when the same region as Archeops is considered, are also consistent with Gaussianity. The same conclusion is reached when the data are analysed with the Minkowski functionals.

Finally, we established a constraint in the value of the non-linear coupling parameter f_{nl}. Analysing Archeops data, we found that $f_{nl} = 200\,^{+900}_{-600}$ at 90% CL, and $f_{nl} = 200\,^{+1100}_{-800}$ at 95% CL. When the same analysis was done with WMC3 data using Archeops-WMAP combined mask, we found $f_{nl} = 100\,^{+400}_{-300}$ at 90% CL, $f_{nl} = 100\,^{+500}_{-400}$ at 95% CL. These limits are similar to those expected for an Archeops-like experiment with a noise amplitude similar to that of WCM3.

7.2 Chapter 3

In this chapter we have presented a complete Gaussianity analysis of the Archeops data at 143 GHz using the Minkowski functionals. First, we characterised the Archeops instrumental noise by taking the difference of the data of the two most sensitive bolometers, 143K03 and 143K04. From this we found non-Gaussian deviations at high resolution, 27 arcmin ($N_{side} = 128$ in the Healpix pixelization scheme). This is due to the noisiest pixels for which at high resolution the number of observations per pixel does not allow good systematic error removal. A more detailed analysis has been performed for the $143K03$ bolometer for which a noise map was obtained by subtracting the WMAP CMB data. From this analysis we found that pixels with a number of observations below 90 were non-Gaussian. Masking out those pixels, the noise map is compatible with a Gaussian model. Similar results were obtained with the $143K04$ bolometer although the minimum number of observations per pixel for Gaussianity was of the order of 150 and was not considered for further analysis.

Second, masking out these highly noisy pixels we performed a Gaussianity analysis of the Archeops $143K03$ data at low and high resolution. We found that the data are compatible with Gaussianity at $N_{side} = 32$, $N_{side} = 64$, $N_{side} = 128$, and for the combinations $N_{side} = 32, 64$, and for the combinations $N_{side} = 32, 64, 128$ at better than 95% CL. From this analysis and using realistic non-Gaussian simulations (Liguori et al. [109]) we imposed constraints on the f_{nl} parameter at these resolutions. The tightest constraints are $f_{nl} = 70^{+590}_{-400}$ at 68% CL and $f_{nl} = 70^{+1075}_{-920}$ at 95% CL.

Third, we also imposed constraints on f_{nl} using the Sachs-Wolfe approximation, $f_{nl}^{SW} = 25^{+200}_{-150}$ at 68% CL and $f_{nl}^{SW} = 25^{+375}_{-300}$ at 95% CL. For comparison notice that these constraints are a factor of ≈ 3 smaller than those given in Curto et al. [44] where only low resolution ($N_{side} = 32$) maps were considered.

Finally, we performed a detailed comparison of the realistic non-Gaussian simulations used in this chapter and those from the Sachs-Wolfe approximation. From this we conclude that even at low resolution the Sachs-Wolfe approximation overestimates the non-Gaussianity of the CMB fluctuations and therefore the f_{nl} constraints imposed are too tight by a factor of three, as shown above.

7.3 Chapter 4

We have analysed the 5-year WMAP data using Gaussian and realistic non-Gaussian simulations through a wavelet-based test. We have considered different combined maps for the analysis: Q+V+W, V+W, Q, V, and W. We have considered two kinds of extended masks to analyse the V+W map (defined in section 4.2.2). The third order moments (equation 4.2.1) of the wavelet coefficients of these maps are compatible with Gaussian simulations (see figure 4.2).

We have performed a χ^2 analysis and found that the data are indeed compatible with Gaussian simulations (see figure 4.3). We performed another χ^2 analysis to constrain the non-linear coupling parameter f_{nl} by using non-Gaussian simulations with f_{nl}. The best-fit f_{nl} values of the five analysed maps are compatible with the ones obtained by Komatsu et al. [97] using the bispectrum, showing similar confidence intervals and also a similar trend with the frequency.

Finally we have estimated the contribution to f_{nl} from unresolved point sources for the V+W map using a simple model that has point sources with constant intensity ($F_{src} = 0.5$ Jy) and a realistic model given by de Zotti et al. [176]. We have found that they add a positive contribution of $\Delta f_{nl} = 11 \pm 4$ for the simple model and $\Delta f_{nl} = 17 \pm 5$ for the realistic model. These values are larger than the one obtained by Komatsu et al. [97] for the bispectrum, which can be explained by the enhancement of the point sources produced by wavelets. Using the less restrictive extended masks, the point source distribution add a positive contribution of $\Delta f_{nl} = 3 \pm 4$ for the simple model and $\Delta f_{nl} = 3 \pm 5$ for the realistic model. The smaller values are explained because the less restrictive extended masks add some pixels that affect the efficiency of the wavelet to detect point sources. Taking into account the point source correction, our best estimate of f_{nl} is $-8 < f_{nl} < +111$ at 95% CL. It is important to emphasise the agreement found between the two estimators (bispectrum and wavelets), since they are formed by very different combinations of the data and are affected by systematic effects (like the mask, noise, beam response and foreground residuals) in very different ways.

7.4 Chapter 5

We have tested the Gaussianity and constrained the f_{nl} parameter with the 5-yr WMAP data. We use an optimal wavelet-based test. We have considered the V+W, Q, V and W combined maps at high resolution. We have used a set of 300 realistic non-Gaussian simulations and thousands of Gaussian simulations for the analysis. We have computed the wavelet coefficient maps at scales from 6.9 arcmin to 500 arcmin and computed all the possible third order moments (equation 5.2.1) using appropriate extended masks.

The data are compatible with Gaussian simulations for the considered combined maps (see table 5.1). We have imposed constraints on the non-linear coupling parameter f_{nl} by using non-Gaussian simulations with f_{nl}. The results show that f_{nl} increases when we go from the Q to the V and W combined maps. This frequency dependence also appears in the results by Curto et al. [46], Komatsu et al. [97], Yadav & Wandelt [173]. The results are compatible with zero at 95% CL for the V+W, Q, and V combined maps, but not for the W map (which is compatible at 99% CL). This value cannot be explained by unresolved point sources since their contribution is $\Delta f_{nl} = 1 \pm 2$ for the W map. We have estimated the probability of having those values with simulations and the results do not show incompatibility among different channels. We have also seen that the relatively large f_{nl} value obtained for the W band may come from systematics in one or several radiometers of this band.

We have also estimated the contribution of unresolved point sources to f_{nl} for the V+W map using a realistic model given by de Zotti et al. [176]. The results are $\Delta f_{nl} = 6 \pm 5$. Taking into account this value, our best estimate for f_{nl} is $-18 < f_{nl} < +80$ at 95% CL. The use of new scales and all the possible third order moments has returned better constrains to f_{nl} and lower error bars compared with the results by Curto et al. [46] and previous works. Our best estimate is compatible with the values obtained by Komatsu et al. [97] and it excludes the best-fitting f_{nl} value obtained by Yadav & Wandelt [173] at the $\sim$99% CL.

Finally we have constrained f_{nl} for the North and South hemispheres and the results give two best-fitting values that are compatible with zero at 95% CL and also are compatible between them. Therefore we do not find any North-South asymmetry for this parameter.

7.5 Chapter 6

We have developed an efficient method to constrain the local f_{nl} with the CMB anisotropies based on wavelets. We have found the dependence of the third order moments defined in equation 6.1.2 with f_{nl} and the cosmological model through the primordial bispectrum (see equation 6.1.13). On the other hand we have found an analytical expression for the covariance matrix for all the third order statistics (see equation 6.1.17). Assuming a Gaussian-like distribution for the third order moments, we have estimated the variance of f_{nl} through the method of maximum likelihood for the f_{nl} parameter (section 6.1.4). This variance is compared with the variance obtained through the Fisher matrix of the bispectrum in section 6.2. Both cases have been applied to an ideal experiment with an angular resolution of 6.9 arcmin and without instrumental noise. After a meticulous analysis of the influence of the errors in the computation of the inverse of the covariance matrix, we have found that $\sigma(f_{nl}) = 4.21$ when we use the wavelets whereas $\sigma(f_{nl}) = 4.13$ when we use the bispectrum. This result indicates that wavelets can be as efficient as the bispectrum to detect the non-Gaussianity of the local type. Apart from the efficiency of the tool it is remarkable that, as they are different statistical estimators, they may be sensitive to different systematics in real data. Moreover wavelets allow us to test the isotropic character of the f_{nl} parameter. We stress the importance of this statistical tool as an efficient alternative to measure local f_{nl} in near-future experiments as Planck.

7.6 Future Work

There are several models for the primordial non-Gaussianity which produce different forms for the CMB bispectrum as for example the *equilateral* and *local* shapes. These models have been constrained in many works [see for example 36, 37, 97]. Other models, as for example the *warm* and *flat* shapes are studied in [61]. In addition there are other general models of local-type of non-Gaussianity characterised with the τ_{nl} and g_{nl} parameters [91].

The local f_{nl} parameter has been constrained in this thesis using the SMHW with optimal results. The analyses described in chapters 4 and 5 show equivalent results to the values obtained with the bispectrum [97]. In chapter 6 we show the relation between wavelets and the bispectrum for the local shape. Similar tests can be performed with other shapes. This will open a new window in the search of different kind of primordial non-Gaussianity and it will allow one to discriminate different inflationary scenarios. A further work to be performed is the search of non-Gaussianities present in the trispectrum through the use of four-order statistics based in the wavelet coefficients.

Improved results can be achieved for the realistic case with masks by filling the masked out regions with constrained realisations. In this case the extended masks are not necessary. This would mean that for each scale there will be more available area, specially for the largest scales. In addition we could use greater scales than the ones allowed by the extended masks (see section 4.2.2) which are very relevant to constrain f_{nl} when they are combined with small scales. As a consequence the uncertainties for the f_{nl} parameter would be reduced, making the wavelet-based method more efficient.

CHAPTER 8

Resumen en Castellano

8.1 Introducción

8.1.1 La Radiación del Fondo Cósmico de Microondas

Cuando observamos la radiación electromagnética procedente del cielo en el rango de las microondas nos encontramos con una señal isótropa. Esta radiación, conocida como la radiación del fondo cósmico de microondas (RFCM), llena todo el espacio de forma muy uniforme y su espectro electromagnético es muy parecido al de un cuerpo negro con una temperatura de unos 3 K. La RFCM no se ha formado en unas condiciones como las del Universo actual. La interpretación estándar que explica su origen es que esta radiación muestra una imagen del Universo cuando este tenía unos 400.000 años de edad, momento en el cual el Universo se enfrió lo suficiente como para que la radiación y la materia dejasen de interaccionar y el espacio se hiciese transparente para los fotones. A partir de entonces esta radiación se ha ido enfriando hasta alcanzar la baja temperatura de 3 K que tenemos hoy en día.

El descubrimiento de la RFCM confirmó una de las principales predicciones de la teoría del *Big Bang* (Gran Explosión en inglés) propuesta en 1948 por G. Gamow y sus colaboradores [5] frente a otras alternativas, como por ejemplo el modelo del Universo estacionario, desarrollado por Alfred Hoyle y sus colaboradores [22, 82]. De acuerdo con el modelo del Big Bang, el Universo se formó hace aproximadamente unos catorce mil millones de años a partir de un estado de muy alta densidad y temperatura. Además, el Big Bang explica la formación de núcleos ligeros (H, He, Li ...) con mucha precisión, así como la expansión del Universo, observada por primera vez por E. Hubble en 1929 [83].

El modelo del Big Bang predice la existencia de una radiación de fondo isótropa a unos 5 K de temperatura. En 1965 esta radiación fue descubierta casualmente por A. Penzias y R. Wilson [138] (premiados con el Nobel de Física por este descubrimiento) e interpretada como una reliquia del Big Bang por R. Dicke y sus colaboradores [49].

Después del descubrimiento de la RFCM se han llevado a cabo muchos experimentos para observar y caracterizar esta radiación. En 1989 se lanzó COBE (Cosmic Background Explorer), el primer satélite espacial para estudiar la RFCM. Este satélite tenía dos instrumentos principales para observar la RFCM. El primero era el FIRAS (Far Infrared Absolute Spectrophotometer) dedicado a medir la intensidad de la RFCM (ver la figura 1.1) y el segundo era el DMR (Differential Microwave Radiometer) dedicado a medir las anisotropías de la RFCM (ver la figura 1.2). El éxito de esta misión permitió que los investigadores principales de COBE, G. Smoot y J. Mather, recibieran el premio Nobel de Física en 2006.

Las siguientes generaciones de experimentos se dedicaron principalmente a la observación en más detalle de las anisotropías de la RFCM que detectó COBE, del orden de $\Delta T/T \sim 10^{-5}$. A lo largo de los años 90 del siglo XX y los primeros años del siglo XXI se desarrollaron numerosos experimentos en tierra y se lanzaron varios globos estratosféricos para observar esas anisotropías. Los experimentos MAXIMA y BOOMERanG detectaron el primer máximo en la potencia de las anisotropías [19, 73], mientras que el experimento Archeops fue el primero en conectar las grandes escalas observadas por COBE con las pequeñas escalas detectadas por MAXIMA y BOOMERanG [16].

En 2001 la NASA lanzó su segundo satélite dedicado a la observación de la RFCM, el satélite WMAP (Wilkinson Microwave Anisotropy Probe). Este satélite fue enviado al punto de estabilidad conocido como Lagrangiano 2, L2, en el sitema Sol-Tierra, a una distancia de unos 1.5 millones de Km de la Tierra. Este satélite ha producido y sigue produciendo mapas de anisotropías de la RFCM a diferentes frecuencias entre 23 GHz y 94 GHz con mucha precisión. El día 14 de mayo de 2009 la Agencia Europea del Espacio lanzó Planck, el tercer satélite dedicado a la observación de las anisotropías de la RFCM. Planck tiene dos instrumentos principales, el LFI (Low Frequency Instrument) y el HFI (High Frequency Instrument), que operan en frecuencias entre los 30 y los 857 GHz. La misión Planck producirá mapas de anisotropías de todo el cielo con una resolución y contraste sin precedentes.

Los últimos cuarenta años de observaciones de la RFCM han servido para tener información que nos da una descripción concisa del Universo hasta épocas muy remotas. En particular, las anisotropías de la RFCM nos permiten medir con mucha precisión los parámetros que caracterizan el Universo. Mediciones independientes de dichos parámetros, por ejemplo usando la estructura a gran escala y las supernovas confirman los valores de los principales parámetros cosmológicos. El modelo ΛCDM (Λ-Cold Dark Matter) del Big Bang es el que mejor se ajusta a todas esas predicciones y por ello es conocido también como modelo concordante. Λ es la constante cosmológica que explica la expansión cada vez más acelerada que se ha observado recientemente. La naturaleza microscópica de este efecto es desconocida, y se llama energía oscura. CDM es el modelo con materia oscura fría, es decir, materia no bariónica y de naturaleza también poco conocida. De esta materia se sabe, además de que no es bariónica, que sólo interaciona de forma perceptible con el resto de la materia a través de la gravedad y que se mueve a velocidades no relativistas. Este modelo asume un Universo sin curvatura espacial, y sin topología observable, es decir, que su tamaño es mucho mayor que el horizonte (la distancia que un fotón ha podido recorrer libremente desde que el Universo se formó). Este modelo usa la métrica espacial de Friedmann-Lemaître-Robertson-Walker (FLRW). Además, el modelo nos dice cómo era el Universo en el pasado. Así por ejemplo sabemos que el Universo hace unos 14.000 millones de años estaba en un estado singular de *infinita* densidad y temperatura. En ese momento las leyes fundamentales de la física dejan de funcionar como nosotros sabemos. Desde esa singularidad hasta aproximadamente 10^{-43} segundos después la física del universo es poco conocida (especialmente porque las condiciones de muy altas energías no se han podido reproducir todavía en un laboratorio). A partir de este tiempo conocemos mejor el comportamiento del Universo. La temperatura, presión y densidad eran muy altas. Según la *inflación estandar*, el Universo se expandió muy rápidamente hasta 10^{-35} segundos después del Big Bang. Al final de la inflación el Universo estaba formado por un plasma de quarks y otras partículas fundamentales. Hacia los 10^{-5} segundos después del Big Bang, se formaron los primeros bariones, y después, cuando la temperatura promedio descendió hasta los 3000 K, 400.000 años después del Big Bang, la radiación y la materia se desacoplaron, apareciendo la RFCM. Las fluctuaciones presentes en el momento que la materia y la radiación se desacoplaron quedaron presentes en la RFCM. Dado que sus escalas características son mayores que el tamaño del horizonte en aquel momento, no pudieron formarse de forma causal, y por tanto deben introducirse como parte de las condiciones iniciales. La inflación estándar es capaz de resolver de forma dinámica este problema [2, 70, 105, 106], y sus predicciones se ajustan muy bien con las observaciones de las anisotropías de la RFCM [97].

Las anisotropías en la RFCM que observamos actualmente se han formado por diferentes procesos físicos en distintos lugares y en distintos momentos. Se clasifican en primarias y secundarias dependiendo si se formaron antes o durante el desacoplo de fotones y materia bariónica (primarias) o después (secundarias).

Las anisotropías primarias se forman en un contexto en el que la radiación y la materia están interaccionando y en equilibrio térmico. Así la presión de la radiación tiende a borrar anisotropías mientras que la gravedad de los bariones tiende a ampliar las anisotropías. Estos dos efectos crean oscilaciones acústicas en el plasma de bariones y fotones que dejan una huella característica en el espectro de potencias en forma de oscilaciones. En la gran escala, domina el efecto Sachs-Wolfe [145] debido a variaciones en el potencial gravitatorio. En la pequeña escala dominan efectos de amortiguamiento que se producen en el momento en que el plasma de materia y radiación empieza a desaparecer. Este efecto contribuye a la supresión de anisotropías a pequeña escala [152].

Las anisotropías secundarias se formaron después de que la radiación y la materia dejaron de estar en equilibrio térmico (desacoplo). Se deben a la interacción de los fotones de la RFCM con la materia neutra e ionizada. La interacción con materia ionizada tiende a reducir las anisotropías y además genera polarización. Además el gas caliente atrapado entre cúmulos de galaxias contiene electrones libres que interaccionan con los fotones de la RFCM. Este efecto es conocido como efecto de Sunyaev-Zel'dovich. Hay dos variantes de este efecto, el cinemático y el térmico. El primero es debido a la velocidad peculiar del cúmulo y el segundo por la temperatura del gas. Finalmente hay interacciones de los fotones con los pozos de potencial gravitatorio formados por la distribución a gran escala de la materia como son el efecto Sachs-Wolfe integrado, el efecto Rees-Sciama, el efecto lente gravitatoria, etc.

8.1.2 Contaminantes

La señal de RFCM llega contaminada con componentes que no tienen un origen cosmológico. Las fuentes de esta contaminación son la Via Láctea y las emisiones provenientes de otras galaxias. Los contaminantes debidos a la Galaxia suelen ser extensos y dominan sobre todo en la zona del plano galáctico. Los contaminantes extragalácticos suelen estar muy localizados en las posiciones de galaxias o grupos de galaxias vecinos. Hay una ventana de frecuencias entre los 30 GHz y los 100 GHz donde los contaminantes son menos importantes que la RFCM.

Los contaminantes debidos a la Galaxia más importantes son la radiación sincrotrón, la radiación *free-free* y la radiación debida al polvo. El espectro de estos contaminantes viene caracterizado por una dependencia con la frecuencia en forma de ley de potencias, $I(\nu) \propto \nu^{\beta}$, siendo β un índice espectral. La radiación sincrotrón se produce por la aceleración de partículas cargadas que se mueven a velocidades ultrarrelativistas dentro de un campo magnético. Su espectro tiene un índice espectral entre -3.1 y -2.6. La radiación *free-free* se produce por la interacción entre electrones e iones. Es dominante a frecuencias intermedias. Los granos de polvo que hay en el espacio interestelar, cuyo tamaño característico es de varias micras, absorben radiación ultravioleta y la reemiten en las bandas infrarroja y microondas, por lo que es dominante a altas frecuencias ($\gtrsim 100$ GHz). Su índice varía entre 1.5 y 2.5.

Los contaminantes extragalácticos son los cuásares, galaxias y núcleos galácticos activos. Su señal nos llega como fuentes puntuales, pues están muy lejos. Las máscaras para los datos de WMAP enmascaran las fuentes puntuales más brillantes.

8.1.3 Fuentes primordiales de no-Gaussianidad y la RFCM

Durante el período inflacionario el Universo temprano se expandió de forma exponencial. Como se puede ver en el capítulo 1, esta expansión acelerada sólo se puede producir en una situación en la que hay un medio con presión negativa [108]. Sin embargo, la física de las partículas que pueden dar una presión promedio negativa es poco conocida. La inflación resuelve varios problemas no resueltos de la teoría del Big Bang, como son el problema de horizonte, la falta de curvatura del Universo, la falta de monopolos magnéticos así como la generación de inhomogeneidades que dan lugar a las estructuras que se observan en el Universo actual.

El problema del *horizonte* surge cuando se observa que la distribución de materia en escalas muy grandes (del orden de 100 Mpc o más) es muy homogénea e isótropa. Lo mismo sucede con las anisotropías de la RFCM. La pregunta surge dado que el tamaño del Universo es tan grande, hay regiones separadas por distancias tan grandes que ni siquiera la luz ha podido recorrerlas a lo largo de los 14.000 millones de años de edad del Universo. Y sin embargo esas regiones son demasiado parecidas, lo cual sugiere un cierto contacto en el pasado. Una forma de resolver este problema es que en algún momento de la historia del Universo, el factor de escala $a(t)$ que caracteriza la expansión, haya sufrido una aceleración $d^2a/dt^2 > 0$. En ese caso, se puede demostrar que el Universo sufrió una expansión tal que regiones del Universo que inicialmente estaban en contacto causal, dejaron de estarlo por la rápida expansión.

El problema de la falta de *curvatura* del Universo surge a partir de las observaciones que indican que la densidad promedio es muy próxima a la llamada densidad crítica $\rho_c = 3H/8\pi G$, donde $H = \dot{a}/a$ es el parámetro de Hubble y G la constante de gravitación universal. A partir de las ecuaciones de Friedmann se puede ver que esto implica que la densidad del universo en el pasado aún era más cercana a la densidad crítica, o lo que es equivalente, la geometría del Universo era muy aproximadamente plana. Estas condiciones iniciales son demasiado especiales y por tanto, *a priori*, parecen muy improbables. Al igual que en el caso anterior, una gran expansión del Universo puede llevarnos de forma dinámica a los valores de la densidad actuales.

Algunas teorías de física de partículas indican que en situaciones de altas temperatura y densidad como las que sufrió el Universo primitivo tuvieron que generarse *monopolos magnéticos* estables y muy energéticos, que no han sido observados en la naturaleza. La inflación resuelve esta cuestión dado que una situación de expansión inflacionaria puede haber diluido la densidad de esas partículas a niveles fuera del rango de observación.

Finalmente, *la formación de inhomogeneidades* también se resuelve mediante la inflación. Las escalas de las fluctuaciones cuánticas de los campos presentes en los primeros momentos del Universo se amplían por la expansión, y cuando dichas fluctuaciones alcanzan tamaños mayores que el horizonte se fosilizan, dejan de fluctuar rápidamente y dan lugar a las semillas de las estructuras e inhomogeneidades que podemos ver actualmente.

Desde el punto de vista microscópico, la inflación puede ser generada por una o más partículas con *spin* 0, caracterizadas a través de los campos escalares. Estos campos dan una presión promedio que es negativa, propiedad que es necesaria para producir una expansión acelerada. La inflación estándar asume la existencia de un único campo escalar llamado inflatón que da lugar a la expansión inflacionaria. Por las propiedades del inflatón (ver capítulo 1) se sabe que la presión negativa se alcanza cuando el inflatón tiene más energía potencial que cinética. Esta situación se puede dar por ejemplo en un mínimo local del potencial del inflatón [70], aunque diversos cálculos [71, 76] mostraron que este tipo de falsos mínimos eran inviables para generar inflación acorde con las observaciones. Los modelos más conocidos que sí funcionan son aquellos en los que el inflatón sufre una transición en el potencial hacia un mínimo absoluto de forma lenta, de modo que se sigue satisfacciendo la condición de presión negativa [2, 105]. Al final de la inflación, cuando el inflatón alcanza el mínimo, se produce un proceso de termalización durante el cual el inflatón es transformado en otras partículas y radiación que llenan el Universo. Las fluctuaciones presentes en el inflatón, ampliadas por el efecto de la expansión dan lugar a las inhomogeneidades que quedan reflejadas en la materia y la radiación en forma de anisotropías. En el caso de la inflación estándar, el inflatón está en su estado fundamental de acuerdo con la teoría cuántica de campos, lo que implica que las fluctuaciones tienen una distribución de probabilidad de tipo Gaussiano. Esta distribución de probabilidad se transmite de las inhomogeneidades a las anisotropías de la RFCM. Así, al estudiar la distribución estadística de las anisotropías de la RFCM, estamos estudiando la inflación, y por tanto podemos descartar o confirmar los modelos inflacionarios que sean compatibles con las observaciones.

Hay diferentes modelos de inflación que predicen la presencia de desviaciones con respecto a la distribución Gaussiana. El nivel de no -Gaussianidad se puede caracterizar fenomenológicamente a través del parámetro de acoplamiento no-lineal f_{nl} [13]. Así por ejemplo, la propia inflación estándar tiene ligeras desviaciones no-Gaussianas cuando se tienen en cuenta elementos perturbativos de segundo orden. Hay varios modelos inflacionarios alternativos al estándar que predicen desviaciones no-Gaussianas en las fluctuaciones. Podemos mencionar el modelo de curvatón [115], el modelo de termalización o recalentamiento in-homogéneo [55], los modelos con varios campos o inflación híbrida [107], o modelos más exóticos como la inflación templada [18], la inflación fantasma [8] o la inflación de tipo DBI [153] todas ellas descritas en detalle en Bartolo et al. [13]. Además de la inflación, hay otros modelos que predicen no-Gaussianidad que puede ser detectada en las anisotropías de la RFCM.

Los modelos que tienen *defectos topológicos* también predicen no-Gaussianidad en la RFCM. Las teorías de física de altas energías que hablan de la unificación de las fuerzas fundamentales en el Universo primitivo predicen la producción de defectos topológicos durante las rupturas de simetrías. Estos defectos, que pueden ser de diversos tipos según la clase de transición, son fenómenos extraordinariamente energéticos que dejan sus huellas en la RFCM. En Cruz et al. [41] se propone que una mancha fría no-Gaussiana detectada en los datos de WMAP es compatible con los efectos de un tipo de defecto topológico llamado textura.

También la *geometría y la topología* del Universo afectan a la RFCM. Ligeras desviaciones de la métrica de Friedmann-Roberston-Walker o topologías no triviales pueden dejar huellas no-Gaussianas en la RFCM o afectar a la isotropía del Universo [122]. Luminet et al. [113] proponen una topología con forma de dodecaedro para explicar unas anomalías encontradas en el espectro de potencias de WMAP en los bajos multipolos ℓ.

Los *campos magnéticos primordiales* también pueden generar no-Gaussianidad [54]. La turbulencia magnética de tipo Alfvén generada durante la época de recombinación por un campo magnético isótropo y homogéneo induce correlación en los multipolos $a_{\ell m}$ con $\Delta\ell = 2$. Este efecto ha sido estudiado por Naselsky et al. [133] en los datos de WMAP sin encontrar contribuciones significativas.

8.1.4 Métodos para analizar las anisotropias de la RFCM

Desde la llegada de experimentos de gran precisión para el estudio de la RFCM, se han aplicado diferentes técnicas matemáticas para caracterizar la distribución estadística de las anisotropías de la RFCM. Hay herramientas que son más eficientes para ciertos tipos de no-Gaussianidad que para otros. En esta tesis se han usado herramientas basadas en el espacio real, como un tipo particular de prueba de bondad en el ajuste y los funcionales de Minkowski (capítulos 2 y

3), y otras basadas en el espacio de armónicos esféricos como las ondículas y el biespectro (capítulos 4, 5 y 6).

Prueba continua de bondad en el ajuste

En los métodos basados en la bondad en el ajuste continua, se trata de analizar si un conjunto de números aleatorios $\{y_i\}_{i=1}^{i=n}$ se ajustan a una función de densidad de probabilidad $f(y,\theta)$. La cantidad θ, que puede ser un número real o un vector, sirve para parametrizar de forma continua el espacio de funciones densidad de probabilidad. En esta prueba se trata de verificar una hipótesis nula, $H_0 : \{\theta = 0\}$ frente a la hipótesis alternativa, $K : \{\theta \neq 0\}$.

Dentro de todas las posibilidades que tenemos para la función $f(y,\theta)$, podemos considerar la función densidad alternativa de orden k definida como [141, 142]

$$g_k(y,\theta) = C(\theta)\exp\left[\sum_{i=1}^{k}\theta_i h_i(y)\right] f(y) \tag{8.1.1}$$

donde θ es un conjunto de k parámetros que recorren de forma continua el espacio de funciones, $C(\theta)$ es una constante de normalización, $f(y)$ es la función densidad de la hipótesis nula y $h_i(y)$ es un un conjunto completo de funciones ortonormales[1] con $f(y)$.

Para probar si los números de partida cumplen la hipótesis nula, se puede usar el estadístico S_k definido como [3]

$$S_k = \sum_{i=1}^{k} U_i^2 \ , \tag{8.1.2}$$

siendo los estadísticos U_i

$$U_i = \sum_{j=1}^{n} \frac{h_i(y_j)}{\sqrt{n}}. \tag{8.1.3}$$

En el caso que los números y_i sean Gaussianos, se puede demostrar que los estadísticos U_i^2 se comportan siguiendo la distribución χ^2 con 1 grado de libertad.

En el capítulo 2 se usa este método para analizar las anisotropías de la RFCM a través de una descomposición de señal-ruido, mediante un método conocido como *automodos señal-ruido*, usado por primera vez por Bond [21] y aplicado por ejemplo por Aliaga et al. [3, 4], Cayón et al. [29]. Con este método se transforman los datos $\vec{d}$, a través de la matriz de correlación señal-ruido A definida en

[1] $\int_{-\infty}^{\infty} h_i(y) f(y) h_j(y)\, dy = \delta_{ij}$

la ecuación 1.4.7, en unas cantidades y_i independientes y con una señal-ruido conocida. Estos números y_i se analizan con la prueba continua de bondad en el ajuste descrita anteriormente para comprobar la Gaussianidad de los datos.

Los funcionales de Minkowski

Los funcionales de Minkowski son un tipo de descriptores morfológicos que sirven para describir funciones definidas en un espacio como pueden ser las anisotropías de la RFCM en la esfera [67, 127, 149]. En el caso de una función definida en la esfera, como por ejemplo las anisotropías $\Delta T(\vec{n})$, hay tres funcionales de Minkowski para un determinado umbral ν. Considerando el conjunto de puntos Q_ν tales que $\Delta T(\vec{n})/\sigma > \nu$, donde σ es la dispersión del mapa, los funcionales son:

- El área total $A(\nu)$ del conjunto Q_ν
- El perímetro $C(\nu)$ del conjunto Q_ν
- El género $G(\nu)$, definido como el número de manchas calientes (conjunto compacto de puntos con $\Delta T(\vec{n})/\sigma > \nu$) menos el número de manchas frías (conjunto compacto de puntos con $\Delta T(\vec{n})/\sigma < \nu$)

En el caso de que las anisotropías sean Gaussianas, se pueden calcular los funcionales de forma analítica [149]

$$\begin{aligned}
\langle A(\nu)\rangle &= \frac{1}{2}\left(1-\frac{2}{\sqrt{\pi}}\int_0^{\nu/\sqrt{2}} exp(-t^2)dt\right) \\
\langle C(\nu)\rangle &= \frac{\sqrt{\tau}}{8} exp\left(-\frac{\nu^2}{2}\right) \\
\langle G(\nu)\rangle &= \frac{\tau}{(2\pi)^{3/2}}\,\nu\, exp\left(-\frac{\nu^2}{2}\right),
\end{aligned} \tag{8.1.4}$$

donde $\tau = \sum_{\ell=1}^{\ell_{max}}(2\ell+1)C_\ell\ell(\ell+1)/2$ para un espectro de potencias C_ℓ determinado.

Este test consiste en evaluar los funcionales de Minkowski de los datos para un conjunto determinado de umbrales n_{th}. La prueba de Gaussianidad se hace comparando el valor de los funcionales para los datos con el valor esperado de los funcionales para el caso Gaussiano, a través de un test χ^2 (ecuaciones 1.4.11

y 1.4.17). De forma similar se pueden usar los funcionales para acotar el valor del parámetro f_{nl} (ecuaciones 1.4.15 y 1.4.18).

La ondícula de sombrero mejicano en la esfera

Las ondículas son herramientas útiles para analizar la Gaussianidad de la RFCM. Mediante las ondículas podemos descomponer funciones como combinación de ondículas de forma análoga a la transformada de Fourier. Mientras que en el análisis armónico la transformada sólo está localizada en el espacio armónico, en el caso de las ondículas tenemos propiedades de ambos espacios. En esta tesis hemos usado un tipo particular de ondícula de sombrero mejicano adaptada a la esfera (spherical Mexican hat wavelet, SMHW) a través de una proyección estereográfica [6, 120]. Ejemplos de la aplicación de las ondículas a la RFCM son Barreiro et al. [10], Cayón et al. [27, 28] usando los datos de COBE y Cabella et al. [25], Cayón et al. [30], Cruz et al. [38, 40], McEwen et al. [125], Mukherjee & Wang [132], Vielva et al. [165, 166], Wiaux et al. [172] para los datos de WMAP. Para una función $f(\mathbf{n})$ evaluada en la esfera y una familia de ondículas continuas $\Psi(\mathbf{n};\mathbf{b},R)$ como la SMHW podemos definir la transformada de $f(\mathbf{n})$ como

$$w(\mathbf{b};R) = \int d\mathbf{n} f(\mathbf{n})\Psi(\mathbf{n};\mathbf{b},R) \tag{8.1.5}$$

donde $\mathbf{b}$ es la posición donde la ondícula es evaluada y R es la escala característica. Para la SMHW la función ondícula es

$$\Psi_S(\theta;R) = \frac{1}{\sqrt{2\pi}N(R)}\left[1+\left(\frac{y}{2}\right)^2\right]^2\left[2-\left(\frac{y}{R}\right)^2\right]e^{-y^2/2R^2} \tag{8.1.6}$$

donde

$$N(R) = R\left(1+\frac{R^2}{2}+\frac{R^4}{4}\right)^{1/2} \tag{8.1.7}$$

y

$$y = 2\tan\left(\frac{\theta}{2}\right). \tag{8.1.8}$$

Nuestro análisis estadístico con ondículas consiste en evaluar los mapas de coeficientes de la ecuación 8.1.5 para varias escalas angulares, de forma que se pueda resaltar la no-Gaussianidad dominante en cada escala angular. Esos coeficientes son combinados a través de diferentes estadísticos para buscar desviaciones no-Gaussianas y acotar el parámetro f_{nl} (ver por ejemplo los capítulos 4, 5 y 6).

El biespectro

El biespectro es una de las herramientas estadísticas más usadas para la búsqueda de no-Gaussianidad en las anisotropías de la RFCM [36, 93, 94, 95, 97, 155, 156, 173]. Es una cantidad de tercer orden definida a partir de los coeficientes $a_{\ell m}$ de las anisotropías de la RFCM:

$$B^{m_1 m_2 m_3}_{\ell_1 \ell_2 \ell_3} \equiv \langle a_{\ell_1 m_1} a_{\ell_2 m_2} a_{\ell_3 m_3} \rangle. \tag{8.1.9}$$

En términos prácticos, es más útil usar el biespectro promediado $B_{\ell_1 \ell_2 \ell_3}$ definido como

$$B_{\ell_1 \ell_2 \ell_3} \equiv \sum_{m_1 m_2 m_3} \begin{pmatrix} l_1 & l_2 & l_3 \\ m_1 & m_2 & m_3 \end{pmatrix} B^{m_1 m_2 m_3}_{\ell_1 \ell_2 \ell_3}, \tag{8.1.10}$$

o en términos del biespectro reducido $b_{\ell_1 \ell_2 \ell_3}$ que se define a través de la expresión

$$B_{\ell_1 \ell_2 \ell_3} \equiv \begin{pmatrix} l_1 & l_2 & l_3 \\ 0 & 0 & 0 \end{pmatrix} \sqrt{\frac{(2\ell_1+1)(2\ell_2+1)(2\ell_3+1)}{4\pi}} b_{\ell_1 \ell_2 \ell_3} \tag{8.1.11}$$

Usando la función de transferencia $g_{T\ell}(k)$ que relaciona las anisotropías de la RFCM con el potencial gravitatorio primordial (ecuación 1.4.26) podemos escribir el biespectro reducido como

$$\begin{aligned} b_{\ell_1 \ell_2 \ell_3} = \left(\frac{2}{\pi}\right)^3 \int drdk_1dk_2dk_3 r^2 (k_1k_2k_3)^2 B_\Phi(k_1,k_2,k_3) \times \\ \times g_{T\ell_1}(k_1) g_{T\ell_2}(k_2) g_{T\ell_3}(k_3) j_{\ell_1}(k_1r_1) j_{\ell_2}(k_2r_2) j_{\ell_3}(k_3r_3) \end{aligned} \tag{8.1.12}$$

donde $B_\Phi(k_1,k_2,k_3)$ es el biespectro primordial [61] definido como

$$\langle \Phi(\mathbf{k_1})\Phi(\mathbf{k_2})\Phi(\mathbf{k_3}) \rangle = (2\pi)^3 B_\Phi(k_1,k_2,k_3)\delta(\mathbf{k_1}+\mathbf{k_2}+\mathbf{k_3}). \tag{8.1.13}$$

La función $B_\Phi(k_1,k_2,k_3)$ depende del tipo de modelo no-Gaussiano que se quiera analizar. En Fergusson & Shellard [61] se calcula el biespectro para diferentes escenarios, entre ellos los más conocidos: f_{nl} local y equilateral.

El biespectro es una herramienta útil para acotar el parámetro f_{nl} en cualquiera de sus versiones. Una forma de hacerlo es a través de un test χ^2 asumiendo que no hay correlaciones entre los distintos multipolos ℓ [93]. En ese caso, se puede calcular el error en f_{nl} como

$$\left(\frac{N}{S}\right)_{f_{nl}} \equiv \frac{\sigma(f_{nl})}{f_{nl}} = \frac{1}{\sqrt{F}}, \tag{8.1.14}$$

donde F es la matriz de Fisher para el biespectro (ecuación 1.4.37).

Hay otras formas de combinar el biespectro computacionalmente de manera más eficiente [96] que han sido aplicadas a los datos de WMAP con muy buenos resultados [97, 156, 173].

Otras formas de estudiar la Gaussianidad

Además de los métodos descritos anteriormente que han sido usados en esta tesis, hay otras formas de probar la no-Gaussianidad de la RFCM. Esos métodos operan en el espacio real, el espacio de armónicos esféricos o el espacio de coeficientes de ondículas. Habitualmente la forma de trabajar con ellos es calculando su valor esperado a través de simulaciones o de forma analítica y posteriormente comparando con los valores correspondientes a los datos reales obtenidos por un experimento.

La forma más sencilla de buscar huellas no-Gaussianas en la RFCM es a través de la *skewness* S y la *kurtosis* K del campo de anisotropías [114, 130], que están relacionadas con los momentos de tercer y cuarto orden.

Otra forma de buscar no-Gaussianidad es a través de las correlaciones angulares de N puntos [56, 92] o la distribución de probabilidad de N puntos [168].

Una forma diferente de probar la Gaussianidad es a través de cantidades escalares construidas a partir de las primeras y segundas derivadas del campo Gaussiano [58, 128]. Estos escalares son bastante eficientes para un tipo de no-Gaussianidad como la generada por la expansión de Edgeworth [129].

Finalmente podemos mencionar diferentes tipos de ondículas además de la ya descrita SMHW. Por ejemplo las ondículas planas [131, 136], la ondícula de Haar en la esfera [10], ondículas direccionales en la esfera [125], ondículas direccionales [166, 172], etc.

8.1.5 Anomalías detectadas en WMAP

Algunos de los análisis estadísticos que se han hecho usando los datos de WMAP indican la presencia de posibles asimetrías así como desviaciones Gaussianas. Podemos mencionar el alineamiento y las simetrías en los multipolos bajos [34, 35, 101, 135], las asimetrías Norte-Sur [60], correlaciones en las fases [31, 33], valores inesperados para la varianza de los mapas [130] así como una mancha fría no-Gaussiana localizada en el hemisferio sur de la Galaxia [38, 39, 40, 41, 42, 43, 165].

De todas ellas, las más conocidas y estudiadas son el alineamiento de los multipolos bajos y las asimetrías así como la mancha no-Gaussiana del sur galáctico. Se han barajado varias explicaciones para la mancha, como por ejemplo un gran vacío o una textura cósmica. Con respecto al resto, principalmente localizadas en el plano eclíptico se piensa que podrían estár relacionadas con efectos sistemáticos desconocidos.

8.2 Capítulo 2

En este capítulo hacemos un análisis estadístico de las anisotropías de la RFCM medidas por el experimento Archeops instalado en un globo estratosférico. Los datos analizados se corresponden a un bolómetro que opera a 143 GHz. En este análisis hemos usado mapas a baja resolución (2 grados) considerando sólo una fracción del hemisferio norte galáctico correspondiente al 16% de todo el cielo. Como herramientas estadísticas hemos usado la prueba de bondad en el ajuste descrita anteriormente así como los funcionales de Minkowski. Para ambos análisis se hicieron simulaciones Gaussianas que contienen señal de la RFCM así como ruido instrumental. Se usaron dos tipos de algoritmos para producir los mapas (coadición y *Mirage*). Ambos tipos de mapas son compatibles con Gaussianidad, lo cual es compatible con las predicciones de la inflación estándar. También hemos estudiado la contaminación por el polvo de la Galaxia así como por la atmósfera de la Tierra, excluyendo una contaminación por encima del 7.8% con un nivel de confianza del 90%. Finalmente hemos acotado el parámetro f_{nl} local para la aproximación de Sachs-Wolfe a gran escala. Los resultados indican $f_{nl} = 200\ ^{+1100}_{-800}$ con un nivel de confianza del 95%. Por comparación hemos analizado los datos de WMAP en la misma zona del cielo y con la misma resolución encontrando resultados compatibles.

8.3 Capítulo 3

En este capítulo presentamos un análisis de Gaussianidad de las anisotropías de la RFCM a alta resolución medidas por el experimento Archeops. Mediante este análisis acotamos el parámetro de acoplamiento no-lineal f_{nl} usando un modelo no-Gaussiano bien motivado. Hemos usado los datos del bolómetro menos afectado por sistemáticos a 143 GHz. Para caracterizar el ruido, hemos usado los datos de un segundo bolómetro a 143 GHz. Las escalas angulares consideradas varían desde los 27 minutos de arco hasta los 1.8 grados. Hemos considerado una fracción del 21% del cielo, incluyendo zonas del norte y del sur de la Galaxia (cortando las zonas con menos de 15 grados de latitud galáctica). Para este análisis se han usado los funcionales de Minkowski evaluados en la esfera a diferentes umbrales. Con estas cantidades hemos construido un estadístico χ^2 que hemos usado para analizar la Gaussianidad de los datos así como para acotar f_{nl}. El algoritmo para generar los mapas es el *Mirage*, mencionado en el capítulo 2. Las simulaciones usadas en este análisis contienen una parte de señal Gaussiana y no-Gaussiana así como ruido instrumental Gaussiano. Los datos de Archeops a alta resolución son compatibles con Gaussianidad después de quitar algunos pixeles contaminados por el ruido. El parámetro de acoplamiento no-lineal queda acotado con estos datos $f_{nl} = 70^{+590}_{-400}$ con un nivel de confianza del 68% y $f_{nl} = 70^{+1075}_{-920}$ con un nivel de confianza del 95%, usando simulaciones no-Gaussianas realistas.

8.4 Capítulo 4

En este capítulo desarrollamos un análisis de Gaussianidad de los datos del quinto año de observación del satélite WMAP. Hemos usado un conjunto de estimadores de tercer orden basados en los coeficientes de la ondícula de sombrero mejicano esférica (SMHW por sus siglas en inglés). Además acotamos el parámetro de acoplamiento no-lineal f_{nl} usando simulaciones no-Gaussianas bien motivadas. Los mapas analizados se corresponden con las bandas Q, V y W de WMAP a una resolución angular de 6.9 minutos de arco. Hemos considerado la máscara *KQ*75 que recomienda el equipo de WMAP para los análisis cosmológicos, que excluye un 28% del cielo. Los mapas de coeficientes de la SMHW son evaluados en 10 escalas angulares diferentes entre los 6.9 y los 150 minutos de arco. Los estadísticos de tercer orden basados en esos coeficientes se usan para construir un estadístico χ^2 para analizar la Gaussianidad así como imponer cotas a f_{nl}. Los resultados indican que los datos de WMAP son compatibles con Gaussianidad y el parámetro f_{nl} queda acotado $-8 < f_{nl} < +111$ con un nivel de confianza del 95% para el mapa combinado V+W. Este valor ha sido corregido por la contaminación debida a la presencia de fuentes puntuales no enmascaradas, que añaden una contribución positiva de $\Delta f_{nl} = 3 \pm 5$ para el mapa combinado V+W. Estos resultados son muy parecidos a los obtenidos por Komatsu et al. [97] usando el biespectro.

8.5 Capítulo 5

En este capítulo presentamos nuevas cotas al parámetro de acoplamiento no-lineal f_{nl} usando las anisotropías de la RFCM medidas por WMAP. Este capítulo es una continuación del capítulo anterior donde hemos usado varios estadísticos de tercer orden basados en la ondícula de sombrero mejicano esférica. En particular, se usan todos los posibles estadísticos de tercer orden que se pueden generar a partir de los mapas de coeficientes de ondículas para 12 escalas angulares diferentes. Esas escalas están distribuidas logarítmicamente entre los 6.9 y los 500 minutos de arco. El resultado del análisis indica que $-18 < f_{nl} < +80$ con un nivel de confianza del 95% para el mapa combinado V+W. Este valor ha sido corregido por la contribución de las fuentes puntuales que añaden $\Delta f_{nl} = 6 \pm 5$. Nuestro resultado excluye al 99% el valor f_{nl} =87 encontrado por Yadav & Wandelt [173]. Hemos acotado f_{nl} para las bandas Q, V y W de WMAP por separado, encontrando que f_{nl} es compatible con cero con un nivel de confianza del 95% para Q y V pero no para W. Hemos hecho varios análisis para entender por qué se desvía de cero el valor de f_{nl} del canal W. Los resultados indican que posibles sistemáticos presentes en los radiómetros de W pueden explicar esta desviación. Finalmente hemos acotado f_{nl} para las regiones norte y sur de la Galaxia. El resultado indica que el valor de f_{nl} que mejor ajusta los datos de la zona norte es compatible con el valor de f_{nl} que mejor ajusta los datos de la zona sur.

8.6 Capítulo 6

En este capítulo estudiamos la eficiencia de la ondícula de sombrero mejicano esférica como detector de no-Gaussianidad primordial a través de las anisotropías de la RFCM. Para ello hemos definido estadísticos de tercer orden basados en los mapas de coeficientes de la ondícula evaluados en diferentes escalas. Hemos encontrado una relación analítica entre estos estadísticos y el biespectro para el modelo de f_{nl} local [93]. Hemos comparado los valores analíticos de estos estadísticos con los valores obtenidos con simulaciones no-Gaussianas para un experimento ideal sin contaminación instrumental y sin máscaras.

Finalmente estudiamos la potencia del método para acotar f_{nl}, es decir el valor de $\sigma(f_{nl})$ y comparamos con la matriz de Fisher para el biespectro en el mismo experimento ideal. Los resultados indican que el método basado en ondículas es tan eficiente como el biespectro como detector óptimo de no-Gaussianidad primordial del tipo local.

8.7 Conclusiones

La búsqueda de desviaciones no-Gaussianas en las anisotropías de la RFCM es una de las cuestiones más importantes de la cosmología moderna dado que puede servir para distinguir posibles escenarios del Universo primitivo y también para estudiar fuentes secundarias de no-Gaussianidad. La inflación estándar predice que las fluctuaciones primordiales generadas durante la inflación presentes en las anisotropías de la RFCM son Gaussianas. En la introducción hemos descrito algunos de los modelos inflacionarios alternativos que predicen no-Gaussianidad. En esta tesis hemos presentado varios análisis de Gaussianidad para las anisotropías de la RFCM. Hemos analizado los datos medidos por el experimento Archeops usando un tipo especial de prueba de bondad en el ajuste así como los funcionales de Minkowski. Hemos acotado los niveles de contaminación atmosférica y hemos acotado f_{nl}. También hemos analizado los datos del experimento WMAP usando ondículas. En un primer análisis hemos acotado el parámetro f_{nl} encontrando que es compatible con cero y que los resultados son comparables a los obtenidos por el equipo de WMAP. En un segundo análisis más exhaustivo hemos mejorado las cotas de ese parámetro. Finalmente hemos estudiado la eficiencia de las ondículas para detectar f_{nl} así como su dependencia con el biespectro, considerado el detector más eficiente para este tipo de no-Gaussianidad. A continuación pasamos a resumir las conclusiones de cada uno de los capítulos de esta tesis:

8.7.1 Capítulo 2

En este capítulo hemos hecho un análisis de Gaussianidad de los datos de Archeops a baja resolución usando un tipo especial de prueba de bondad en el ajuste y los funcionales de Minkowski.

Hemos encontrado que los estadísticos U_i^2 evaluados para simulaciones Gaussianas de la RFCM se comportan como una distribución χ_1^2 para casos con índices $1 \leq i \leq 4$. Para momentos superiores, $i > 4$ la media de la distribución es $\mu \simeq 1$ pero la dispersión es $\sigma \gtrsim 2$, debido a la propagación de los errores numéricos en los estadísticos.

Analizando los datos de Archeops para los dos tipos de algoritmos que generan los mapas, *coadición* y *Mirage*, hemos encontrado que los datos son compatibles con Gaussianidad. Sólo en el caso de coadición hemos encontrado que U_2^2 llega a valer 8 para un corte de señal-ruido bajo. Aunque la probabilidad de que U_2^2 valga más que 8 para un determinado corte señal-ruido es muy baja (ver la tabla 2.3) la probabilidad de tener U_2^2 mayor que 8 para cualquier corte de señal-ruido es 0.1482. Esto no es despreciable, y por tanto la detección no es significativa. Además, dado que este efecto no aparece en el mapa Mirage, sólo puede ser debido a algún sistematico relacionado con el proceso de generación del mapa. El análisis con los funcionales de Minkowski también indica compatibilidad con Gaussianidad para los datos de Archeops.

En este análisis también hemos acotado la contaminación presente a los 143 GHz. Hemos usado como modelo del polvo galáctico y de la atmósfera terrestre los datos de Archeops a 353 GHz. La contaminación queda acotada a menos del 7.8% con un nivel de confianza del 90%.

Hemos comparado los resultados de Archeops con los datos de WMAP para el primer y el tercer año de observaciones en la misma zona del cielo. Hemos encontrado un máximo en el estadístico U_2^2 para un determinado corte de señal-ruido que no es significativo, y por tanto los datos son también consistentes con Gaussianidad.

Finalmente hemos impuesto cotas al parámetro de acoplamiento no-lineal f_{nl}. Así, tenemos para los datos de Archeops $f_{nl} = 200\ ^{+900}_{-600}$ con un 90% de nivel de confianza y $f_{nl} = 200\ ^{+1100}_{-800}$ con un 95% de nivel de confianza. Usando los datos de WMAP en la misma zona del cielo, encontramos $f_{nl} = 100\ ^{+400}_{-300}$ al 90% de nivel de confianza y $f_{nl} = 100\ ^{+500}_{-400}$ al 95% de nivel de confianza. Estos límites son similares a los que se esperarían para un experimento similar a Archeops con un nivel de ruido parecido a WMAP en el tercer año de observaciones.

8.7.2 Capítulo 3

En este capítulo hemos presentado un análisis de Gaussianidad completo de los datos de Archeops a 143 GHz usando los funcionales de Minkowski. Primero hemos caracterizado el ruido instrumental de Archeops tomando como modelo de ruido la diferencia de los mapas medidos con dos bolómetros distintos, 143K03 y 143K04. En este mapa hemos encontrado algunas desviaciones no-Gaussianas a alta resolución, 27 minutos de arco ($N_{side} = 128$ en la pixelización de HEALPix). Esto se explica porque el número de observaciones por pixel para los pixeles más ruidosos no permite hacer una correcta limpieza de los errores sistemáticos. Un análisis más detallado, llevado a cabo sustrayendo los datos de WMAP al bolómetro $143K03$, indica que los pixeles con un número de observaciones por debajo de 90 no son Gaussianos. Si enmascaramos esos pixeles, el mapa de ruido es compatible con el modelo Gaussiano. Resultados similares se han encontrado para el bolómetro $143K04$ aunque en ese caso el número mínimo de observaciones es mayor, del orden de 150.

Hemos hecho un análisis de Gaussianidad de los datos del bolómetro $143K03$ a baja y alta resolución enmascarando los pixeles más ruidosos. Hemos encontrado que los datos son compatibles con Gaussianidad a $N_{side} = 32$, $N_{side} = 64$, $N_{side} = 128$ y para la combinación $N_{side} = 32, 64$ y la combinación $N_{side} = 32, 64, 128$. Usando simulaciones realistas [109] hemos acotado el parámetro f_{nl}. Las mejores cotas son $f_{nl} = 70^{+590}_{-400}$ y $f_{nl} = 70^{+1075}_{-920}$ con unos niveles de confianza del 68% y 95% respectivamente.

Hemos acotado f_{nl} usando la aproximación de Sachs-Wolfe. En este caso, se obtiene $f_{nl}^{SW} = 25^{+200}_{-150}$ y $f_{nl}^{SW} = 25^{+375}_{-300}$ con unos niveles de confianza del 68% y 95% respectivamente. Nótese que estas cotas son un factor ≈ 3 más pequeñas que las que se presentan en el capítulo 2 donde sólo se usan mapas a baja resolución ($N_{side} = 32$).

Finalmente hemos comparado las simulaciones no-Gaussianas realistas usadas en este capítulo y las correspondientes a la aproximación de Sachs-Wolfe. Incluso para mapas a baja resolución, la aproximación de Sachs-Wolfe sobreestima la no-Gaussianidad de las fluctuaciones de la RFCM y por tanto las cotas al parámetro están artificialmente reducidas por aproximadamente un factor tres.

8.7.3 Capítulo 4

Hemos analizado los datos del quinto año de observaciones de WMAP usando simulaciones Gaussianas y simulaciones no-Gaussianas de las anisotropías de la RFCM mediante un método basado en ondículas. Hemos considerado diferentes combinaciones de los mapas: Q+V+W, V+W, Q, V y W. Para este análisis hemos usado dos tipos de máscaras definidas en la sección 4.2.2. Los momentos de tercer orden definidos en la ecuación 4.2.1 de los datos de WMAP son compatibles con simulaciones Gaussianas (ver la figura 4.2).

A través de un análisis basado en el estadístico χ^2 hemos encontrado que los datos son compatibles con Gaussianidad (ver la figura 4.3). Mediante otro análisis con un estadístico χ^2 hemos acotado el parámetro de acoplamiento no-lineal f_{nl} usando simulaciones no-Gaussianas. El valor de f_{nl} que mejor ajusta los datos es compatible con el encontrado por Komatsu et al. [97] usando el biespectro, mostrando similares intervalos de confianza y la misma dependencia frecuencial.

Finalmente hemos estimado la contribución a f_{nl} debida a fuentes puntuales no resueltas para el mapa V+W usando un modelo simple que tiene fuentes puntuales de intensidad constante ($F_{src} = 0.5$ Jy) y un modelo realista descrito por de Zotti et al. [176]. Hemos encontrado que las fuentes dan una contribución positiva de $\Delta f_{nl} = 11 \pm 4$ para el modelo sencillo y $\Delta f_{nl} = 17 \pm 5$ para el modelo realista. Estos valores son mayores que los encontrados por Komatsu et al. [97] usando el biespectro, y pueden ser explicados por la sensibilidad de las ondículas a las fuentes puntuales. Usando las máscaras menos restrictivas las contribuciones debidas a las fuentes puntuales son $\Delta f_{nl} = 3 \pm 4$ para el modelo sencillo y $\Delta f_{nl} = 3 \pm 5$ para el modelo realista. Estos valores más pequeños se explican porque estas máscaras añaden algunos pixeles que afectan la eficiencia de la máscara a la hora de detectar fuentes puntuales. Teniendo en cuenta la corrección debida a las fuentes puntuales la mejor cota a f_{nl} que tenemos es $-8 < f_{nl} < +111$ con un nivel de confianza del 95%. Es importante resaltar la coincidencia entre los dos estimadores (ondículas y biespectro) dado que están calculados con diferentes combinaciones de los datos y por tanto están afectados por diferentes errores sistemáticos.

8.7.4 Capítulo 5

En este capítulo hemos hecho un análisis de Gaussianidad y hemos acotado el parámetro f_{nl} usando los datos del quinto año de observaciones de WMAP. Para este análisis hemos usado un método optimizado basado en las ondículas. Hemos considerado los mapas combinados V+W, Q, V y W de WMAP a alta resolución. Hemos usado un conjunto de 300 simulaciones no-Gaussianas y varios miles de simulaciones Gaussianas para este análisis. Las escalas angulares consideradas varían entre los 6.9 y los 500 minutos de arco para evaluar todos los posibles momentos de tercer orden (ecuación 5.2.1), usando las máscaras apropiadas.

Los datos analizados son compatibles con simulaciones Gaussianas para los cuatro tipos de mapas considerados (ver tabla 5.1). Hemos impuesto cotas al parámetro f_{nl} local usando simulaciones no-Gaussianas con f_{nl}. Los resultados indican que f_{nl} crece con la frecuencia al pasar de los canales Q al V y al W. Este efecto también aparece en otros análisis como por ejemplo los presentados por Curto et al. [46], Komatsu et al. [97], Yadav & Wandelt [173]. Los resultados son compatibles con cero con un nivel de confianza del 95% para los mapas V+W, Q y V pero no para W que sólo es compatible con cero al 99%. Este valor no se puede explicar por la contribución de las fuentes puntuales dado que su contribución para el mapa W es $\Delta f_{nl} = 1 \pm 2$. Hemos estimado la probabilidad de tener esos valores con simulaciones y los resultados no muestran incompatibilidad entre los diferentes canales. También hemos visto que el valor relativamente grande de f_{nl} obtenido para el canal W puede ser explicado por la presencia de sistemáticos en uno o varios radiómetros de esa banda.

Hemos estimado la contribución de fuentes puntuales al parámetro f_{nl} en el mapa V+W usando el modelo realista de de Zotti et al. [176]. Los resultados son $\Delta f_{nl} = 6 \pm 5$. Si tenemos en cuenta esa contribución, la mejor estimación para f_{nl} es $-18 < f_{nl} < +80$ con un nivel de confianza del 95%. El uso de nuevas escalas y la inclusión de todos los momentos de tercer orden ha proporcionado mejores cotas al parámetro comparadas con las que se obtenían por Curto et al. [46] y en trabajos previos. Nuestra mejor cota es compatible con los resultados presentados por Komatsu et al. [97] y excluye con un nivel de confianza superior al 99% el valor que mejor ajusta a los datos encontrado por Yadav & Wandelt [173].

Finalmente hemos acotado f_{nl} para los hemisferios galácticos norte y sur. Los resultados obtenidos son compatibles con cero al 95% de nivel de confianza y también son compatibles entre sí. Por tanto, no hemos encontrado ninguna asimetría norte-sur para este parámetro.

8.7.5 Capítulo 6

En este capítulo hemos desarrollado un método eficiente basado en ondículas para acotar el parámetro local f_{nl} usando las anisotropías de la RFCM. Hemos encontrado una relación analítica entre los momentos de tercer orden definidos en la ecuación 6.1.2 con f_{nl} y el modelo cosmológico a través del biespectro primordial (ecuación 6.1.13). También hemos encontrado una expresión analítica para evaluar la matriz de covarianza entre todos los estadísticos de tercer orden (ecuación 6.1.17). Suponiendo que los estadísticos de tercer orden se comportan de forma aproximadamente Gaussiana, se puede determinar la varianza f_{nl} a través del método de máxima verosimilitud para el parámetro f_{nl} (sección 6.1.4). Hemos comparado esta varianza con la obtenida para el mismo parámetro usando la matriz de Fisher del biespectro (sección 6.2). Los dos métodos se han aplicado a un experimento ideal con una resolución angular de 6.9 minutos de arco sin ruido instrumental. Teniendo en cuenta la influencia de los errores numéricos debidos a la evaluación de la matriz de covarianza inversa, hemos encontrado que $\sigma(f_{nl}) = 4.20$ usando las ondículas y $\sigma(f_{nl}) = 4.13$ cuando usamos el biespectro. Este resultado indica que las ondículas son tan eficientes como el biespectro para detectar no-Gaussianidad de tipo local. Además de la eficiencia de esta herramienta para detectar f_{nl} tenemos que resaltar que es un estimador estadístico distinto del biespectro, y por tanto puede ser sensible a diferentes sistemáticos presentes en los datos reales. Es por ello por lo que subrayamos la importancia de esta herramienta estadística como una eficiente alternativa para medir f_{nl} en futuros experimentos como Planck.

8.8 Trabajo Futuro

Hay varios formalismos para acotar la no-Gaussianidad primordial usando el biespectro de la RFCM, como por ejemplo el local o el equilateral. Estos modelos han sido caracterizados y comparados con las observaciones en diferentes trabajos [por ejemplo 36, 37, 97]. Otros modelos son descritos en trabajos como

Fergusson & Shellard [61], Jeong & Komatsu [91].

El parámetro f_{nl} local ha sido acotado en esta tesis usando la ondícula de sombrero mejicano. Los análisis descritos en los capítulos 4 y 5 muestran resultados equivalentes a los obtenidos con el biespectro [97]. En el capítulo 6 estudiamos la relación entre las ondículas y el biespectro para el modelo local. Análisis similares pueden ser llevados a cabo con otros tipos de modelos. Esto servirá para estudiar diferentes tipos de no-Gaussianidad primordial y permitirá discriminar distintos modelos inflacionarios alternativos. Otro trabajo a realizar consiste en la búsqueda de no-Gaussianidad presente en el triespectro a través del uso de estadísticos de cuarto orden basados en los coeficientes de la ondícula.

También se pueden mejorar las cotas al parámetro f_{nl} para el caso realista con máscara rellenando las zonas enmascaradas con simulaciones con ligaduras. Esto implicaría que para cada escala habría más área disponible para el análisis y que además se podrían usar escalas más grandes (ver sección 4.2.2). Como consecuencia, las incertidumbres en el parámetro f_{nl} se reducirían y por tanto el método sería aún más eficiente.

References

[1] R. J. Adler, J. D. Bjorken, and J. M. Overduin. "Finite cosmology and a CMB cold spot". arXiv:gr-qc/0602102, February 2006.

[2] A. Albrecht and P. J. Steinhardt. "Cosmology for grand unified theories with radiatively induced symmetry breaking". Physical Review Letters, 48, 1220, April 1982.

[3] A. M. Aliaga, E. Martínez-González, L. Cayón, F. Argüeso, J. L. Sanz, and R. B. Barreiro. "Goodness-of-fit tests of Gaussianity: constraints on the cumulants of the MAXIMA data". New Astronomy Review, 47, 821, November 2003.

[4] A. M. Aliaga, J. A. Rubiño-Martín, E. Martínez-González, R. B. Barreiro, and J. L. Sanz. "Gaussianity of the cosmic microwave background: smooth goodness-of-fit tests applied to interferometric data". MNRAS, 356, 1559, February 2005.

[5] R. A. Alpher, H. Bethe, and G. Gamow. "The Origin of Chemical Elements". Physical Review, 73, 803, April 1948.

[6] J.-P. Antoine and P. Vandergheynst. "Wavelets on the n-sphere and related manifolds". Journal of Mathematical Physics, 39, 3987, August 1998.

[7] F. Argüeso, J. L. Sanz, R. B. Barreiro, D. Herranz, and J. González-Nuevo. "Statistical analysis of undetected point sources in cosmic microwave background maps". MNRAS, 373, 311, November 2006.

[8] N. Arkani-Hamed, P. Creminelli, S. Mukohyama, and M. Zaldarriaga. "Ghost inflation". Journal of Cosmology and Astro-Particle Physics, 4, 1, April 2004.

[9] R. B. Barreiro, J. L. Sanz, E. Martinez-Gonzalez, L. Cayon, and J. Silk. "Peaks in the Cosmic Microwave Backgound: Flat versus Open Models". ApJ, 478, 1, March 1997.

[10] R. B. Barreiro, M. P. Hobson, A. N. Lasenby, A. J. Banday, K. M. Górski, and G. Hinshaw. "Testing the Gaussianity of the COBE DMR data with spherical wavelets". MNRAS, 318, 475, October 2000.

[11] R. B. Barreiro, E. Martínez-González, and J. L. Sanz. "Geometrical estimators as a test of Gaussianity in the cosmic microwave background". MNRAS, 322, 411, April 2001.

[12] R. B. Barreiro, M. P. Hobson, A. J. Banday, A. N. Lasenby, V. Stolyarov, P. Vielva, and K. M. Górski. "Foreground separation using a flexible maximum-entropy algorithm: an application to COBE data". MNRAS, 351, 515, June 2004.

[13] N. Bartolo, E. Komatsu, S. Matarrese, and A. Riotto. "Non-Gaussianity from inflation: theory and observations". Phys. Rep., 402, 103, November 2004.

[14] C. L. Bennett, M. Halpern, G. Hinshaw, N. Jarosik, A. Kogut, M. Limon, S. S. Meyer, L. Page, D. N. Spergel, G. S. Tucker, E. Wollack, E. L. Wright, C. Barnes, M. R. Greason, R. S. Hill, E. Komatsu, M. R. Nolta, N. Odegard, H. V. Peiris, L. Verde, and J. L. Weiland. "First-Year Wilkinson Microwave Anisotropy Probe (WMAP) Observations: Preliminary Maps and Basic Results". ApJS, 148, 1, September 2003.

[15] C. L. Bennett, R. S. Hill, G. Hinshaw, M. R. Nolta, N. Odegard, L. Page, D. N. Spergel, J. L. Weiland, E. L. Wright, M. Halpern, N. Jarosik, A. Kogut, M. Limon, S. S. Meyer, G. S. Tucker, and E. Wollack. "First-Year Wilkinson Microwave Anisotropy Probe (WMAP) Observations: Foreground Emission". ApJS, 148, 97, September 2003.

[16] A. Benoît, P. Ade, A. Amblard, R. Ansari, É. Aubourg, S. Bargot, J. G. Bartlett, J.-P. Bernard, R. S. Bhatia, A. Blanchard, J. J. Bock, A. Boscaleri, F. R. Bouchet, A. Bourrachot, P. Camus, F. Couchot, P. de Bernardis, J. Delabrouille, F.-X. Désert, O. Doré, M. Douspis, L. Dumoulin, X. Dupac, P. Filliatre, P. Fosalba, K. Ganga, F. Gannaway, B. Gautier, M. Giard, Y. Giraud-Héraud, R. Gispert, L. Guglielmi, J.-C. Hamilton, S. Hanany,

S. Henrot-Versillé, J. Kaplan, G. Lagache, J.-M. Lamarre, A. E. Lange, J. F. Macías-Pérez, K. Madet, B. Maffei, C. Magneville, D. P. Marrone, S. Masi, F. Mayet, A. Murphy, F. Naraghi, F. Nati, G. Patanchon, G. Perrin, M. Piat, N. Ponthieu, S. Prunet, J.-L. Puget, C. Renault, C. Rosset, D. Santos, A. Starobinsky, I. Strukov, R. V. Sudiwala, R. Teyssier, M. Tristram, C. Tucker, J.-C. Vanel, D. Vibert, E. Wakui, and D. Yvon. "The cosmic microwave background anisotropy power spectrum measured by Archeops". A&A, 399, L19, March 2003.

[17] A. Benoît, P. Ade, A. Amblard, R. Ansari, É. Aubourg, S. Bargot, J. G. Bartlett, J.-P. Bernard, R. S. Bhatia, A. Blanchard, J. J. Bock, A. Boscaleri, F. R. Bouchet, A. Bourrachot, P. Camus, F. Couchot, P. de Bernardis, J. Delabrouille, F.-X. Désert, O. Doré, M. Douspis, L. Dumoulin, X. Dupac, P. Filliatre, P. Fosalba, K. Ganga, F. Gannaway, B. Gautier, M. Giard, Y. Giraud-Héraud, R. Gispert, L. Guglielmi, J.-C. Hamilton, S. Hanany, S. Henrot-Versillé, J. Kaplan, G. Lagache, J.-M. Lamarre, A. E. Lange, J. F. Macías-Pérez, K. Madet, B. Maffei, C. Magneville, D. P. Marrone, S. Masi, F. Mayet, A. Murphy, F. Naraghi, F. Nati, G. Patanchon, G. Perrin, M. Piat, N. Ponthieu, S. Prunet, J.-L. Puget, C. Renault, C. Rosset, D. Santos, A. Starobinsky, I. Strukov, R. V. Sudiwala, R. Teyssier, M. Tristram, C. Tucker, J.-C. Vanel, D. Vibert, E. Wakui, and D. Yvon. "Cosmological constraints from Archeops". A&A, 399, L25, March 2003.

[18] A. Berera. "Warm Inflation". Physical Review Letters, 75, 3218, October 1995.

[19] P. de Bernardis, P. A. R. Ade, J. J. Bock, J. R. Bond, J. Borrill, A. Boscaleri, K. Coble, B. P. Crill, G. De Gasperis, P. C. Farese, P. G. Ferreira, K. Ganga, M. Giacometti, E. Hivon, V. V. Hristov, A. Iacoangeli, A. H. Jaffe, A. E. Lange, L. Martinis, S. Masi, P. V. Mason, P. D. Mauskopf, A. Melchiorri, L. Miglio, T. Montroy, C. B. Netterfield, E. Pascale, F. Piacentini, D. Pogosyan, S. Prunet, S. Rao, G. Romeo, J. E. Ruhl, F. Scaramuzzi, D. Sforna, and N. Vittorio. "A flat Universe from high-resolution maps of the cosmic microwave background radiation". Nature, 404, 955, April 2000.

[20] F. Bernardeau and J.-P. Uzan. "Non-Gaussianity in multifield inflation". Phys. Rev. D., 66, 103506, November 2002.

[21] J. R. Bond. "Signal-to-Noise Eigenmode Analysis of the Two-Year COBE Maps". Physical Review Letters, 74, 436, May 1995.

[22] H. Bondi and T. Gold. "The Steady-State Theory of the Expanding Universe". MNRAS, 108, 252, 1948.

[23] F. R. Bouchet and R. Gispert. "Foregrounds and CMB experiments I. Semi-analytical estimates of contamination". New Astronomy, 4, 443, September 1999.

[24] W. N. Brandt, C. R. Lawrence, A. C. S. Readhead, J. N. Pakianathan, and T. M. Fiola. "Separation of foreground radiation from cosmic microwave background anisotropy using multifrequency measurements". ApJ, 424, 1, March 1994.

[25] P. Cabella, M. Liguori, F. K. Hansen, D. Marinucci, S. Matarrese, L. Moscardini, and N. Vittorio. "Primordial non-Gaussianity: local curvature method and statistical significance of constraints on f_{NL} from WMAP data". MNRAS, 358, 684, April 2005.

[26] L. Cayón, J. L. Sanz, R. B. Barreiro, E. Martínez-González, P. Vielva, L. Toffolatti, J. Silk, J. M. Diego, and F. Argüeso. "Isotropic wavelets: a powerful tool to extract point sources from cosmic microwave background maps". MNRAS, 315, 757, July 2000.

[27] L. Cayón, J. L. Sanz, E. Martínez-González, A. J. Banday, F. Argüeso, J. E. Gallegos, K. M. Górski, and G. Hinshaw. "Spherical Mexican hat wavelet: an application to detect non-Gaussianity in the COBE-DMR maps". MNRAS, 326, 1243, October 2001.

[28] L. Cayón, E. Martínez-González, F. Argüeso, A. J. Banday, and K. M. Górski. "COBE-DMR constraints on the non-linear coupling parameter: a wavelet based method". MNRAS, 339, 1189, March 2003.

[29] L. Cayón, F. Argüeso, E. Martínez-González, and J. L. Sanz. "Goodness-of-fit tests to study the Gaussianity of the MAXIMA data". MNRAS, 344, 917, September 2003.

[30] L. Cayón, J. Jin, and A. Treaster. "Higher Criticism statistic: detecting and identifying non-Gaussianity in the WMAP first-year data". MNRAS, 362, 826, September 2005.

[31] L.-Y. Chiang, P. D. Naselsky, O. V. Verkhodanov, and M. J. Way. "Non-Gaussianity of the Derived Maps from the First-Year Wilkinson Microwave Anisotropy Probe Data". ApJ, 590, L65, June 2003.

[32] S. E. Church, K. M. Ganga, P. A. R. Ade, W. L. Holzapfel, P. D. Mauskopf, T. M. Wilbanks, and A. E. Lange. "An Upper Limit to Arcminute-Scale Anisotropy in the Cosmic Microwave Background Radiation at 142 GHz". ApJ, 484, 523, July 1997.

[33] P. Coles, P. Dineen, J. Earl, and D. Wright. "Phase correlations in cosmic microwave background temperature maps". MNRAS, 350, 989, May 2004.

[34] C. J. Copi, D. Huterer, and G. D. Starkman.

[35] C. J. Copi, D. Huterer, D. J. Schwarz, and G. D. Starkman. "On the large-angle anomalies of the microwave sky". MNRAS, 367, 79, March 2006.

[36] P. Creminelli, A. Nicolis, L. Senatore, M. Tegmark, and M. Zaldarriaga. "Limits on non-Gaussianities from WMAP data". Journal of Cosmology and Astro-Particle Physics, 5, 4, May 2006.

[37] P. Creminelli, L. Senatore, M. Zaldarriaga, and M. Tegmark. "Limits on f_{NL} parameters from Wilkinson Microwave Anisotropy Probe three-year data". Journal of Cosmology and Astro-Particle Physics, 3, 5, March 2007.

[38] M. Cruz, E. Martínez-González, P. Vielva, and L. Cayón. "Detection of a non-Gaussian spot in WMAP". MNRAS, 356, 29, January 2005.

[39] M. Cruz, M. Tucci, E. Martínez-González, and P. Vielva. "The non-Gaussian cold spot in WilkinsonMicrowaveAnisotropyProbe: significance, morphology and foreground contribution". MNRAS, 369, 57, June 2006.

[40] M. Cruz, L. Cayón, E. Martínez-González, P. Vielva, and J. Jin. "The Non-Gaussian Cold Spot in the 3 Year Wilkinson Microwave Anisotropy Probe Data". ApJ, 655, 11, January 2007.

[41] M. Cruz, N. Turok, P. Vielva, E. Martínez-González, and M. Hobson. "A Cosmic Microwave Background Feature Consistent with a Cosmic Texture". Science, 318, 1612, December 2007.

[42] M. Cruz, E. Martínez-González, P. Vielva, J. M. Diego, M. Hobson, and N. Turok. "The CMB cold spot: texture, cluster or void?" MNRAS, 390, 913, November 2008.

[43] M. Cruz, E. Martinez-Gonzalez, and P. Vielva. "The WMAP cold spot". arXiv:0901.1986, January 2009.

[44] A. Curto, J. Aumont, J. F. Macías-Pérez, E. Martínez-González, R. B. Barreiro, D. Santos, F. X. Désert, and M. Tristram. "Testing Gaussianity on Archeops data". A&A, 474, 23, October 2007.

[45] A. Curto, J. F. Macías-Pérez, E. Martínez-González, R. B. Barreiro, D. Santos, F. K. Hansen, M. Liguori, and S. Matarrese. "Constraints on the non-linear coupling parameter f_{nl} with Archeops data". A&A, 486, 383, August 2008.

[46] A. Curto, E. Martínez-González, P. Mukherjee, R. B. Barreiro, F. K. Hansen, M. Liguori, and S. Matarrese. "Wilkinson Microwave Anisotropy Probe 5-yr constraints on f_{nl} with wavelets". MNRAS, 393, 615, February 2009.

[47] A. Curto, E. Martinez-Gonzalez, and R. B. Barreiro. "Improved constraints on primordial non-Gaussianity for the Wilkinson Microwave Anisotropy Probe 5-yr data". ArXiv:0902.1523, February 2009.

[48] J. Delabrouille, J.-F. Cardoso, and G. Patanchon. "Multidetector multicomponent spectral matching and applications for cosmic microwave background data analysis". MNRAS, 346, 1089, December 2003.

[49] R. H. Dicke, P. J. E. Peebles, P. G. Roll, and D. T. Wilkinson. "Cosmic Black-Body Radiation." ApJ, 142, 414, July 1965.

[50] P. Dineen and P. Coles. "Multivariate Non-Normality in the WMAP 1st Year Data". arXiv:astro-ph/0511802, November 2005.

[51] S. Dodelson. *Modern cosmology*. Academic Press, 2003.

[52] O. Doré, S. Colombi, and F. R. Bouchet. "Probing cosmic microwave background non-Gaussianity using local curvature". MNRAS, 344, 905, September 2003.

[53] M. Dragovan, J. E. Ruhl, G. Novak, S. R. Platt, B. Crone, R. Pernic, and J. B. Peterson. “Anisotropy in the microwave sky at intermediate angular scales”. ApJL, 427, L67–L70, June 1994.

[54] R. Durrer, T. Kahniashvili, and A. Yates. “Microwave background anisotropies from Alfvén waves”. Phys. Rev. D., 58, 123004, December 1998.

[55] G. Dvali, A. Gruzinov, and M. Zaldarriaga. “New mechanism for generating density perturbations from inflation”. Phys. Rev. D., 69, 023505, January 2004.

[56] H. K. Eriksen, A. J. Banday, and K. M. Górski. “The N-point correlation functions of the COBE-DMR maps revisited”. A&A, 395, 409, November 2002.

[57] H. K. Eriksen, F. K. Hansen, A. J. Banday, K. M. Górski, and P. B. Lilje. “Asymmetries in the Cosmic Microwave Background Anisotropy Field”. ApJ, 605, 14, April 2004.

[58] H. K. Eriksen, D. I. Novikov, P. B. Lilje, A. J. Banday, and K. M. Górski. “Testing for Non-Gaussianity in the Wilkinson Microwave Anisotropy Probe Data: Minkowski Functionals and the Length of the Skeleton”. ApJ, 612, 64, September 2004.

[59] H. K. Eriksen, A. J. Banday, K. M. Górski, and P. B. Lilje. “The N-Point Correlation Functions of the First-Year Wilkinson Microwave Anisotropy Probe Sky Maps”. ApJ, 622, 58, March 2005.

[60] H. K. Eriksen, A. J. Banday, K. M. Górski, F. K. Hansen, and P. B. Lilje. “Hemispherical Power Asymmetry in the Third-Year Wilkinson Microwave Anisotropy Probe Sky Maps”. ApJ, 660, L81, May 2007.

[61] J. R. Fergusson and E. P. S. Shellard. “The shape of primordial non-Gaussianity and the CMB bispectrum”. arXiv:0812.3413, December 2008.

[62] D. P. Finkbeiner, M. Davis, and D. J. Schlegel. “Extrapolation of Galactic Dust Emission at 100 Microns to Cosmic Microwave Background Radiation Frequencies Using FIRAS”. ApJ, 524, 867, October 1999.

[63] D. P. Finkbeiner. “A Full-Sky Hα Template for Microwave Foreground Prediction”. ApJS, 146, 407, June 2003.

[64] D. J. Fixsen, E. S. Cheng, J. M. Gales, J. C. Mather, R. A. Shafer, and E. L. Wright. "The Cosmic Microwave Background Spectrum from the Full COBE FIRAS Data Set". ApJ, 473, 576, December 1996.

[65] K. M. Górski, E. Hivon, A. J. Banday, B. D. Wandelt, F. K. Hansen, M. Reinecke, and M. Bartelmann. "HEALPix: A Framework for High-Resolution Discretization and Fast Analysis of Data Distributed on the Sphere". ApJ, 622, 759, April 2005.

[66] A. Gangui, F. Lucchin, S. Matarrese, and S. Mollerach. "The three-point correlation function of the cosmic microwave background in inflationary models". ApJ, 430, 447, August 1994.

[67] J. R. I. Gott, C. Park, R. Juszkiewicz, W. E. Bies, D. P. Bennett, F. R. Bouchet, and A. Stebbins. "Topology of microwave background fluctuations - Theory". ApJ, 352, 1, March 1990.

[68] J. R. Gott, W. N. Colley, C.-G. Park, C. Park, and C. Mugnolo. "Genus topology of the cosmic microwave background from the WMAP 3-year data". MNRAS, 377, 1668, June 2007.

[69] K. Grainge, P. Carreira, K. Cleary, R. D. Davies, R. J. Davis, C. Dickinson, R. Genova-Santos, C. M. Gutiérrez, Y. A. Hafez, M. P. Hobson, M. E. Jones, R. Kneissl, K. Lancaster, A. Lasenby, J. P. Leahy, K. Maisinger, G. G. Pooley, R. Rebolo, J. A. Rubiño-Martin, P. J. Sosa Molina, C. Ödman, B. Rusholme, R. D. E. Saunders, R. Savage, P. F. Scott, A. Slosar, A. C. Taylor, D. Titterington, E. Waldram, R. A. Watson, and A. Wilkinson. "The cosmic microwave background power spectrum out to $\ell = 1400$ measured by the Very Small Array". MNRAS, 341, L23, June 2003.

[70] A. H. Guth. "Inflationary universe: A possible solution to the horizon and flatness problems". Phys. Rev. D, 23, 347, January 1981.

[71] A. H. Guth and E. J. Weinberg. "Could the Universe have recovered from a slow first-order phase transition?" Nuclear Physics B, 212, 321, 1983.

[72] N. W. Halverson, E. M. Leitch, C. Pryke, J. Kovac, J. E. Carlstrom, W. L. Holzapfel, M. Dragovan, J. K. Cartwright, B. S. Mason, S. Padin, T. J. Pearson, A. C. S. Readhead, and M. C. Shepherd. "Degree Angular Scale Interferometer First Results: A Measurement of the Cosmic Microwave Background Angular Power Spectrum". ApJ, 568, 38, March 2002.

[73] S. Hanany, P. Ade, A. Balbi, J. Bock, J. Borrill, A. Boscaleri, P. de Bernardis, P. G. Ferreira, V. V. Hristov, A. H. Jaffe, A. E. Lange, A. T. Lee, P. D. Mauskopf, C. B. Netterfield, S. Oh, E. Pascale, B. Rabii, P. L. Richards, G. F. Smoot, R. Stompor, C. D. Winant, and J. H. P. Wu. "MAXIMA-1: A Measurement of the Cosmic Microwave Background Anisotropy on Angular Scales of $10'$-5^o". ApJL, 545, L5, December 2000.

[74] F. K. Hansen, P. Cabella, D. Marinucci, and N. Vittorio. "Asymmetries in the Local Curvature of the Wilkinson Microwave Anisotropy Probe Data". ApJ, 607, L67, June 2004.

[75] C. G. T. Haslam, C. J. Salter, H. Stoffel, and W. E. Wilson. "A 408 MHz all-sky continuum survey. II - The atlas of contour maps". A&AS, 47, 1, January 1982.

[76] S. W. Hawking, I. G. Moss, and J. M. Stewart. "Bubble collisions in the very early universe". Phys. Rev. D., 26, 2681, November 1982.

[77] A. F. Heavens. "Estimating non-Gaussianity in the microwave background". MNRAS, 299, 805, September 1998.

[78] G. Hinshaw, M. R. Nolta, C. L. Bennett, R. Bean, O. Doré, M. R. Greason, M. Halpern, R. S. Hill, N. Jarosik, A. Kogut, E. Komatsu, M. Limon, N. Odegard, S. S. Meyer, L. Page, H. V. Peiris, D. N. Spergel, G. S. Tucker, L. Verde, J. L. Weiland, E. Wollack, and E. L. Wright. "Three-Year Wilkinson Microwave Anisotropy Probe (WMAP) Observations: Temperature Analysis". ApJS, 170, 288, June 2007.

[79] G. Hinshaw, J. L. Weiland, R. S. Hill, N. Odegard, D. Larson, C. L. Bennett, J. Dunkley, B. Gold, M. R. Greason, N. Jarosik, E. Komatsu, M. R. Nolta, L. Page, D. N. Spergel, E. Wollack, M. Halpern, A. Kogut, M. Limon, S. S. Meyer, G. S. Tucker, and E. L. Wright. "Five-Year Wilkinson Microwave Anisotropy Probe Observations: Data Processing, Sky Maps, and Basic Results". ApJS, 180, 225, February 2009.

[80] M. P. Hobson, A. W. Jones, A. N. Lasenby, and F. R. Bouchet. "Foreground separation methods for satellite observations of the cosmic microwave background". MNRAS, 300, 1, October 1998.

[81] M. P. Hobson, R. B. Barreiro, L. Toffolatti, A. N. Lasenby, J. Sanz, A. W. Jones, and F. R. Bouchet. "The effect of point sources on satellite obser-

vations of the cosmic microwave background". MNRAS, 306, 232, June 1999.

[82] F. Hoyle. "A New Model for the Expanding Universe". MNRAS, 108, 372, 1948.

[83] E. Hubble. "A Relation between Distance and Radial Velocity among Extra-Galactic Nebulae". Proceedings of the National Academy of Science, 15, 168, March 1929.

[84] K. T. Inoue and J. Silk. "Local Voids as the Origin of Large-Angle Cosmic Microwave Background Anomalies. I." ApJ, 648, 23, September 2006.

[85] K. T. Inoue and J. Silk. "Local Voids as the Origin of Large-Angle Cosmic Microwave Background Anomalies: The Effect of a Cosmological Constant". ApJ, 664, 650, August 2007.

[86] T. R. Jaffe, A. J. Banday, H. K. Eriksen, K. M. Górski, and F. K. Hansen. "Evidence of Vorticity and Shear at Large Angular Scales in the WMAP Data: A Violation of Cosmological Isotropy?" ApJ, 629, L1, August 2005.

[87] T. R. Jaffe, S. Hervik, A. J. Banday, and K. M. Górski. "On the Viability of Bianchi Type VII_h Models with Dark Energy". ApJ, 644, 701, June 2006.

[88] N. Jarosik, C. Barnes, C. L. Bennett, M. Halpern, G. Hinshaw, A. Kogut, M. Limon, S. S. Meyer, L. Page, D. N. Spergel, G. S. Tucker, J. L. Weiland, E. Wollack, and E. L. Wright. "First-Year Wilkinson Microwave Anisotropy Probe (WMAP) Observations: On-Orbit Radiometer Characterization". ApJS, 148, 29, September 2003.

[89] N. Jarosik, C. Barnes, M. R. Greason, R. S. Hill, M. R. Nolta, N. Odegard, J. L. Weiland, R. Bean, and et al. "Three-Year Wilkinson Microwave Anisotropy Probe (WMAP) Observations: Beam Profiles, Data Processing, Radiometer Characterization, and Systematic Error Limits". ApJS, 170, 263, June 2007.

[90] E. Jeong and G. F. Smoot. "Probing Non-Gaussianity In The Cosmic Microwave Background Anisotropies: One Point Distribution Function". arXiv:0710.2371, October 2007.

[91] D. Jeong and E. Komatsu. "Primordial non-Gaussianity, scale-dependent bias, and the bispectrum of galaxies". arXiv:0904.0497, April 2009.

[92] A. Kogut, A. J. Banday, C. L. Bennett, K. M. Gorski, G. Hinshaw, G. F. Smoot, and E. L. Wright. "Tests for Non-Gaussian Statistics in the DMR Four-Year Sky Maps". ApJ, 464, L29, June 1996.

[93] E. Komatsu and D. N. Spergel. "Acoustic signatures in the primary microwave background bispectrum". Phys. Rev. D., 63, 063002, March 2001.

[94] E. Komatsu, B. D. Wandelt, D. N. Spergel, A. J. Banday, and K. M. Górski. "Measurement of the Cosmic Microwave Background Bispectrum on the COBE DMR Sky Maps". ApJ, 566, 19, February 2002.

[95] E. Komatsu, A. Kogut, M. R. Nolta, C. L. Bennett, M. Halpern, G. Hinshaw, N. Jarosik, M. Limon, S. S. Meyer, L. Page, D. N. Spergel, G. S. Tucker, L. Verde, E. Wollack, and E. L. Wright. "First-Year Wilkinson Microwave Anisotropy Probe (WMAP) Observations: Tests of Gaussianity". ApJS, 148, 119, September 2003.

[96] E. Komatsu, D. N. Spergel, and B. D. Wandelt. "Measuring Primordial Non-Gaussianity in the Cosmic Microwave Background". ApJ, 634, 14, November 2005.

[97] E. Komatsu, J. Dunkley, M. R. Nolta, C. L. Bennett, B. Gold, G. Hinshaw, N. Jarosik, D. Larson, M. Limon, L. Page, D. N. Spergel, M. Halpern, R. S. Hill, A. Kogut, S. S. Meyer, G. S. Tucker, J. L. Weiland, E. Wollack, and E. L. Wright. "Five-Year Wilkinson Microwave Anisotropy Probe Observations: Cosmological Interpretation". ApJS, 180, 330, February 2009.

[98] C.-L. Kuo, P. Ade, J. J. Bock, M. D. Daub, J. Goldstein, W. L. Holzapfel, A. E. Lange, M. Newcomb, J. B. Peterson, J. Ruhl, M. C. Runyan, and E. Torbet. "ACBAR CMB Power Spectrum". Bulletin of the American Astronomical Society, 34, 1324, December 2002.

[99] M. Lachieze-Rey and J. Luminet. "Cosmic topology". Phys. Rep., 254, 135, March 1995.

[100] J. M. Lamarre, J. L. Puget, F. Bouchet, P. A. R. Ade, A. Benoit, J. P. Bernard, J. Bock, P. de Bernardis, J. Charra, F. Couchot, J. Delabrouille, G. Efstathiou, M. Giard, G. Guyot, A. Lange, B. Maffei, A. Murphy, F. Pajot, M. Piat, I. Ristorcelli, D. Santos, R. Sudiwala, J. F. Sygnet, J. P. Torre, V. Yurchenko, and D. Yvon. "The Planck High Frequency Instrument, a

third generation CMB experiment, and a full sky submillimeter survey". New Astronomy Review, 47, 1017, December 2003.

[101] K. Land and J. Magueijo. "The Axis of Evil revisited". MNRAS, 378, 153, June 2007.

[102] D. Langlois, S. Renaux-Petel, D. A. Steer, and T. Tanaka. "Primordial perturbations and non-Gaussianities in DBI and general multifield inflation". Phys. Rev. D., 78, 063523, September 2008.

[103] D. L. Larson and B. D. Wandelt. "The Hot and Cold Spots in the Wilkinson Microwave Anisotropy Probe Data Are Not Hot and Cold Enough". ApJ, 613, L85, October 2004.

[104] A. Lewis, A. Challinor, and A. Lasenby. "Efficient Computation of Cosmic Microwave Background Anisotropies in Closed Friedmann-Robertson-Walker Models". ApJ, 538, 473, August 2000.

[105] A. D. Linde. "A new inflationary Universe scenario: a possible solution of the horizon, flatness, homogeneity, isotropy and primordial monopole problems." Physics Letters B, 108, 389, 1982.

[106] A. D. Linde. "Chaotic inflation." Physics Letters B, 129, 177, 1983.

[107] A. D. Linde. "Generation of isothermal density perturbations in an inflationary universe." Soviet Journal of Experimental and Theoretical Physics Letters, 40, 1333, December 1984.

[108] A. R. Liddle and D. H. Lyth. *Cosmological Inflation and Large-Scale Structure*. Cambridge University Press, April 2000.

[109] M. Liguori, S. Matarrese, and L. Moscardini. "High-Resolution Simulations of Non-Gaussian Cosmic Microwave Background Maps in Spherical Coordinates". ApJ, 597, 57, November 2003.

[110] M. Liguori, A. Yadav, F. K. Hansen, E. Komatsu, S. Matarrese, and B. Wandelt. "Temperature and polarization CMB maps from primordial non-Gaussianities of the local type". Phys. Rev. D, 76, 105016, November 2007.

[111] M. S. Longair. *The cosmic century: a history of astrophysics and cosmology*. Cambridge University Press, 2006.

[112] M. López-Caniego, J. González-Nuevo, D. Herranz, M. Massardi, J. L. Sanz, G. De Zotti, L. Toffolatti, and F. Argüeso. "Nonblind Catalog of Extragalactic Point Sources from the Wilkinson Microwave Anisotropy Probe (WMAP) First 3 Year Survey Data". ApJS, 170, 108, May 2007.

[113] J.-P. Luminet, J. R. Weeks, A. Riazuelo, R. Lehoucq, and J.-P. Uzan. "Dodecahedral space topology as an explanation for weak wide-angle temperature correlations in the cosmic microwave background". Nature, 425, 593, October 2003.

[114] X. Luo and D. N. Schramm. "Kurtosis, skewness, and non-Gaussian cosmological density perturbations". ApJ, 408, 33, May 1993.

[115] D. H. Lyth and D. Wands. "Generating the curvature perturbation without an inflaton". Physics Letters B, 524, 5, January 2002.

[116] J. F. Macías-Pérez, G. Lagache, B. Maffei, K. Ganga, A. Bourrachot, P. Ade, A. Amblard, R. Ansari, E. Aubourg, J. Aumont, S. Bargot, J. Bartlett, A. Benoît, J.-P. Bernard, R. Bhatia, A. Blanchard, J. J. Bock, A. Boscaleri, F. R. Bouchet, P. Camus, J.-F. Cardoso, F. Couchot, P. de Bernardis, J. Delabrouille, F.-X. Désert, O. Doré, M. Douspis, L. Dumoulin, X. Dupac, P. Filliatre, P. Fosalba, F. Gannaway, B. Gautier, M. Giard, Y. Giraud-Héraud, R. Gispert, L. Guglielmi, J.-C. Hamilton, S. Hanany, S. Henrot-Versillé, V. Hristov, J. Kaplan, J.-M. Lamarre, A. E. Lange, K. Madet, C. Magneville, D. P. Marrone, S. Masi, F. Mayet, J. A. Murphy, F. Naraghi, F. Nati, G. Patanchon, O. Perdereau, G. Perrin, S. Plaszczynski, M. Piat, N. Ponthieu, S. Prunet, J.-L. Puget, C. Renault, C. Rosset, D. Santos, A. Starobinsky, I. Strukov, R. V. Sudiwala, R. Teyssier, M. Tristram, C. Tucker, J.-C. Vanel, D. Vibert, E. Wakui, and D. Yvon. "Archeops inflight performance, data processing, and map making". A&A, 467, 1313, June 2007.

[117] D. Maino, A. Farusi, C. Baccigalupi, F. Perrotta, A. J. Banday, L. Bedini, C. Burigana, G. De Zotti, K. M. Górski, and E. Salerno. "All-sky astrophysical component separation with Fast Independent Component Analysis (FASTICA)". MNRAS, 334, 53, July 2002.

[118] D. Maino, S. Donzelli, A. J. Banday, F. Stivoli, and C. Baccigalupi. "Cosmic microwave background signal in Wilkinson Microwave Anisotropy Probe three-year data with FASTICA". MNRAS, 374, 1207, February 2007.

[119] D. Marinucci, D. Pietrobon, A. Balbi, P. Baldi, P. Cabella, G. Kerkyacharian, P. Natoli, D. Picard, and N. Vittorio. "Spherical needlets for cosmic microwave background data analysis". MNRAS, 383, 539, January 2008.

[120] E. Martínez-González, J. E. Gallegos, F. Argüeso, L. Cayón, and J. L. Sanz. "The performance of spherical wavelets to detect non-Gaussianity in the cosmic microwave background sky". MNRAS, 336, 22, October 2002.

[121] E. Martínez-González, J. M. Diego, P. Vielva, and J. Silk. "Cosmic microwave background power spectrum estimation and map reconstruction with the expectation-maximization algorithm". MNRAS, 345, 1101, November 2003.

[122] E. Martinez-Gonzalez. "Cosmic Microwave Background anisotropies: the power spectrum and beyond". arXiv:astro-ph/0610162, October 2006.

[123] E. Martínez-González. "Gaussianity". arXiv:0805.4157, 805, May 2008.

[124] J. C. Mather, E. S. Cheng, D. A. Cottingham, R. E. Eplee, Jr., D. J. Fixsen, T. Hewagama, R. B. Isaacman, K. A. Jensen, S. S. Meyer, P. D. Noerdlinger, S. M. Read, L. P. Rosen, R. A. Shafer, E. L. Wright, C. L. Bennett, N. W. Boggess, M. G. Hauser, T. Kelsall, S. H. Moseley, Jr., R. F. Silverberg, G. F. Smoot, R. Weiss, and D. T. Wilkinson. "Measurement of the cosmic microwave background spectrum by the cobe firas instrument". ApJ, 420, 439, January 1994.

[125] J. D. McEwen, M. P. Hobson, A. N. Lasenby, and D. J. Mortlock. "A high-significance detection of non-Gaussianity in the Wilkinson Microwave Anisotropy Probe 1-yr data using directional spherical wavelets". MNRAS, 359, 1583, June 2005.

[126] A. D. Miller, R. Caldwell, M. J. Devlin, W. B. Dorwart, T. Herbig, M. R. Nolta, L. A. Page, J. Puchalla, E. Torbet, and H. T. Tran. "A Measurement of the Angular Power Spectrum of the Cosmic Microwave Background from $\ell = 100$ to 400". ApJL, 524, L1, October 1999.

[127] H. Minkoski. "Volumen und Oberflähe". Mathematische Ann., 57, 447, October 1903.

[128] C. Monteserín, R. B. Barreiro, J. L. Sanz, and E. Martínez-González. "Scalar statistics on the sphere: application to the cosmic microwave background". MNRAS, 360, 9, June 2005.

[129] C. Monteserín, R. B. Barreiro, E. Martínez-González, and J. L. Sanz. "Scalar quantities as detectors of non-Gaussianity in cosmic microwave background maps". MNRAS, 371, 312, September 2006.

[130] C. Monteserín, R. B. Barreiro, P. Vielva, E. Martínez-González, M. P. Hobson, and A. N. Lasenby. "A low cosmic microwave background variance in the Wilkinson Microwave Anisotropy Probe data". MNRAS, 387, 209, June 2008.

[131] P. Mukherjee, M. P. Hobson, and A. N. Lasenby. "Do wavelets really detect non-Gaussianity in the 4-year COBE data?" MNRAS, 318, 1157, November 2000.

[132] P. Mukherjee and Y. Wang. "Wavelets and Wilkinson Microwave Anisotropy Probe Non-Gaussianity". ApJ, 613, 51, September 2004.

[133] P. D. Naselsky, L.-Y. Chiang, P. Olesen, and O. V. Verkhodanov. "Primordial Magnetic Field and Non-Gaussianity of the One-Year Wilkinson Microwave Anisotropy Probe Data". ApJ, 615, 45, November 2004.

[134] M. R. Nolta, J. Dunkley, R. S. Hill, G. Hinshaw, E. Komatsu, D. Larson, L. Page, D. N. Spergel, C. L. Bennett, B. Gold, N. Jarosik, N. Odegard, J. L. Weiland, E. Wollack, M. Halpern, A. Kogut, M. Limon, S. S. Meyer, G. S. Tucker, and E. L. Wright. "Five-Year Wilkinson Microwave Anisotropy Probe Observations: Angular Power Spectra". ApJS, 180, 296, February 2009.

[135] A. de Oliveira-Costa, M. Tegmark, M. Zaldarriaga, and A. Hamilton. "Significance of the largest scale CMB fluctuations in WMAP". Phys. Rev. D., 69, 063516, March 2004.

[136] J. Pando, D. Valls-Gabaud, and L. Z. Fang. "Evidence for scale-scale correlations in the cosmic microwave background radiation". Physical Review Letters, 81, 4568, November 1998.

[137] G. Patanchon, J.-F. Cardoso, J. Delabrouille, and P. Vielva. "Cosmic microwave background and foregrounds in Wilkinson Microwave Anisotropy Probe first-year data". MNRAS, 364, 1185, December 2005.

[138] A. A. Penzias and R. W. Wilson. "A Measurement of Excess Antenna Temperature at 4080 Mc/s." ApJ, 142, 419, July 1965.

[139] D. Pietrobon, P. Cabella, A. Balbi, G. de Gasperis, and N. Vittorio. "Constraints on primordial non-Gaussianity from a needlet analysis of the WMAP-5 data". MNRAS, 396, 1682, July 2009.

[140] N. Ponthieu, J. F. Macías-Pérez, M. Tristram, P. Ade, A. Amblard, R. Ansari, J. Aumont, É. Aubourg, A. Benoît, J.-P. Bernard, A. Blanchard, J. J. Bock, F. R. Bouchet, A. Bourrachot, P. Camus, J.-F. Cardoso, F. Couchot, P. de Bernardis, J. Delabrouille, F.-X. Désert, M. Douspis, L. Dumoulin, P. Filliatre, P. Fosalba, M. Giard, Y. Giraud-Héraud, R. Gispert, J. Grain, L. Guglielmi, J.-C. Hamilton, S. Hanany, S. Henrot-Versillé, J. Kaplan, G. Lagache, A. E. Lange, K. Madet, B. Maffei, S. Masi, F. Mayet, F. Nati, G. Patanchon, O. Perdereau, S. Plaszczynski, M. Piat, S. Prunet, J.-L. Puget, C. Renault, C. Rosset, D. Santos, D. Vibert, and D. Yvon. "Temperature and polarization angular power spectra of Galactic dust radiation at 353 GHz as measured by Archeops". A&A, 444, 327, December 2005.

[141] J. C. W. Rayner and D. J. Best. *Smooth test of goodness of fit*. Oxford University Press, 1989.

[142] J. C. W. Rayner and D. J. Best. "Smooth tests of goodness of fit: An overview." Int. Stat. Rev., 58, 9, January 1990.

[143] J. A. Rubiño-Martín, A. M. Aliaga, R. B. Barreiro, R. A. Battye, P. Carreira, K. Cleary, R. D. Davies, R. J. Davis, C. Dickinson, R. Génova-Santos, K. Grainge, C. M. Gutiérrez, Y. A. Hafez, M. P. Hobson, M. E. Jones, R. Kneissl, K. Lancaster, A. Lasenby, J. P. Leahy, K. Maisinger, E. Martínez-González, G. G. Pooley, N. Rajguru, R. Rebolo, J. L. Sanz, R. D. E. Saunders, R. S. Savage, A. Scaife, P. Scott, A. Slosar, A. C. Taylor, D. Titterington, E. Waldram, and R. A. Watson. "Non-Gaussianity in the Very Small Array cosmic microwave background maps with smooth goodness-of-fit tests". MNRAS, 369, 909, June 2006.

[144] O. Rudjord, F. K. Hansen, X. Lan, M. Liguori, D. Marinucci, and S. Matarrese. "An Estimate of the Primordial Non-Gaussianity Parameter f_{NL} Using the Needlet Bispectrum from WMAP". arXiv:0901.3154, January 2009.

[145] R. K. Sachs and A. M. Wolfe. "Perturbations of a Cosmological Model and

Angular Variations of the Microwave Background". ApJ, 147, 73, January 1967.

[146] D. S. Salopek and J. R. Bond. "Nonlinear evolution of long-wavelength metric fluctuations in inflationary models". Phys. Rev. D., 42, 3936, December 1990.

[147] J. L. Sanz, D. Herranz, M. Lopez-Caniego, and F. Argueso. "Wavelets on the sphere. Application to the detection problem". arXiv:astro-ph/0609351, September 2006.

[148] D. J. Schlegel, D. P. Finkbeiner, and M. Davis. "Maps of Dust Infrared Emission for Use in Estimation of Reddening and Cosmic Microwave Background Radiation Foregrounds". ApJ, 500, 525, 1998.

[149] J. Schmalzing and K. M. Gorski. "Minkowski functionals used in the morphological analysis of cosmic microwave background anisotropy maps". MNRAS, 297, 355, June 1998.

[150] U. Seljak and M. Zaldarriaga. "A Line-of-Sight Integration Approach to Cosmic Microwave Background Anisotropies". ApJ, 469, 437, October 1996.

[151] J. L. Sievers, T. J. Pearson, A. C. S. Readhead, M. C. Shepherd, P. S. Udomprasert, J. K. Cartwright, B. S. Mason, S. Padin, S. T. Myers, J. R. Bond, C. Contaldi, S. Prunet, and D. Pogosyan. "The CMB Power Spectrum from CBI Mosaics". Bulletin of the American Astronomical Society, 33, 1357, December 2001.

[152] J. Silk. "Cosmic Black-Body Radiation and Galaxy Formation". ApJ, 151, 459, February 1968.

[153] E. Silverstein and D. Tong. "Scalar speed limits and cosmology: Acceleration from D-cceleration". Phys. Rev. D., 70, 103505, November 2004.

[154] G. F. Smoot, C. L. Bennett, A. Kogut, E. L. Wright, J. Aymon, N. W. Boggess, E. S. Cheng, G. de Amici, S. Gulkis, M. G. Hauser, G. Hinshaw, P. D. Jackson, M. Janssen, E. Kaita, T. Kelsall, P. Keegstra, C. Lineweaver, K. Loewenstein, P. Lubin, J. Mather, S. S. Meyer, S. H. Moseley, T. Murdock, L. Rokke, R. F. Silverberg, L. Tenorio, R. Weiss, and D. T. Wilkinson. "Structure in the COBE differential microwave radiometer first-year maps". ApJL, 396, L1, September 1992.

[155] K. M. Smith, L. Senatore, and M. Zaldarriaga. "Optimal limits on f_{nl}^{local} from WMAP 5-year data". arXiv:0901.2572, January 2009.

[156] D. N. Spergel, R. Bean, O. Doré, M. R. Nolta, C. L. Bennett, J. Dunkley, G. Hinshaw, N. Jarosik, E. Komatsu, L. Page, H. V. Peiris, L. Verde, M. Halpern, R. S. Hill, A. Kogut, M. Limon, S. S. Meyer, N. Odegard, G. S. Tucker, J. L. Weiland, E. Wollack, and E. L. Wright. "Three-Year Wilkinson Microwave Anisotropy Probe (WMAP) Observations: Implications for Cosmology". ApJS, 170, 377, June 2007.

[157] J.-L. Starck, Y. Moudden, P. Abrial, and M. Nguyen. "Wavelets, ridgelets and curvelets on the sphere". A&A, 446, 1191, February 2006.

[158] V. Stolyarov, M. P. Hobson, M. A. J. Ashdown, and A. N. Lasenby. "All-sky component separation for the Planck mission". MNRAS, 336, 97, October 2002.

[159] M. Tegmark and G. Efstathiou. "A method for subtracting foregrounds from multifrequency CMB sky maps". MNRAS, 281, 1297, August 1996.

[160] M. Tristram, G. Patanchon, J. F. Macías-Pérez, P. Ade, A. Amblard, R. Ansari, É. Aubourg, A. Benoît, J.-P. Bernard, A. Blanchard, J. J. Bock, F. R. Bouchet, A. Bourrachot, P. Camus, J.-F. Cardoso, F. Couchot, P. de Bernardis, J. Delabrouille, F.-X. Désert, M. Douspis, L. Dumoulin, P. Filliatre, P. Fosalba, M. Giard, Y. Giraud-Héraud, R. Gispert, L. Guglielmi, J.-C. Hamilton, S. Hanany, S. Henrot-Versillé, J. Kaplan, G. Lagache, J.-M. Lamarre, A. E. Lange, K. Madet, B. Maffei, C. Magneville, S. Masi, F. Mayet, F. Nati, O. Perdereau, S. Plaszczynski, M. Piat, N. Ponthieu, S. Prunet, C. Renault, C. Rosset, D. Santos, D. Vibert, and D. Yvon. "The CMB temperature power spectrum from an improved analysis of the Archeops data". A&A, 436, 785, June 2005.

[161] G. De Troia, P. A. R. Ade, J. J. Bock, J. R. Bond, J. Borrill, A. Boscaleri, P. Cabella, C. R. Contaldi, B. P. Crill, P. de Bernardis, G. De Gasperis, A. de Oliveira-Costa, G. Di Stefano, P. G. Ferreira, E. Hivon, A. H. Jaffe, T. S. Kisner, M. Kunz, W. C. Jones, A. E. Lange, M. Liguori, S. Masi, S. Matarrese, P. D. Mauskopf, C. J. MacTavish, A. Melchiorri, T. E. Montroy, P. Natoli, C. B. Netterfield, E. Pascale, F. Piacentini, D. Pogosyan, G. Polenta, S. Prunet, S. Ricciardi, G. Romeo, J. E. Ruhl, P. Santini, M. Tegmark,

M. Veneziani, and N. Vittorio. "Searching for Non-Gaussian Signals in the BOOMERANG 2003 CMB Maps". ApJ, 670, L73, December 2007.

[162] L. Verde, L. Wang, A. F. Heavens, and M. Kamionkowski. "Large-scale structure, the cosmic microwave background and primordial non-Gaussianity". MNRAS, 313, 141, March 2000.

[163] P. Vielva, E. Martínez-González, L. Cayón, J. M. Diego, J. L. Sanz, and L. Toffolatti. "Predicted Planck extragalactic point-source catalogue". MNRAS, 326, 181, September 2001.

[164] P. Vielva, R. B. Barreiro, M. P. Hobson, E. Martínez-González, A. N. Lasenby, J. L. Sanz, and L. Toffolatti. "Combining maximum-entropy and the Mexican hat wavelet to reconstruct the microwave sky". MNRAS, 328, 1, November 2001.

[165] P. Vielva, E. Martínez-González, R. B. Barreiro, J. L. Sanz, and L. Cayón. "Detection of Non-Gaussianity in the Wilkinson Microwave Anisotropy Probe First-Year Data Using Spherical Wavelets". ApJ, 609, 22, July 2004.

[166] P. Vielva, Y. Wiaux, E. Martínez-González, and P. Vandergheynst. "Alignment and signed-intensity anomalies in Wilkinson Microwave Anisotropy Probe data". MNRAS, 381, 932, November 2007.

[167] P. Vielva. "Probing the Gaussianity and the statistical isotropy of the CMB with spherical wavelets". Society of Photo-Optical Instrumentation Engineers (SPIE) Conference Series, 6701, 670119, October 2007.

[168] P. Vielva and J. L. Sanz. "Analysis of non-Gaussian CMB maps based on the N-pdf. Application to WMAP data". arXiv:0812.1756, December 2008.

[169] A. Vilenkin and E. P. S. Shellard. *Cosmic strings and other topological defects*. Cambridge University Press, 1994.

[170] R. A. Watson, C. M. Gutierrez de La Cruz, R. D. Davies, A. N. Lasenby, R. Rebolo, J. E. Beckman, and S. Hancock. "Anisotropy measurements of the cosmic microwave background radiation at intermediate angular scales". Nature, 357, 660, June 1992.

[171] Y. Wiaux, P. Vielva, E. Martínez-González, and P. Vandergheynst. "Global Universe Anisotropy Probed by the Alignment of Structures in the Cos-

mic Microwave Background". Physical Review Letters, 96, 151303, April 2006.

[172] Y. Wiaux, P. Vielva, R. B. Barreiro, E. Martínez-González, and P. Vandergheynst. "Non-Gaussianity analysis on local morphological measures of WMAP data". MNRAS, 385, 939, April 2008.

[173] A. P. S. Yadav and B. D. Wandelt. "Evidence of Primordial Non-Gaussianity (f_{NL}) in the Wilkinson Microwave Anisotropy Probe 3-Year Data at 2.8σ". Physical Review Letters, 100, 181301, May 2008.

[174] D. Yvon and F. Mayet. "Mirage: A new iterative map-making code for CMB experiments". A&A, 436, 729, June 2005.

[175] M. Zaldarriaga and U. Seljak. "CMBFAST for Spatially Closed Universes". ApJS, 129, 431, August 2000.

[176] G. de Zotti, R. Ricci, D. Mesa, L. Silva, P. Mazzotta, L. Toffolatti, and J. González-Nuevo. "Predictions for high-frequency radio surveys of extragalactic sources". A&A, 431, 893, March 2005.